2014

An Efficient Approach to EPID Transit Dosimetry

Bart Alan Morris
Louisiana State University and Agricultural and Mechanical College, bmorr25@lsu.edu

AN EFFICIENT APPROACH TO EPID TRANSIT DOSIMETRY

A Thesis

Submitted to the Graduate Faculty of the
Louisiana State University and
Agricultural and Mechanical College
in partial fulfillment of the
requirements for the degree of
Master of Science

in

The Department of Physics and Astronomy

by
Bart Alan Morris
B.S., Middle Tennessee State University, 2011
August 2014

ACKNOWLEDGMENTS

I would like to thank the LSU and Mary Bird Perkins Cancer Center faculty, staff, and students for what has been a rigorous, but rewarding graduate school experience. The LSU medical physics program has prepared me in many ways for a future as a medical physicist. Thank you to Oncology Data Systems for their funding contributions to this research.

I owe a tremendous debt of gratitude to Dr. Jonas Fontenot for giving me the opportunity to work with him on this research endeavor and for the guidance he provided throughout the project. I appreciate his ability to lead by example and his unending belief in the progress of this work. He taught me a tremendous amount about research, medical physics, and professionalism.

I am grateful to committee members Connell Chu, Dr. Peter Diener, Dr. John Gibbons, Dr. Kenneth Matthews, and Dr. Guang Jia for sacrificing their time and for supplying their knowledge and talents.

Thank you to Susan Hammond, Paige Barcia, and Katie Bailey for their many logistical contributions.

Finally, I want to thank Shelley and Jack Morris, and the rest of our family. I cannot imagine having faced the last three years without their support and inspiration. I will be forever grateful to Shelley for her patience and belief over the last several years.

TABLE OF CONTENTS

LIST OF TABLES

LIST OF FIGURES

ABSTRACT

Introduction: In order to maintain uniform standards in the accuracy of fractionated radiation therapy, quantification of the delivered dose per fraction accuracy is required. The pupose of this study was to investigate the feasibility of a transit dosimetry method using the electronic portal imaging device (EPID) for dose delivery error detection and prevention.

Methods and Materials: In the proposed method, 2D predicted transit images were generated for comparison with online images acquired during treatment. Predicted transit images were generated by convolving through-air EPID measurements of each field with pixel-specific kernels selected from a library of pre-calculated Monte Carlo pencil kernels of various radiological thicknesses. The kernel used for each pixel was selected based on the calculated radiological thickness of the patient along the line joining the pixel to the virtual source. The accuracy of the technique was evaluated in homogeneous plastic water phantoms, a heterogeneous cylindrical phantom, and an anthropomorphic head phantom. Gamma analysis was used to quantify the accuracy of the technique for the various cases.

Results: In the comparison between the measured and predicted images, an average of 99.4% of the points in passed a 3%/ 3 mm gamma for the homogeneous plastic water phantoms. Points for the heterogeneous cylindrical phantom analysis had a 94.6% passing rate. For the anthropomorphic head phantom, an average of 98.3% and 96.6% of points passed the 5%/3mm and 3%/3mm gamma criteria, respectively for all field

sizes. Failures occurred typically at points when object thickness was changing rapidly or at boundaries between materials, and at the edges of large fields.

Discussion: The results suggested that the proposed transit dosimetry method is a feasible approach to *in vivo* dose monitoring. The gamma analysis passing rates are within the accuracy needed for transit dosimetry. Future research efforts should include evaluation of the method for more complex treatment techniques and assessment of the sensitivity to changes in EPID or linac hardware, as well as characterization of any dependency the method may have on image ghosting or lag, gantry angle, or long-term stability.

CHAPTER 1: INTRODUCTION

1.1 DOSIMETRY FOR TREATMENT VERIFICATION IN RADIATION THERAPY

The proliferation of the use and effectiveness of external beam radiation therapy for the treatment of cancer has been well documented (Wagener 2009; Halperin 2013). Early work in the field of radiotherapy by Roentgen and Grubbe (Grubbe 1902), has been followed by over a century of advancements in treatment techniques and a better understanding of the pertinent physical and biological processes. Although it is estimated that there will be more than 500,000 cancer deaths in the United States in 2014, mortality rates are declining due to the advancements in detection and treatment of the disease (Siegel 2014). Nearly two-thirds of all cancer patients in the U.S. receive radiation treatment for their disease (SROA 2010), Nevertheless, existing rates of mortality provide continued motivation to look for new and better methods (Jemal 2010).

Current external beam radiation treatment methods generally include a series of treatment sessions known as fractions, which take place over the course of days or weeks. The primary purpose for distributing the therapeutic dose over time is to take advantage of naturally occurring radiobiology processes (Hall 2006). Recent advances in radiotherapy have allowed physicians to prescribe higher total dose and dose per fraction to the tumor with acceptable morbidity (Zietman 2005). The increase in total dose over the course of treatment places increased importance on the accuracy of the dose delivery.

To maintain uniform standards in the accuracy of fractionated radiation therapy, quantification of the accuracy of delivered dose per fraction is required. This topic has been addressed by the International Commision on Radiation Units and Measurements (ICRU) and

the American Association of Physicists in Medicine (AAPM) (Kutcher 1994). The ICRU recommends an overall accuracy of within 5% for each treatment fraction. The AAPM Task Group Report 40 points out that, due to the many steps involved in treatment planning and delivery, the accuracy of each step must be better than 5% in order to maintain the ICRU recommendation for the overall treatment fraction accuracy.

1.2 MODERN TREATMENT PLANNING AND DELIVERY

Modern treatment planning is tailored to the specific anatomy and disease of the patient, most commonly with the use of computed tomography (CT). Three dimensional patient density and geometry information is generated by a CT scan prior to the start of treatment. The information is then input into the treatment planning system and is used to calculate the planned dose distribution delivered to the patient. The treatment planning and approval process can be laborious and time consuming, so a single treatment plan (generated from the pretreatment CT scan) is used for every fraction throughout the course of treatent. Matching the actual dose distribution delivered to the patient to the treatment plan is, therefore, dependent on patient positioning accuracy and any changes in patient anatomy. While advances in image guidance have improved targeting accuracy, errors in the setup positioning of the patient or changes in the patient's anatomy during treatment can cause the delivered dose distribution to be distorted from what was originally planned.

The incentive to accurately deliver radiation dose has increased with the use of intensity-modulated radiation therapy (IMRT) and inverse planning. Initially, radiation therapy was delivered with rectangular fields modulated only by wedges and blocks in an attempt to shape the dose distribution (Webb 2003). Currently, multileaf collimators allow the beam to be

collimated to more precisely conform to the shape of the tumor. The shape of the beam is optimized for a number of different beam angles. Figure 1.1 shows an example illustration of an IMRT prostate treatment with modulated intensity profiles that provide conformal dose distribution to the target, while limiting the dose to normal tissue to acceptable levels.

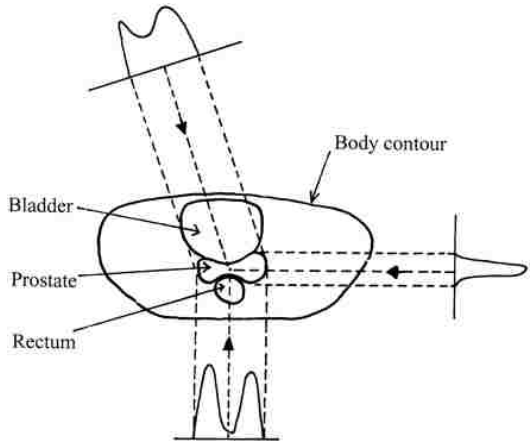

Figure 1.1. Example of IMRT beam angles and intensity profiles. Figure adapted from Webb (2003).

These technological advances have allowed clinicians to exercise a higher level of control with respect to dose distributions. Higher conformity of dose distribution has led to increased normal tissue sparing, which has subsequently allowed the delivery of higher doses to tumors that were previously not possible without severe side effects. Physicians have been treating prostate cases, for example, with escalated doses. Clinical trial results have illustrated that IMRT plans are capable of delivering a higher level of conformity with reduced toxicity (Zelefsky 2006).

Along with the benefits of greater control over dose distributions, however, come challenges. Due to higher dose distribution gradients, there is an associated increased importance on the accuracy and precision of the planned dose delivery (Warkentin 2003). The accuracy of IMRT treatments relies on the proper use and function of planning and delivery

systems, which are built upon complex software and hardware systems. These systems must be rigorously commissioned and checked to ensure that they are performing properly. The treatment planning system calculations and linear accelerator operating parameters must be correct in order to ensure the planned dose is delivered.

1.3 CURRENT QUALITY CONTROL PRACTICES AND THEIR SHORTCOMINGS

Quality assurance (QA) procedures are used to ensure proper delivery of the complex radiation treatments associated with IMRT. The AAPM recommends quality assurance protocols through its Task Group reports. For example, the report from Task Group 53 provides guidelines for treatment planning system QA, while the Task Group 40 and Task Group 142 reports provide QA information for the linear accelerator (Kutcher 1994; Fraass 1998; Klein 2009). The implementation of QA procedures is critically important to ensure the proper delivery of the treatment plan.

In addition to QA for the treatment planning system and the treatment delivery machine, a third category of IMRT QA is patient-specific QA. Patient-specific QA is a necessary part of the overall QA process, and should be addressed prior to the delivery of the first fraction (Ramsey 2003). Patient-specific QA involves verification of the individualized, intensity modulated fields (IMFs) involved in the specific treatment of a patient (LoSasso 2001). The verification of IMFs is a check to make sure the delivery beams designed in the treatment plan are being delivered by the linear accelerator as expected. Verification of IMFs is accomplished by measurements of delivered dose from the planned fields of an IMRT treatment. The fields are measured without the patient in the beam path, and measurements are made to ensure the delivered fields match the planned fields in terms of dose delivered. The dose that will

ultimately be delivered to the patient, however, is assumed to be correct from the pretreatment verification of the IMF's. Commonly, the individual fields are delivered, and planar dose maps are taken with ion chamber or diode arrays, film, or an electronic portal imaging device (EPID) (Dong 2003; Both 2007; van Elmpt 2008).

Patient-specific QA dosimetry is verified by analysis of individual or composite IMFs. The comparison of planned and measured doses from the IMFs is quantified by gamma analysis (Low 1998). Gamma analysis quantifies the difference between the planned and measured doses by examining both the dose differences between points and the distance-to-agreement (DTA), which is the distance to the nearest measured point that matches the planned dose. The gamma index incorporates both of these metrics into a single value:

$$\Gamma = \sqrt{\left(\frac{r}{\Delta d}\right)^2 + \left(\frac{\delta}{\Delta D}\right)^2} \qquad [1]$$

where r represents the DTA, and δ represents the magnitude of the difference between the measured dose value and the planned dose value. The point is considered to "pass" if the Γ value is less than 1. Δd and ΔD are the required agreement between the measured and planned dose distribution. For example, the dose difference criterion (ΔD) might be assigned to 3%, and the DTA criterion (Δd) could be set to 3 mm.

In addition to IMRT QA, patient positioning also impacts the accuracy of treatment plan delivery. Achieving the planned dose distribution requires the patient to be in the expected orientation with respect to the beam for each treatment field. Image guidance is commonly employed to ensure proper patient position prior to each fraction (van Herk 2004). With image guidance, images from the planning CT are compared with real-time images of the patient on the treatment couch to verify that the patient is positioned as expected by the treatment plan.

Current methods of image guidance include portal imaging, cone beam computed tomography (CBCT), megavoltage computed tomography, and stereoscopic x-ray imaging (Verellen 2007).

Image guidance is performed by aligning the images of the patient taken just prior to treatment with images used in the planning process. For example, for CBCT guided patient alignment, it is common to use bony anatomy as a reference point (Figure 1.2). However, in a number of situations, this form of positioning verification may be inadequate. For example, the alignment of bony anatomy may not ensure that soft tissues have not shifted relative to their position at the time of the treatment planning imaging.

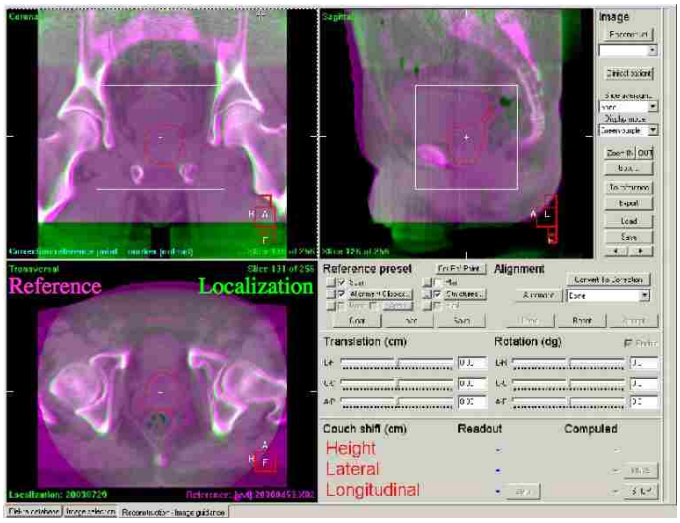

Figure 1.2. Image guidance using CBCT. The purple and green images are from the planning CT and CBCT, respectively. Adjustments are made to the patient position until agreement between the two image sets is achieved (van Herk 2004).

Historically, portal images were acquired on film. Film was the standard imaging medium for decades and provides extremely high spatial resolution. Flat panel digital technology can provide certain advantages over film including higher detection efficiency, higher dynamic range, and post processing capabilities (Vedantham 2000). A current

technology that implements the advantages of digital imaging and is commonly available on linear accelerators is the EPID, shown in Figure 1.3.

Figure 1.3. EPID on an Elekta Linac. Adapted from www.elekta.com

Patient-specific QA and image guidance miss errors that occur during the delivery of radiation to the patient (van Elmpt 2008). These techniques do not account for intrafraction movement of the patient or for changes in patient anatomy. Changes in anatomy during the course of radiotherapy are not uncommon. The size of the tumor, for example may shrink as a result of the radiation treatments, or the patient may lose significant weight. These changes in anatomy can introduce changes in the dose distribution in the patient compared to the distributions in the treatment plan. There is also no guarantee that the patient will not shift position during treatment relative to the positioning verification procedure. Conducting these procedures immediately prior to treatment delivery can help to reduce the chances of patient misalignment, but intrafractional patient movement can nevertheless occur (Litzenberg 2006).

Few methods are available to supplement the short comings of patient-specific QA and patient position verification. *In vivo* dosimetry, or dose measurements carried out during the time of treatment, is one way to give the radiotherapy team further information about delivered dose. With *in vivo* dosimetry, dosimeters are generally placed on the surface of the patient to record dose information during treatment; The information is processed and evaluated after the fraction is delivered (Hansen 1996). Thermoluminescent detectors (TLDs), metal–oxide–semiconductor field-effect transistors, and silicon diodes are three varieties of dosimeters frequently used for *in vivo* dosimetry. Each of these dosimeters has advantages and disadvantages, but all are laborious and time consuming to set up and process (Essers Mijnheer 1999; Jornet 2004). Performing *in vivo* measurements is intrusive for the patient and affects workflow due to the time and manpower associated with setup and subsequent readout of the dosimeters. More importantly, these methods generally provide dose information for only a small number of points; an overall picture of the dose distribution delivered to the patient is unobtainable.

1.4 PRE-TREATMENT DELIVERY VERFICATION USING THE α Si ELECTRONIC PORTAL IMAGING DEVICE

Contemporary electronic portal imaging devices commonly utilize amorphous silicon (a-Si) thin-film transistors (Herman 2001; Antonuk 2002). These are indirect conversion detectors, meaning they incorporate a scintillator layer that converts incident radiation into light prior to detection by a photodiode (Figure 1.4). A metal layer converts x-rays to Compton electrons and absorbs scattered radiation to enhance image quality. Electrons generated in the copper layer, along with some incident photons interact with the phosphor where they produce light. The

light photons then induce charge in the photodiode, which is coupled to a storage capacitor and readout circuit.

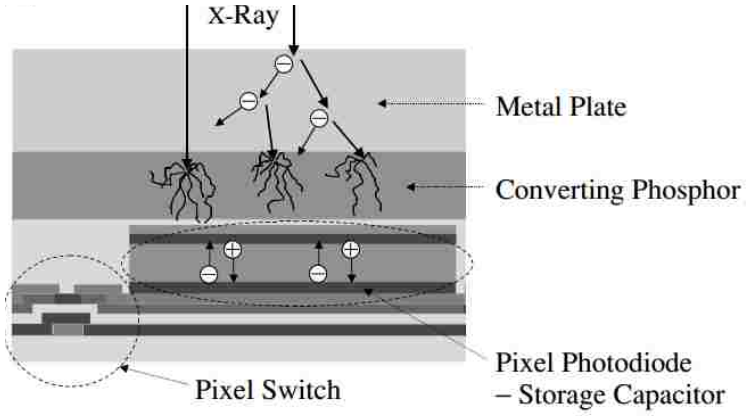

Figure 1.4. Illustration of an indirect scintillating detector. Figure adapted from Antonuk, 2002.

In addition to its function in patient position verification, the EPID as a dosimetric tool for patient-specific QA recently was described (Warkentin 2003; Van Esch 2004). Much of the literature devoted to EPID dosimetry involves the use of the device in a pretreatment setting. In this role, the EPID essentially replaces other two-dimensional planar dose measurement tools, such as diode arrays or film. The EPID is more convenient than a diode array or film measurement, because it is permanently mounted on the linac and no setup of hardware is involved in the QA procedure (Figure 1.3).

1.5 USE OF THE EPID IN TRANSIT DOSIMETRY

An alternative to direct *in vivo* dose measurements is transit dosimetry. Transit dosimetry uses the measured fluence exiting the patient for estimating the dose deposited in the patient. A number of authors have described the process of obtaining transit dose information from measurement of the exit fluence (McNutt 1996; Bogaerts 2000; Louwe 2003). Exit fluence information can be obtained with film, but problems associated with the technique

include variations in the film and film processing (Renner 2003). Many of the same advantages that the EPID displays over film in regard to patient positioning verification carry over to the process of transit dosimetry. In addition, the EPID displays a linear response to dose and eliminates some of the inconsistencies associated with film and film processing (Renner 2005). As a result, numerous studies have been conducted to gauge the feasibility and practicality of using an EPID in transit dosimetry (Pasma 1999; McDermott 2006; Nijsten 2007).

Diverse approaches to EPID transit dosimetry have been proposed in literature (Wendling M BJ. 2006; Renner 2007; van Elmpt 2008). There are four categories of methods with some variations in the implementation details. The four categories include point dose verification, two-dimensional transit dose verification at the plane of the EPID, two-dimensional verification at a plane in the patient, and more complex three-dimensional verification schemes. Some two-dimensional and three-dimensional transit dosimetry methods provide *in vivo* dosimetry; EPID portal dose images are back projected with the use of pretreatment CT information to estimate full dose distributions within the patient.

Use of the EPID as a transit dosimeter has yielded varied results, due to the assorted approaches. Strengths and weaknesses are inherent in the information derived from each method. Each of the methods has proven capable of obtaining acceptable accuracy; each approach provides a mix of information, but varies in the effort needed to implement and process the dosimetry data. The point verification methods were extremely accurate (0.0 ± 1.7%), but they are analogous to current *in vivo* measurements and are similarly limited in value (Nijsten 2007).

The two-dimensional verification methods predict portal dose at either the level of the patient or the level of the imager. In the case of the imager level prediction, the raw EPID

measurements are converted to dose in order to be compared to ionization chamber measurements. These methods used a characterization the response of the EPID to find the dose from the raw measurements (Pasma 1998). Agreement to within 1% between the chamber and EPID measurements has been found using this type of approach. Gamma analysis for measurements of transmitted dose in phantoms has shown 90% point agreement for 3%/3 mm criteria (Mohammadi 2006).

The alternative two-dimensional method is to use transmission EPID images to back-project *in vivo* dose at the level of the patient. Phantom studies showed good agreement of back-projection EPID calculations to *in vivo* film measurements using 2%/2 mm gamma index criteria (Wendling 2006). The back-projection approach was expanded into a three-dimensional approach by other authors (Hansen 1996; Jarry Verhaegen 2007). The two-dimensional EPID measurements are converted to three-dimensional dose information with a dose calculation algorithm and a three-dimensional density representation of the patient. Three-dimensional methods showed acceptable results for 3%/3 mm criteria (van Elmpt 2010).

The two-dimensional approaches are appealing due to their combination of providing a broad picture of dose delivered to the patient and a straightforward means for analysis, namely the gamma criteria outlined in section 1.2. They provide a more detailed dose distribution than one-dimensional point verification methods, while eliminating some of the complexity and sources of error associated with the three-dimensional dosimetry methods. Because two-dimensional methods do not calculate a three-dimensional dose distribution within the patient, however, they are inherently less capable of detecting sources of error then their three-dimensional counterpart (van Elmpt 2008).

Regardless of whether the EPID is being considered for pretreatment patient-specific quality assurance, or for transit dosimetry, the EPID displays a number of unique response characteristics that need to be addressed (van Elmpt 2008). These include the linearity of the EPID response to machine output, the internal non-uniformity corrections made by the EPID software, reproducibility, image ghosting and lagging, dead-time response, energy-dependent response, effects of the metal layer thickness, field size response, glare from the phosphor layer, gantry angle dependence, and backscatter artifacts (Greer Vial 2011). Many of these characteristics are the result of differences between the dosimetric properties of the EPID construction materials and the dosimetric characteristics of tissue (Berry 2012). Most of the characteristics listed above contribute only minor effects with respect to transit dosimetry. The EPID does show, however, large deviations with respect to energy response and field size dependence when compared to ion chamber measurements (Renner 2005; Liebich 2011). In addition, the internal software corrections implemented by the EPID system in order to improve image quality must be addressed to get accurate dose results (Greer 2005).

There have been limited attempts to generalize or commercialize EPID transit dosimetry. In most cases, the method is implemented in a particular clinic, or even for a particular accelerator and may not be easily transferrable to an alternative situation. Unfortunately, early reports indicated that these methods required substantial time and labor to commission the system, run QA procedures, and analyze their results. For example, one author reported dose verification requiring 2.5 hours per plan, and 10-15 minutes per fraction (van Elmpt 2008). In addition, some researchers applied hardware modifications to the EPID to minimize the energy dependence of the device.

The only widespread implementation of EPID dosimetry is the inclusion of a pretreatment QA system known as "PortalVision" by Varian (Varian Medical Systems, Palo Alto, CA). At least two commercially available transit EPID dosimetry packages currently are available. Both Math Resolutions' Dosimetry Check™ (Math Resolutions, LLC, Columbia, MD) and IBA/DOSISoft's EPIgray® (IBA Dosimetry, Bartlett, TN) offer transit dosimetry solutions for any commercial EPID. These systems are relatively new and there are only a few authors who have reported on their experiences with implementing the packages (Dupuis 2011; Chaumet Bleuse 2013; Fafi 2013).

1.6 MOTIVATION FOR RESEARCH

The motivation for this research was to develop a simple and efficient method of EPID transit dosimetry that requires a minimum of time and effort to commission. Ideally, the method would be generalized and implemented in other clinics with any commercial EPID. Specifically this work investigated the feasibility of an approach for predicting two-dimensional transit EPID images under ideal delivery conditions (*i.e.*, no interfraction or intrafraction uncertainties and no treatment delivery error). For this project, no hardware modifications were made to the EPID in order to preserve its normal functionality and make the process applicable to other linear accelerators and EPIDs.

1.7 HYPOTHESIS AND SPECIFIC AIMS

The hypothesis of this work was that a through-air approach to transit dosimetry using the EPID can be devised that will predict EPID transit images to within specified criteria* compared with measured transit images for phantoms of increasing complexity.

*homogeneous phantom: gamma [3%/ 3 mm; 95% passing rate]

*cylindrical heterogeneous phantom: gamma [3%/ 3 mm; 95% passing rate]

*anthropomorphic phantom: gamma [5%/ 3 mm; 95% passing rate]

To test the hypothesis, four specific aims were completed as follows:

Aim 1: Develop the EPID transit dosimetry method for converting "through-air" EPID images to expected patient-specific transit images. Pretreatment images were acquired for each treatment field with no patient in the beam. Transit images were calculated by convolving each pixel of the "through air" image with a pencil beam kernel that depended on the radiological pathlength along the ray between the radiation source and the center of each EPID detector. A Matlab program was written to calculate the radiological pathlengths from CT data, and these pathlengths were used to select the appropriate pencil beam kernel from a lookup table. The pencil kernels were generated with a Monte Carlo model of radiation transport through slabs of water for a variety of radiological thicknesses.

Aim 2: Apply the EPID transit dosimetry method to simple homogeneous phantoms. The EPID transit dosimetry method was tested using square fields delivered to homogeneous phantoms of known thicknesses and density. The phantoms included simple slabs of plastic water of various thicknesses as well as a phantom of complex geometry that varied in thickness from 150 mm to 220 mm. The phantoms were placed vertically on the CT and treatment couches. The single treatment field was positioned laterally and directed isocentrically. Measured image intensity was then compared with the predicted intensity generated using the EPID transit dosimetry technique. A 3%/ 3 mm gamma index of the predicted and measured transit images was used to gauge the accuracy of the predicted transit images.

Aim 3: Apply the EPID transit dosimetry method to a more complex heterogeneous phantom.

The transit dosimetry method was applied to a phantom with a cylindrical shape and air cavity heterogeneities to verify the method for these complicating factors. The beam geometry remained a simple lateral beam (with various square field sizes) delivered isocentrically. Again, a 3%/ 3 mm gamma index was used to compare the predicted images with those that were measured.

Aim 4: Apply the EPID transit dosimetry method to an anthropomorphic head phantom. The transit dosimetry method was tested with a phantom that had realistic patient dimensions, irregular geometry, and heterogeneities. Again, the treatment was an isocentric delivery, with lateral square fields. A 5%/ 3 mm gamma index was used to compare the predicted images with those that were measured.

1.8 OVERVIEW OF THE THESIS

Following the specific aims presented in the previous section, the feasibility study of the EPID transit dosimetry method was conducted. The remainder of this thesis describes the process of developing and testing the method. Chapter 2 describes the research strategy, including the procedure to calculate the radiological pathlengths for each image detector element and the modeling of the pencil beam scatter kernels used to predict scatter and attenuation from the patient. The process of taking open field measurements with the EPID and convolving them with the appropriate kernels is then described. Chapter 2 also discusses preliminary results that let to correction methods to improve the accuracy of the EPID transit dosimetry method. Chapter 2 ends with a description of the methods applied in addressing each Aim. Chapter 3 reports on the results of the study. Finally, Chapter 4 discusses the results

and their implications with respect to testing of the original hypothesis. Chapter 4 also discusses future talks that may be important to develop the EPID transit dosimetry method into a clinical tool.

CHAPTER 2: METHODS AND MATERIALS

2.1 AN EPID TRANSIT DOSIMETRY METHOD - OVERVIEW

For the EPID transit dosimetry method an initial image was measured by the EPID without a phantom in the beam, which accounted for the open beam response of the EPID including accounting for automatic image quality corrections ("Flood-Field corrections") applied by the EPID software (see section 2.3.5). This "through-air" image was used to predict the EPID's response to the treatment beam delivered with the phantom in the beam for a particular field, with the phantom attenuation and scatter, and the resulting change in EPID response accounted for by pixel-specific convolution of the through-air image with pencil kernels. The contribution of attenuation and scatter in both magnitude and spatial distribution was assumed to depend only on the radiological thickness of the object along the ray connecting the source and detector pixel. The pencil kernels were precalculated with a Monte Carlo model of the radiation transport through water slabs of various thicknesses, with dose tallied in a model of the EPID (see section 2.3.1). From CT treatment planning data, radiological pathlengths through the phantom were calculated for the x-ray beam traveling to each EPID pixel. The radiological pathlengths determined the appropriate pencil kernel to apply. At each pixel in the EPID, the selected pencil kernel was centered at the pixel and scaled by the pixel value from the through-air image; finally, all shifted and scaled kernels were summed together to generate the expected EPID transit image (see section 2.3.4). Figure 2.1 shows the workflow process of the proposed transit dosimetry method.

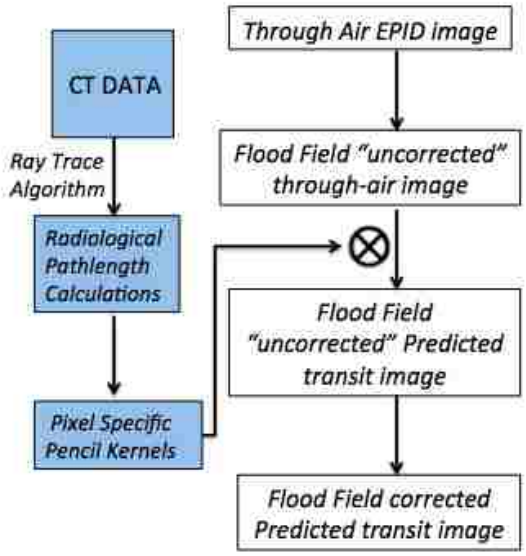

Figure 2.1. Flow chart of transit dosimetry method. Through-air images were first flood field "uncorrected" to remove the internal iView software processing, followed by convolution with pixel specific pencil kernels. Finally, the predicted image has the flood field corrections reapplied for direct comparison to a measured, flood field corrected transit image.

An additional benefit to using the open “through-air” field to calculate predicted EPID treatment images is that the open field images could be used to perform patient-specific QA. The transit dosimetry method could be used in combination with the current patient-specific QA methods such as two-dimensional diode array measurements. Eventually, however, the EPID transit dosimetry method could replace patient-specific QA. Because the patient-specific QA is necessary prior to the first fraction, the process of taking the open field images does not add to the workload, and in fact could reduce the time and effort required to conduct the patient-specific QA, by eliminating the use of separate measurement hardware such as a diode array.

The measured transit images were produced under treatment conditions (matching field size, gantry angle, patient position), and were similar to portal images taken for treatment

positioning verification except for the dose delivered. While typical EPID position verification images are delivered with only a fraction of the treatment dose, the transit images utilized in this dosimetry method required the actual treatment delivered dose.

The through-air images were generated in the same manner as the transit images with the exception that no phantom was in the beam. In this way, the attenuation and scatter from sources other than the phantom, as well as the behavior of the EPID as it responded to the open radiation beam were measured. Essentially, the through-air portal images served as a starting point for predicting the transit images.

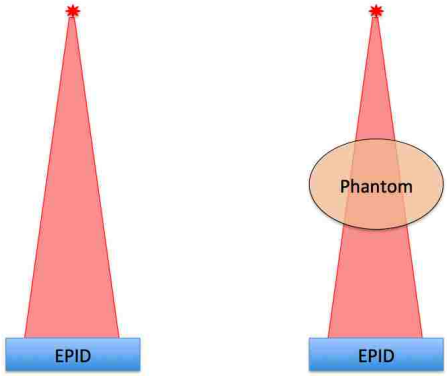

Figure 2.2. Diagram of the experimental setup (Left: Through-air image setup, Right: Transit image setup).

For this thesis, simple square fields were used to test the feasibility of the approach. Each treatment beam was delivered for 3 x 3 cm^2, 5 x 5 cm^2, 10 x 10 cm^2, 15 x 15 cm^2, and 20 x 20 cm^2 field sizes. Open beams of these sizes and shapes were delivered through-air and through the phantom, with images recorded by the EPID. All fields were delivered laterally to minimize the attenuation and scatter inconsistencies resulting from the differences in the CT couch and the treatment machine couch. The x-ray energy was 6 MV and all beams were delivered with 100 monitor units (MU's) at 400 MU/min.

2.2 CHARACTERISTICS OF THE ELEKTA iViewGT™ EPID

The EPID utilized in this study was the Elekta iViewGT™ imaging panel. The EPID contained 1024 x 1024 detector elements with a pixel size of 0.4 x 0.4 mm^2, resulting in a detection area of 40.96 x 40.96 cm^2.

Several authors have reported on EPID response characteristics. Winker measured EPID scatter factors for several iViewGT EPID's at various field sizes and reported reproducibility agreement within ±1% (Winkler Georg 2006). The EPID's response with dose was shown be linear for a range of MU's from 2-200, with an increased response to changes in field size and phantom thickness relative to ion chamber measurements (Renner 2005). Several measurements were performed to confirm that the behavior of the EPID used in the present study was consistent with available literature.

To test linearity, EPID images were acquired for an open 20 x 20 cm^2 field for a range of doses. The values of the central 100 pixels (4 x 4 mm^2) were averaged for each image. As shown in Figure 2.3, EPID response was found to increase linearly with MU, which is consistent with the results reported by other authors (Renner 2005; van Elmpt 2008).

A second test quantified the stability in response for successive images taken by the EPID for identical beam parameters. A simple test of reproducibility was desired to get a general sense of variation from one image to the next for identical beams and field sizes. For each of three square field sizes (3 x 3 cm^2, 10 x 10 cm^2, and 20 x 20 cm^2), 100 MUs were

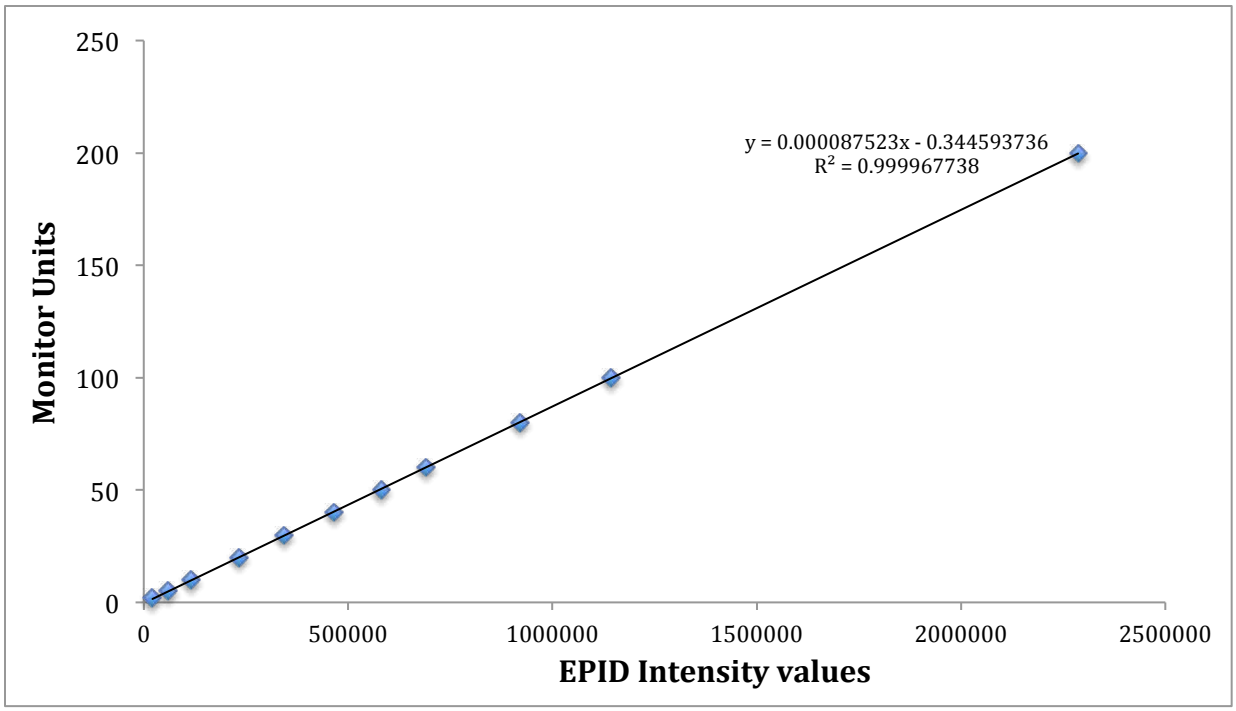

Figure 2.3. Plot of MUs versus the average central axis EPID intensity values. All beams were delivered with an open beam and 10 x 10 cm^2 field size. Measurement uncertainty was smaller than the plotting symbol size.

delivered with an open beam three times, and EPID images were recorded. The central axis pixel values for the three images of each field size were averaged over a 4 x 4 mm^2 area. Table 2.1 revealed that the EPID's response uncertainty in all cases was <0.3%, which is consistent with published findings (Winkler Georg 2006).

Table 2.1. Central axis pixel values for EPID images taken in order to test the reproducibility of the EPID for identical beam and field parameters.

Field Size (cm^2)	Image 1 (intensity)	Image 2 (intensity)	Image 3 (intensity)	Average (intensity)	Std. Dev. (intensity)	% Frac. Unc. (100*(Avg/Std Dev))
3X3	1024500	1023400	1021500	1023133	1239	0.121
10X10	1153750	1153600	1159900	1155750	2935	0.254
20X20	1232600	1239200	1234800	1235533	2744	0.222

A third test investigated the response of the EPID to changes in field size. The response of the EPID under these conditions was also compared against ion chamber measurements performed on central axis at the source-to-detector-distance (SDD) of the EPID. The ion

chamber was a PTW 0.6 cc farmer chamber (serial: TN30013 – 0579, PTW – New York, Brooklyn, NY) and was used with a CNMC Instruments Model 206 electrometer (serial: 11207335, CNMC Company, Nashville, TN). The phantoms were flat slabs of plastic water positioned with their midline depth at isocenter. Figure 2.4 compares the response of the EPID (black triangles) and ion chamber (red squares) to changes in field size for an unattenuated (*i.e.*, no phantom) beam. Each data set was normalized to the value for the 10 x 10 cm^2 field size.

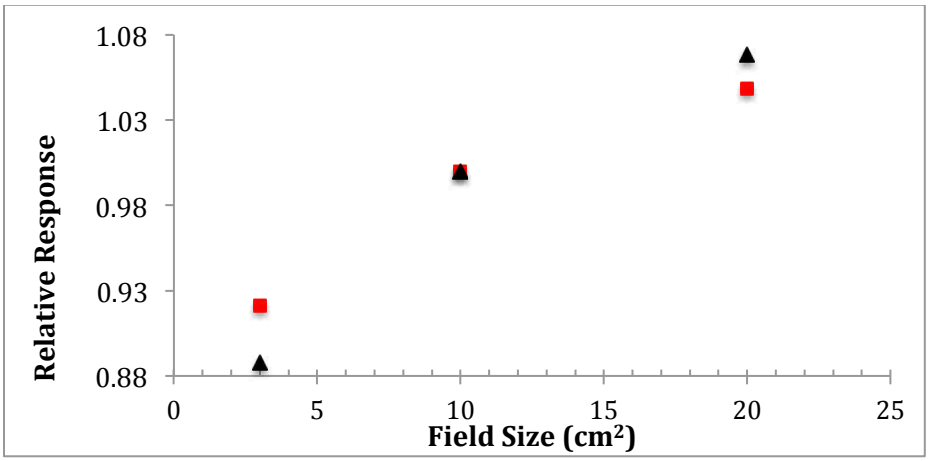

Figure 2.4. The response of the EPID to field size. EPID (black triangles) intensity change with field size is compared to the change in signal measured with an ion chamber (red squares). The chamber was placed at the position of the EPID with 1.5 cm plastic water buildup and 3 cm plastic water behind for backscatter. Both data sets are normalized to the 10x10 cm^2 field.

EPID and ion chamber response were observed to increase with field size; however, the EPID showed a greater response with field size compared with the ion chamber. These findings were similar to the findings of other authors (Greer Popescu 2003; Renner 2005; Liebich 2011), who generally attributed the EPID response to influence from the phosphor layer, which increased the field size response relative to ion chamber (Greer 2011). Greer *et al.* suggested that the high atomic number of the EPID phosphor layer produces greater sensitivity to low energy scattered radiation, which increases with field size (Greer Popescu 2003). Gustafsson *et*

al. conducted experiments with and without the phosphor layer of the EPID in place, and with and without blocking of the optical photons with an opaque sheet. They showed that the phosphor layer caused an increased field size dependency of the EPID to a 6 MV beam relative to the measurements made without the phosphor layer, but did not differentiate between the effects of energy dependence and optical scatter and reflection or "glare" in the phosphor (Gustafsson 2009). Blake *et al.* studied the effects of glare within the phosphor with Monte Carlo simulations and found no significant difference in the field size response when the optical spread was modeled compared to a model without optical spread (Blake 2013).

A fourth test investigated the response of the EPID to changes in broad beam attenuation. The response of the EPID under these conditions was also compared against ion chamber measurements. The ion chamber and electrometer used in the third test were again used. Measurements were taken for phantom thicknesses of 0 cm (no phantom), 10 cm, and 20 cm thicknesses. The phantoms were placed with their midline at isocenter and the relative response of ion chamber and EPID measurements were compared for field sizes of 3 x 3 cm^2 and 20 x 20 cm^2 (Figure 2.5). Each data set was normalized to the value for the 10 cm phantom. EPID and ion chamber response were observed to decrease with phantom thickness, with the EPID again showing a greater change in response over the interval of phantom thicknesses studied. These findings are consistent with those reported by other authors (Kirkby 2005; Renner 2005; Nijsten 2007). The increased change in response of the EPID relative to the ion chamber was shown to be the result of energy spectrum changes associated with attenuation,

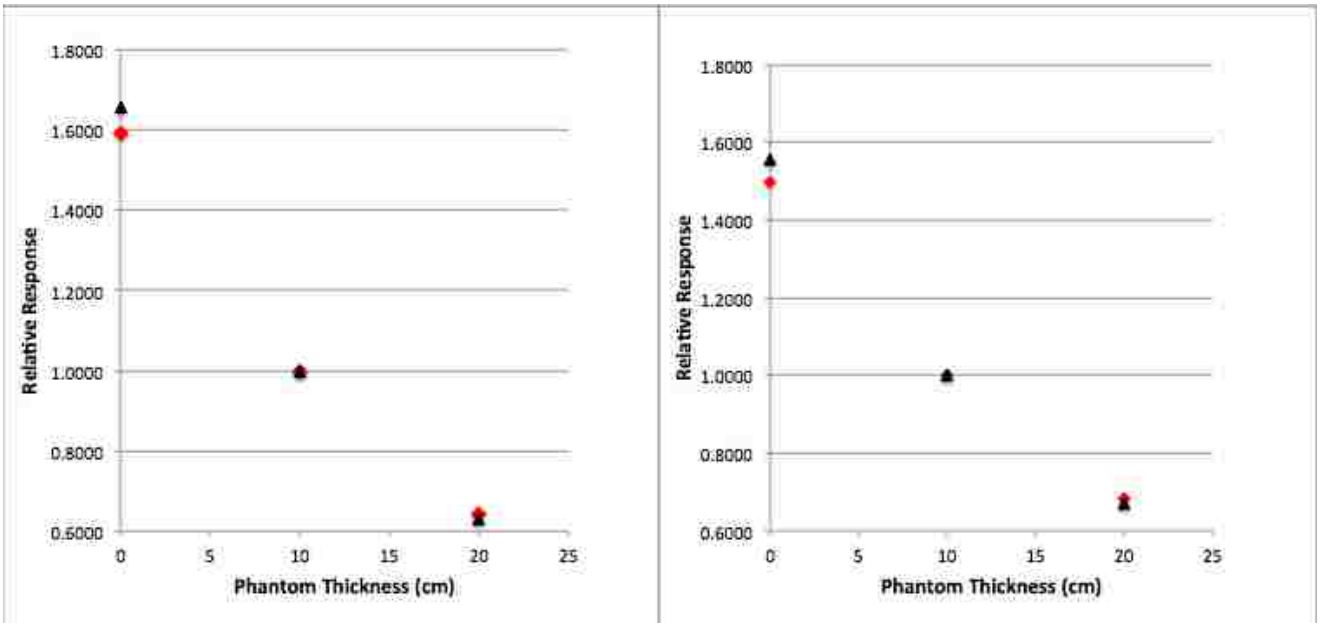

Figure 2.5. The response of the EPID to phantom thickness for a 3x3 cm^2 (left) and a 20x20 cm^2 (right) field size. EPID intensity change with phantom thickness (black) is compared to the change in signal measured with an ion chamber (red). The chamber was placed at the position of the EPID with 1.5 cm plastic water buildup and 3 cm plastic water behind for backscatter. Both data sets are normalized to the 10 cm phantom thickness.

as the EPID shows a marked increase in energy response to photons below 1 MeV, which are more abundant in the beam without the phantom, and preferentially attenuated in the transmission material (Kirkby 2005; Parent 2006; van Elmpt 2008). The change in response of the ion chamber with phantom thickness was due largely to the overall attenuation of photons. The change in response of the EPID to phantom thickness was also due to the attenuation of photons, but the lower energy photons (to which the EPID has an increased response) were attenuated in greater proportion, causing an increased change in the EPID's response relative to the ion chamber.

2.3 AIM1, DEVELOPMENT OF A METHOD OF EPID TRANSIT IMAGE PREDICTION

2.3.1 PIXEL SPECIFIC SCATTER KERNELS MODELED WITH MONTE CARLO

To predict transit images from through-air images, the scatter and attenuation that result from interactions of radiation with the patient and within the EPID must be accounted for. This was achieved by convolution of each pixel of the through-air image with radiological pathlength-specific pencil kernels, followed by a superposition of the convolution results for all pixels of the detector. Pencil kernels were simulated using Monte Carlo (Monte Carlo N-Particle eXtended, version 2.6d) with a 0.4 x 0.4 mm^2 parallel beam of 6 MV polyenergetic x-rays normally incident through a slab of water upon a detailed model of the Elekta EPID. The beam energy spectrum was originally taken from published data (Sheikh-Bagheri Rogers 2002) and modified to match clinical depth dose data for dose in water (Figure 2.6).

Percent depth doses (PDDs) for 1 x 1 cm^2 and 10 x 10 cm^2 field sizes generated with Monte Carlo simulations were compared with the clinical PDD for the linear accelerator used in this work to ensure consistency. The energy spectrum was iteratively modified with a ramp filter by adjusting the slope until good agreement was reached between the simulation PDD's and the clinical PDD's. The data points for all depths from 2.05 – 29.95 cm show agreement of 3% or better (Table 2.2).

The simulations transported photons through a vacuum and some thickness of water, ranging from 0 to 300 mm. The water slab was positioned isocentrically at 100 cm and the emerging photons impinged upon an 80 x 80 cm^2 grid with 4 x 4 mm^2 grid elements.

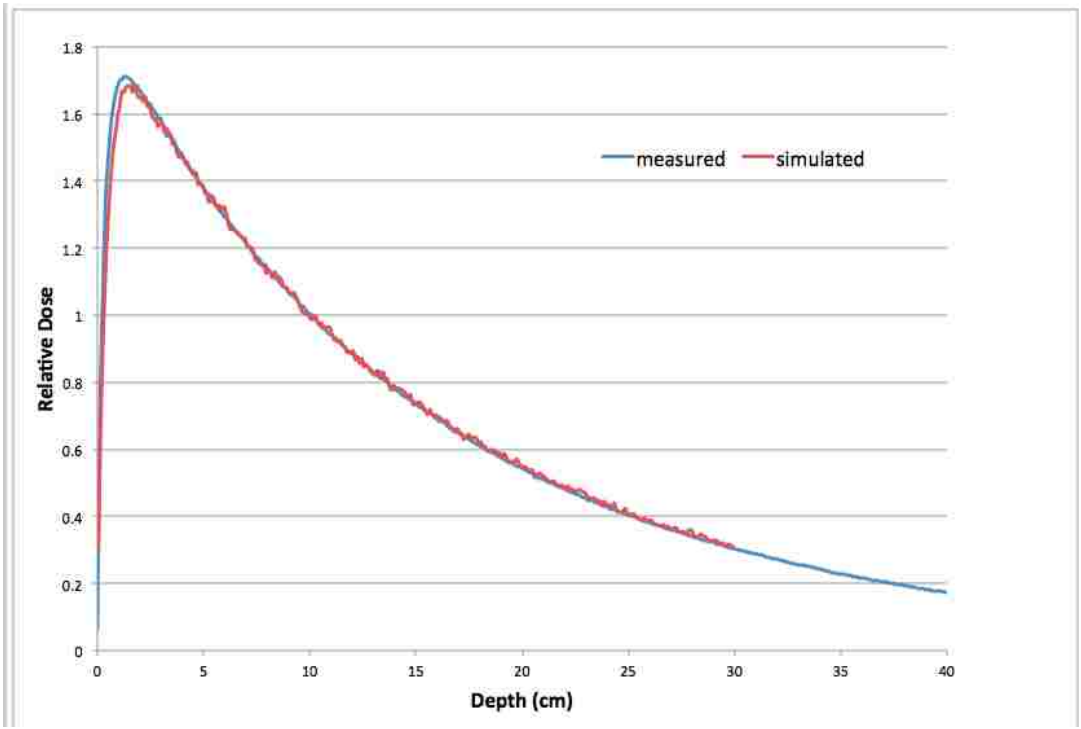

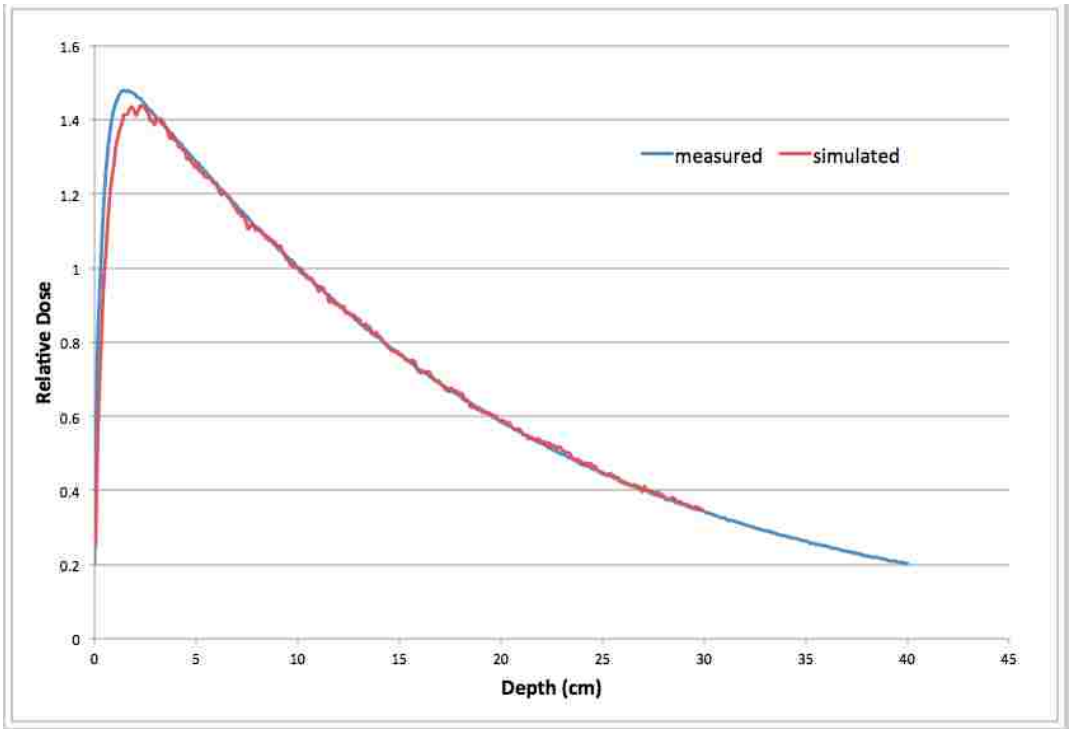

Figure 2.6. Spectra for (above) a 1 x 1 cm^2 field size, and (below) a 10 x 10 cm^2. Red: simulated results from modified published spectrum; Blue: clinical data from the Elekta Infinity linac.

Table 2.2. PDD differences for the linear accelerator used in this study and the spectrum used for modeling. Left: 1 x 1 cm^2 field size; Right: 10 x 10 cm^2 field size.

Depth (cm)	Dose Difference (%)	Depth (cm)	Dose Difference (%)
0.55	15.23	0.55	17.25
1.05	4.70	1.05	8.16
1.55	0.75	1.55	4.40
2.05	0.28	2.05	0.93
2.55	0.64	2.55	0.39
3.05	-0.68	3.05	0.17
4.05	-0.60	4.05	0.07
5.05	0.05	5.05	2.73
7.55	0.26	7.55	0.22
10.05	0.83	10.05	0.15
12.55	0.49	12.55	0.39
15.05	-1.29	15.05	-0.16
18.05	-2.48	18.05	-2.38
22.05	-0.83	22.05	-1.54
26.05	-2.53	26.05	0.21
29.95	-1.52	29.95	-1.70

The impinging photons account for primary fluence attenuation and scatter stemming from interactions with the patient and EPID. The EPID was modeled using rectangular layers of the materials listed in Table 2.3 Specifications for the copper and phosphor layers were taken from Blake *et al* (Blake 2013), while the remaining layers were estimated from literature (Parent 2006). The phosphor layer of the EPID was modeled at a distance of 160 cm from the source. Dose deposited in the phosphor was scored from electrons generated in the EPID materials resulting from interactions of the incident photons and from direct photon/phosphor interactions. Figure 2.7 shows a plot of the dose deposited per particle in the phosphor as a function of distance from the central axis for 10, 100, 200, and 300 mm water transmission. Approximately 2.5 x 10^8 histories were generated for each simulation yielding an average uncertainty of 9% across all points, and 0.06% uncertainty for the central point. Pencil kernels were generated for water thicknesses of 0 mm to 300 mm in 5 mm increments.

Table 2.3. Thickness and density information for modeled Elekta iViewGT EPID layers

Layer	Thickness (mm)	Density (g/cc)
Polystyrene	9.00	1.03
Aluminum	1.13	2.70
Copper	1.00	8.96
Graphite	0.63	2.26
Phosphor	0.29	4.59
a-Si	0.10	2.20
Glass	1.00	2.40
Carbon Fiber	1.50	1.65
Aluminum	1.50	2.70
Copper	1.00	8.96
Glass	1.00	2.40
Aluminum	1.13	2.70
Polystyrene	9.00	1.03

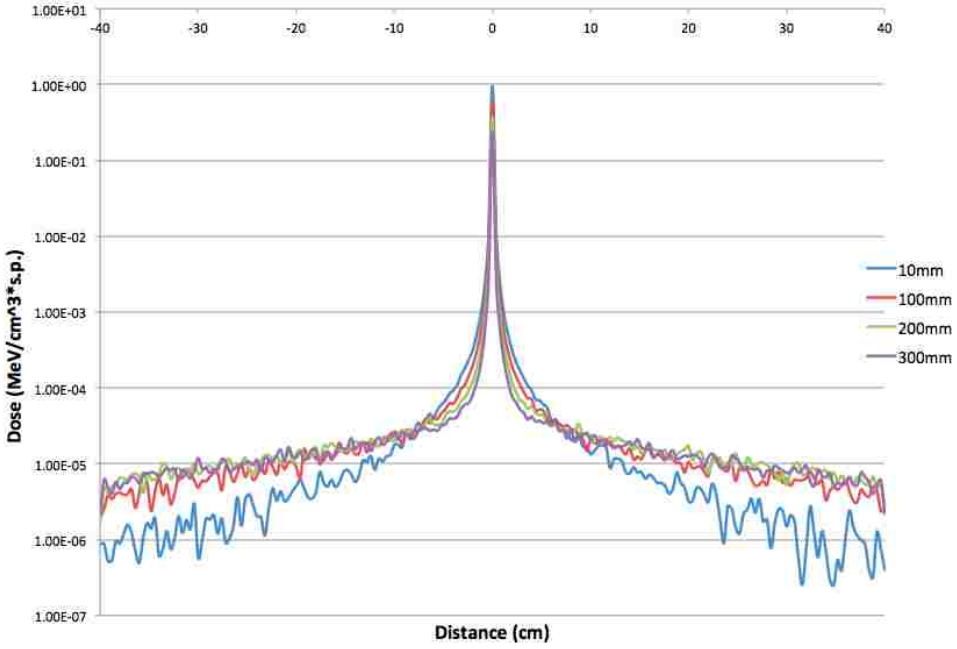

Figure 2.7. Pencil beam kernels for 10, 100, 200, and 300 mm transmission through water. The figure is a plot of dose deposited per source particle (s.p.) in the phosphor of the EPID as a function of distance from the central axis.

Linear interpolation was used to determine intermediate thicknesses. In this way, a library of precalculated pencil kernels was generated that was later used in the transit image prediction process.

2.3.2 CALCULATION OF RADIOLOGICAL PATHLENGTH

Selection of the proper pencil kernel for each EPID pixel required knowledge of the radiological pathlength between the source and the pixel of interest. The method for calculating the radiological pathlength for each detector pixel was based upon Siddon's algorithm (Siddon 1985). The algorithm was written in MATLAB (Mathworks, Natick, MA), and calculates the radiological pathlengths from computed tomography data. The program uses parametric line and plane equations to calculate radiological pathlength from a point source, through a patient or phantom, and terminating at a detector element of the EPID (Figure 2.8).

In the algorithm, the three-dimensional grid of CT voxels were represented by three sets of orthogonal planes, and the line of each ray trace corresponded to a parametric line that originated at the source and terminated at the plane of the detector. The radiological pathlengths were calculated by referencing the CT number to density conversion table for the 16 slice GE Lightspeed scanner contained in the Pinnacle treatment planning system.

The raw 12-bit grayscale CT numbers were imported by the program and downsampled from 512 x 512 to 256 x 256 voxels to reduce calculation time. To minimize the influence of the air between the source and detectors in the CT, a threshold of 50 above the minimum was set for CT numbers below which the density for that voxel was calculated as zero. In this way, the "air pixels" did not contribute to the radiological pathlength. The CT numbers were converted

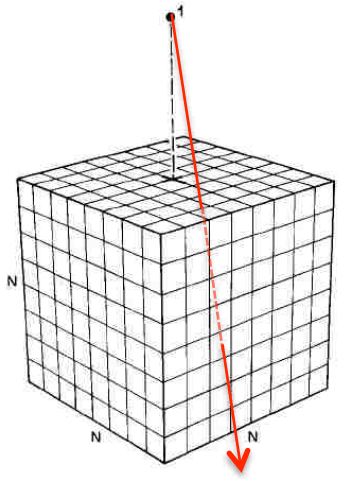

Figure 2.8. Diagram of ray trace geometry. Adapted from Siddon, 1985.

into densities, and the exact physical pathlength (*l)* through each voxel(*i,j,k*) is calculated. Each voxel was then assigned its corresponding density, *ρ,* and the radiological pathlength for all voxels along the ray trace were summed:

$$d = \sum_i \sum_j \sum_k l(i,j,k)\, \rho(i,j,k). \qquad [2]$$

The radiological pathlengths were calculated from the CT images and the EPID geometry for each element of the detector assuming a source-to-detector distance of 159 cm from the linac target, a 40.96 x 40.96 cm^2 sensitive area, and array size of 1024 x 1024 (pixel pitch = 0.4 x 0.4 mm). Each radiological pathlength was rounded to the nearest millimeter for kernel selection purposes.

2.3.3 AQUISITION OF THROUGH-AIR IMAGES

All fields were delivered with an Elekta Infinity linear accelerator (Elekta Ltd, Crawley, West Sussex, United Kingdom) and measured with the Elekta iViewGT EPID (Figure 2.9). The iView software (Elekta, version 3.4) was used to capture and export the images in DICOM format. The iView software applies a global scaling factor to each image to produce a

consistent maximum intensity value that is independent of MU and attenuation. This results in a consistent image appearance that is useful for image guidance but not optimal for measuring changes in fluence. Thus, the scaling factor of each image was retrieved and used to "un-normalize" each measured image. In addition, EPID images are initially inverted for optimal positional verification. The images were therefore inverted prior to dividing them by the pixel scaling factor in order to restore the pixel intensities to their raw values (Renner 2005).

Figure 2.9. Setup for the beam delivery for the Elekta linac with iView EPID. All beams for this study were delivered laterally to minimize transmission through the couch.

2.3.4 FLOOD FIELD AND DARK FIELD CORRECTIONS

To address the intensity profile mismatches seen in preliminary data, flood-field (FF) and dark-field (DF) corrections had to be addressed. The DF image is an image taken while no radiation is delivered and accounts for the individual pixel background signals. The FF image is an open field image delivered to the entire sensitive area of the imager that accounts for individual pixel sensitivities (Grattan McGarry 2010). To enhance image quality for patient positioning purposes, the EPID software automatically applies FF and DF corrections (Louwe

2004; Parent 2007). The raw image pixel intensity (I_{raw}) is first corrected by the subtraction of the DF image intensity. The subtracted image is normalized by the FF image. These corrections can be represented mathematically by:

$$I(x,y) = \left(\frac{[FF(x,y) - DF(x,y)]_{mean}}{FF(x,y) - DF(x,y)} \right) * \left(I_{raw}(x,y) - DF(x,y) \right) \quad [3]$$

where the quantity in brackets is a single value found by averaging the differences between the FF pixel values and their corresponding DF values (Louwe 2004; Parent 2007). This correction is applied to the images automatically at the time of measurement from FF and DF images stored with the iView software.

To obtain the raw image values prior to processing, the open field images were flood-field and dark-field "uncorrected". The values for the initial raw intensities (I_{raw}) were found by reversing the corrections made in equation 3. After the raw images were processed with the pencil beam kernels, the FF and DF corrections were reapplied so that the predicted transit images could be compared directly to the measured transit images.

2.3.5 CONVOLUTION OF THROUGH-AIR IMAGES WITH PENCIL BEAM KERNELS

After through-air images were acquired, they were processed to obtain predicted transit portal images. Each pixel value was convolved with a pencil beam kernel corresponding to the radiological pathlengths (*d*) calculated from the phantom or patient CT data. A pencil kernel ($K_{(d)}$) was selected for each radiological pathlength from the previously calculated library. Once an array of kernels was mapped for all detector elements, the open field image was deconvolved with a zero thickness kernel ($I_{raw,deconv}$). The deconvolution removed the dose

deposition blurring that was present in the through-air image. The deconvolved image pixels were then convolved with the pathlength specific kernels to produce a predicted image:

$$P = \sum_i \sum_j (I_{raw,deconv(i,j)} \otimes K_{(d)}) \quad [4]$$

To test the accuracy of the dose response characteristics of the pencil kernels, the deconvolved, through-air EPID central axis pixels for a 3 x 3 cm^2, 10 x 10 cm^2, 20 x 20 cm^2 field size image were compared with ion chamber measurements for central axis measurements taken at 160 SDD (Figure 2.10). Since the dose deposition kernel accounts for the dose response characteristics of the modeled EPID, the deconvolved signal should be consistent with an ideal detector (if properly modeled), and should therefore compare closely with the ion chamber measurements whose energy response is very linear (McEwen 2001). The deconvolved central axis pixel response for the 3 x 3 cm^2 and 20 x 20 cm^2 field sizes were within 1% of the ion chamber readings, relative the 10 x 10 cm^2 measurements.

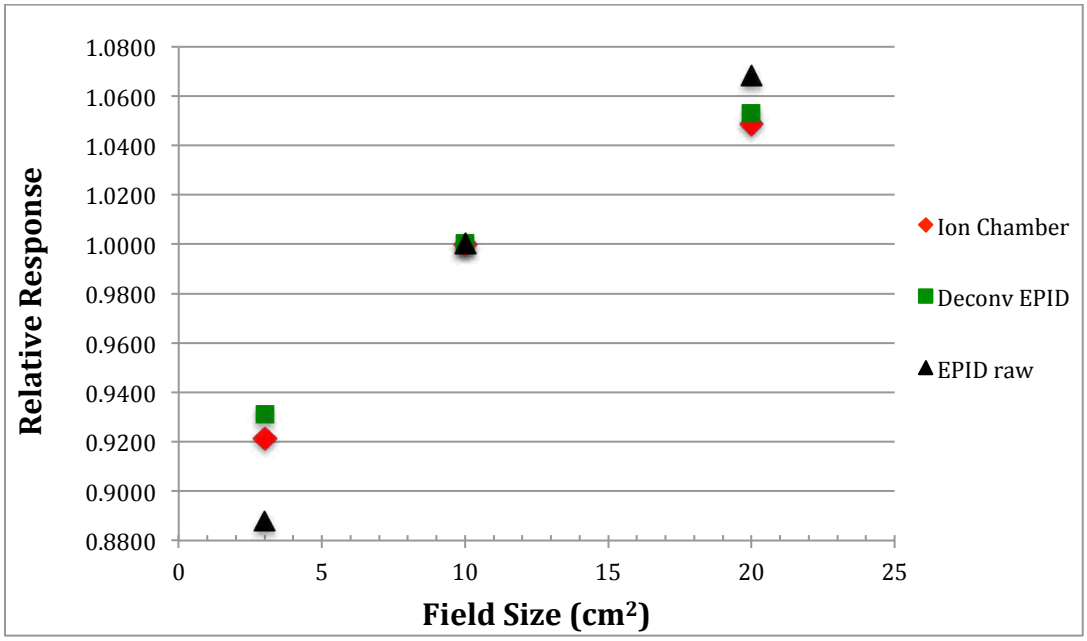

Figure 2.10. Through-air response for ion chamber (red), raw EPID (black), and deconvolved EPID (green) central axis pixels. All values are normalized to the respective 10 x 10 cm^2 field size.

2.4 AIM 2, SIMPLE HOMOGENEOUS PHANTOMS

2.4.1 COMPARISON OF TRANSIT PORTAL IMAGES TO PREDICTED IMAGES

Transit images were measured in the same manner as the through-air images, with the exception of the phantom's or patient's placement in the beam path. The goal of this study was to test the feasibility of the method for isocentric treatments, so phantoms were placed symmetrically at the isocenter. Identical geometry was used for the water slabs modeled with MCNPX. In addition, non-isocentric treatments where the field shape is not centered on the isocenter could require further analysis. This topic has been addressed in other literature (Cilla 2013).

After acquisition of the treatment image, gamma analysis was used to compare the predicted transit images with measured transit images. Treatment images were inverted and scaled in the same fashion as the open beam images. The gamma analysis was performed with an in-house program[1]. For the tests that used phantoms with regular shapes and sizes, a 3%/ 3 criteria was used, similar to that used in other published works (Van Esch 2004; Bedford 2014).

2.4.2 ASSESSMENT WITH UNIFORM PLASTIC SLABS

Figure 2.9 shows the setup for the initial testing of the prediction method was carried out with a simple, single lateral field on blocks of Plastic Water® (ρ=1.039 g/ CM^3, CIRS, Norfolk, Virginia). Plastic water thicknesses of 5cm, 10 cm, 15 cm, 20 cm, and 25 cm were used with 3 x 3 cm^2, 5 x 5 cm^2, 10 x 10 cm^2, 15 x 15 cm^2, and 20 x 20 cm^2 square fields. These fields and phantom thicknesses were chosen to observe the effects of various radiological pathlengths

[1] Written by Gordon Mancuso, M.S.

and field sizes on the EPID transit dosimetry method. A 6 MV, lateral (gantry angle = 90^{o}) beam delivered 100 MU at 400 MU/min for each through-air and transit image. The beam for each of the five field sizes was first delivered through-air to obtain the images for processing. The plastic slabs were then individually placed, and positioned with their midline depth at isocenter, and the center of the field aligned to the center of the phantom for measurement of the corresponding transit image.

Radiological pathlengths for each phantom thickness were calculated from CT scans. The CT data was collected with a 120 kVp beam helical scan with 2.5 mm slice thickness. Initial evaluation of the predicted transit images indicated the presence of profile shape and central axis value differences between predicted and measured intensity profiles. There were also indications that these mismatches were dependent upon both the field size and the thickness of plastic water traversed. The next two sections describe corrections that were applied to achieve agreement between the predicted and measured profiles for the range of plastic water thicknesses and field sizes.

2.4.3 FIELD SIZE CORRECTION

Inaccuracies in the overall image intensities of the predicted images were noted in the preliminary data (Figure 2.11). The magnitude of the error was linear with field size, and was more pronounced in the thicker phantom predictions. The discrepancies in the predicted and measured intensities were attributed to the spectral dependencies on field size and phantom thickness that were not modeled in the pencil kernel convolution process (Kirkby 2005), as well as possible inaccuracies in the EPID layer dimensions and in modeling of the input spectrum.

These topics are addressed in more detail in the Discussion and Conclusions chapter (section 4.2).

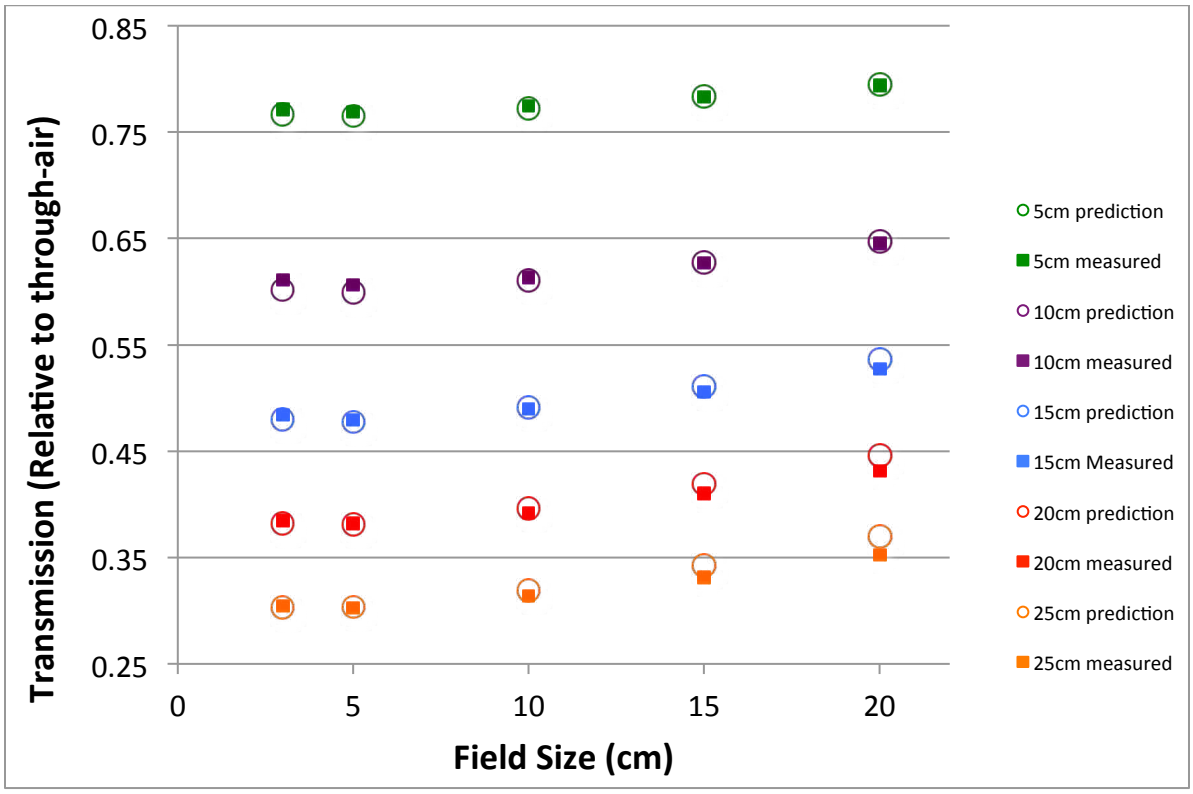

Figure 2.11. Measured (solid squares) and predicted (open circles) central axis region intensity values for various plastic water phantom thicknesses plotted vs. field size.

An analytical correction was implemented in which the radiological pathlength of the ray trace determines the slope (*m)* and intercept (*b*) of the linear field size (*FS*) correction by:

$$correction\ factor = 1 + \frac{(m * FS + b)}{100}. \qquad [5]$$

Values of slope and intercept were determined in a two-step process. First, the average predicted intensities for the central 100 pixels were compared to the measured values for all field sizes with a particular phantom. The differences were plotted and fit with a least-squares method to lines. The process was repeated for all phantom thicknesses. The slopes and

intercepts of the best-fit lines were then plotted versus the radiological pathlengths. Best-fit quadratic curves were determined and used to interpolate the slope and intercept values for arbitrary radiological thicknesses. Correction parameters for several radiological thicknesses are listed in Table 2.4. In practice, for each pixel the slope and intercept are determined from the calculated radiological pathlength. The correction factor is then calculated for the field size and the pixel value of the predicted transit image is multiplied by the correction factor.

Table 2.4. Coefficients for the correction factors applied in Equation 5.

Radiological Thickness (g/cm2)	m	b
51.6	-0.0411	0.7101
104.5	-0.1079	1.7118
155.5	-0.1515	1.2383
207.2	-0.2449	1.4324
259.6	-0.3145	1.3466

2.5 AIM 2, HOMOGENEOUS PHANTOM WITH COMPLEX GEOMETRY

For Aim 2, the EPID transit dosimetry method was evaluated with a phantom of non-uniform thickness (150 mm to 220 mm), shown in Figure 2.12. For this case, the same plastic water material was used. Beam delivery was again a single lateral beam with the set of 3 x 3 cm^2, 5 x 5 cm^2, 10 x 10 cm^2, 15 x 15 cm^2, and 20 x 20 cm^2 square fields (Figure 2.13). A 6 MV, lateral (gantry angle = 90^o) beam delivered 100 MU's at 400 MU/min for each through-air and transit image. The beam for each field size was first delivered through-air. The phantom was then placed and positioned isocentrically; the center of the field was aligned to the center of the phantom for measurement of the transit image. A CT scan of the phantom was used to calculate the radiological pathlengths for all detector elements. The CT data was collected with

a 120 kVp beam helical scan with 2.5 mm slice thickness. Figure 2.14 shows examples for the measured and predicted transit images.

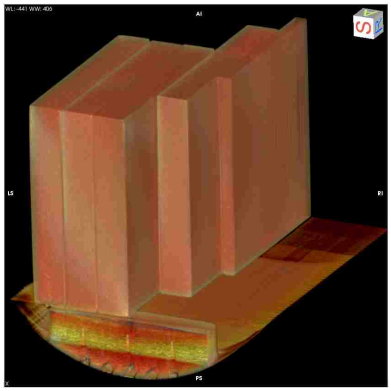

Figure 2.12. 3D representation of the phantom used for Aim 2, which was generated from CT data in Osirix (v3.8, Osirix Imaging Software).

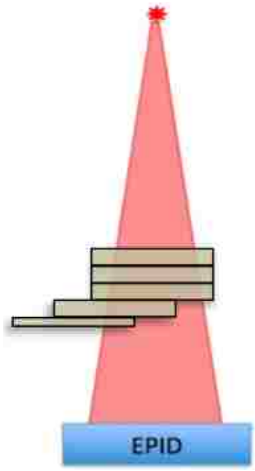

Figure 2.13. Basic beam orientation for homogeneous phantom with complex geometry (not to scale).

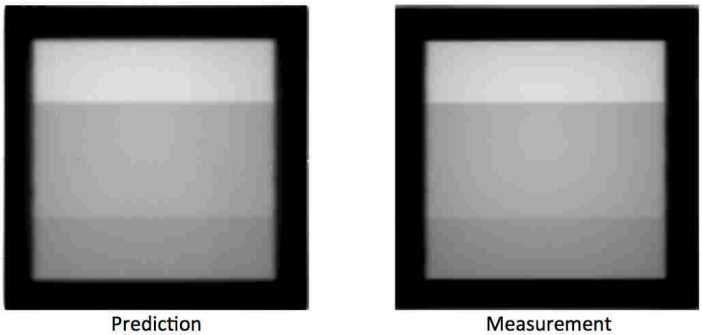

Figure 2.14. Predicted and measured transit images for homogeneous phantom with complex geometry for a 20 x 20 cm^2 field.

A 3%/ 3 mm gamma index of the predicted and measured images was used to gauge the accuracy of the predicted transit images. For dose difference comparisons, the individual pixel differences for measured and predicted images were compared relative to the global maximum pixel value in the field, rather than the local value (Dyk 1993). Only points above a threshold of 10% of the maximum intensity were analyzed, so that only predicted and measured image pixels within the irradiated field were compared.

2.6 AIM 3, CYLINDRICAL HETEROGENEOUS PHANTOM

The transit dosimetry method was further validated for a heterogeneous phantom of cylindrical geometry. Patient treatments require accurate dose predictions for heterogeneous tissues and irregular geometries (Figure 2.15). The phantom (CT Head, Nuclear Associates/Fluke Biomedical 76-414-4150, Fluke Biomedical, Everett, WA) was a polymethl methacrylate cylinder that measured 16 cm in diameter and 15 cm long. The phantom contained cylindrical internal air cavities (1.31 cm diameter) oriented parallel to the cylinder axis, which provided a simple test of the effects of heterogeneities on the accuracy of the method.

Once again, a 6 MV lateral (gantry angle = 90^{o}) beam delivered 100 MU at 400 MU/min for each through-air and transit image. Field sizes of 3 x 3 cm^2, 5 x 5 cm^2, 10 x 10 cm^2, 15 x 15 cm^2, and 20 x 20 cm^2 were used to compare measured and predicted images. The beam for each field size was first delivered through-air. The phantom was then placed on the couch and positioned isocentrically so that the cylinder's axis coincided with the axis of rotation of the gantry. Radiological pathlengths for all detector elements were then calculated from CT data. The CT data was collected with a 120 kVp beam helical scan with 2.5 mm slice thickness.

The initial results of the cylindrical phantom showed a global overestimate of approximately 5% in the prediction of the transit images for all fields. The density of the PMMA phantom material obtained from the scanner's CT number-to-density conversion table was substantially lower (by 6.7%) than the published density from the manufacturer (1.19 ± 0.01 g/cm^3). To improve the accuracy of the density calculation, additional points were added to the CT number-to-density conversion table. The points were added from a CT QA phantom (Nuclear Associates 76-410-4130) with published densities for the compositional materials. The phantom was scanned and the average measured CT numbers were combined with published densities to supplement the table.

A 3%/ 3 mm gamma index of the predicted and measured images was used to gauge the accuracy of the predicted transit images. For dose difference comparisons, the individual pixel differences for measured and predicted images were compared relative to the global maximum pixel value in the field, rather than the local value (Dyk 1993). Only points above a threshold of 10% of the maximum intensity were analyzed, so that only predicted and measured image pixels within the irradiated area were compared.

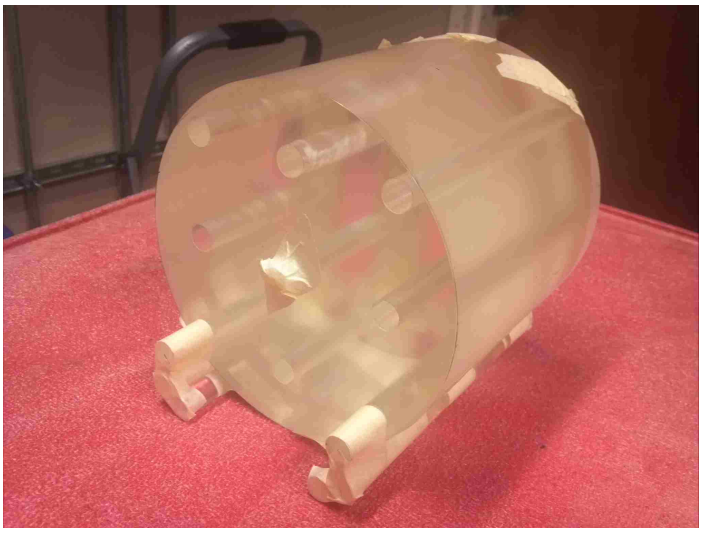

Figure 2.15. Heterogeneous cylinder phantom used for Aim 3.

2.7 AIM 4, ANTHROPOMORPHIC HEAD PHANTOM

The accuracy of the transit dosimetry method was evaluated for a case that resembled a patient, using an anthropomorphic head phantom (RSD Rando ART-210 Head and Neck Phantom, Radiology Support Devices, Long Beach, CA), shown in Figure 2.16.

A 6 MV lateral (gantry angle = 90^{o}) beam delivered 100 MU at 400 MU/min for each through-air and transit image. Field sizes of 3 x 3 cm^2, 5 x 5 cm^2, 10 x 10 cm^2, 15 x 15 cm^2, and 20 x 20 cm^2 were used to compare measured and predicted images. The beam for each field size was first delivered through-air. The phantom head was then placed on the couch and positioned so that the phantom's approximate geometric center was placed at isocenter, giving an SSD of 91.6 cm and the center of the field was aligned to the center of the phantom for measurement of the corresponding transit image. Radiological pathlengths for all detector elements were calculated from CT data of the phantom. The CT data was collected with a 120 kVp beam axial scan with 1.25 mm slice thickness.

Gamma analysis of the predicted and measured transit images was used to gauge the accuracy of the predicted transit images. 3%/ 3 mm criteria were used for all phantoms except the anthropomorphic head phantom. For the anthropomorphic head phantom, a 5%/ 3 mm gamma index was used to allow for the complex geometry and heterogeneities of the patient-like head phantom. For dose difference comparisons, the individual pixel differences for measured and predicted images were compared relative to the global maximum pixel value in the field, rather than the local value (Dyk 1993). Only points above a threshold of 10% of the maximum intensity were analyzed, so that only predicted and measured image pixels in the irradiated field were compared.

In order for a dosimetry method to have clinical value, it must be able to detect errors that would cause failure of points under a 5%/ 3 mm gamma index criteria (Kutcher 1994; Childress 2005). Five percent accuracy represents the minimum level needed for a treatment to comply with AAPM Task Group Report 40 and the ICRU's recommendations (see Section 1.1).

Figure 2.16. Anthropomorphic head phantom used in Aim 4 (RSD Rando ART-210 Head and Neck Phantom, Radiology Support Devices, Long Beach, CA).

CHAPTER 3: RESULTS

3.1 RADIOLOGICAL PATHLENGTH CALCULATIONS

Radiological pathlengths calculated by the code described in Section 2.3.2 were compared with known values for a 30x30x5 cm^3 solid water phantom (Figure 3.1 and Figure 3.2).

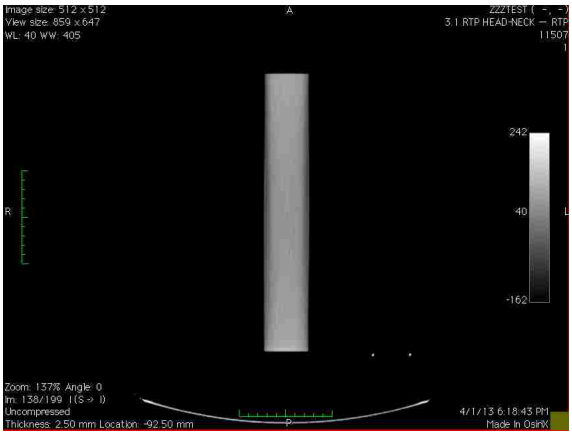

Figure 3.1. 5 cm plastic water block CT slice.

The published density of the plastic water was 1.039 g/cm^3, and the thickness was measured to be 5.00 cm at the center. The radiological pathlength through the center axis (CAX) of the block was calculated by the prototype code as 5.27 g/cm^2 with some variation in

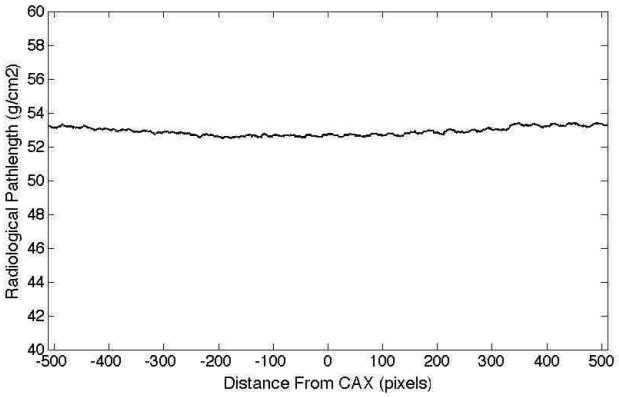

Figure 3.2. Profile of the radiological pathlengths calculated for a 5 cm homogeneous plastic water phantom.

the density (± 5%) based upon the CT numbers standard deviation from the scan. This calculated radiological pathlength was compared with a manually determined value through the center of the phantom. The geometric difference in these distances is negligible. The values obtained for the manually calculated and Matlab predicted radiological pathlengths (5.2676 g/cm^2 and 5.2687 g/cm^2, respectively) were within the range of uncertainty of the CT measurement. The relative difference between the radiological pathlength estimated from the published density and measured thickness and the Matlab predicted thickness is 2.3%.

The difference in radiological pathlengths calculated in the Matlab program between the center of the phantom and the edge in the central row was 0.0911g/cm^2, or 1.7%. This value is consistent with the expected change in pathlength that would result from the geometric pathlength difference. Figure 3.3 displays an example of the difference in the

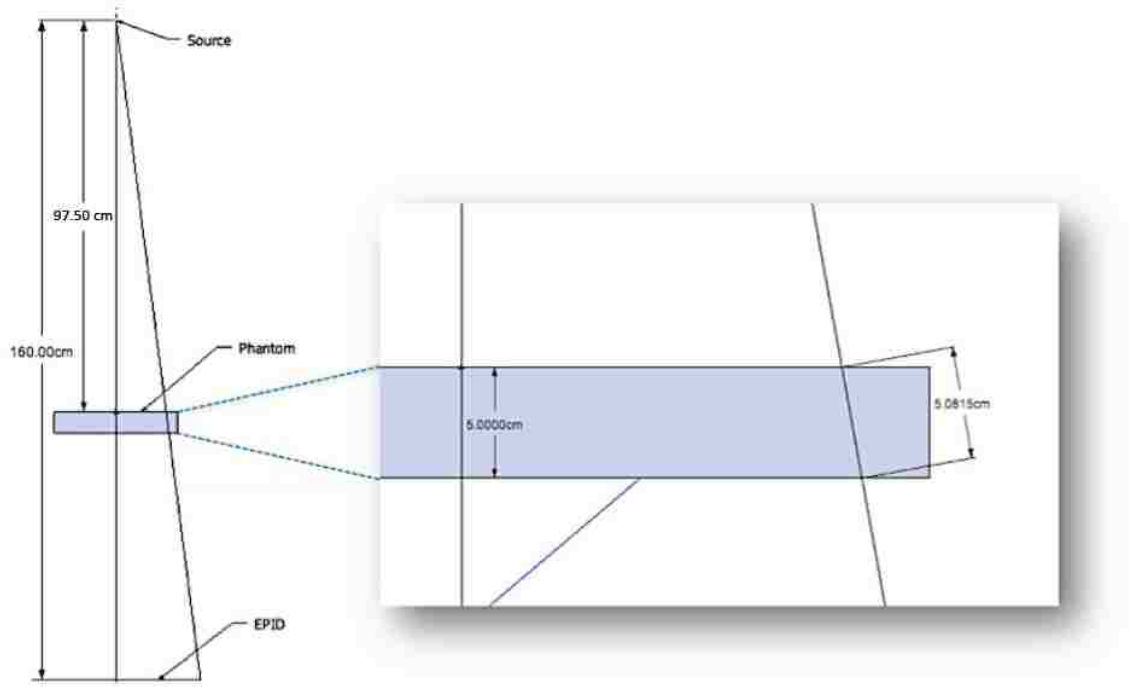

Figure 3.3. Geometric pathlengths through the 5 cm phantom for rays through the center of the block and at its edge. (Left: full diagram, Right: enlarged view)

physical pathlength along the CAX of a 5 cm flat block of plastic water compared to the pathlength at the edge of the EPID detector array. For the EPID geometry, this difference corresponds to a pathlength increase of 0.82 mm or 1.6% for the 5cm block. The difference in pathlength calculated by the MATLAB program (1.7%) and the difference in the physical pathlength from the problem geometry (1.6%) are identical to within statistical uncertainty.

3.2 RESULTS FOR AIM2: SIMPLE HOMOGENEOUS PLASTIC SLABS

Gamma analysis was performed after the correction factors were determined and applied for predicted transit images. Analysis was performed for each field size and thickness of phantom tested. The number of passing points for each case is shown in Table 3.1. The corrections accounted for the field size and thickness dependencies seen in the original predictions. Failure points that were produced were found near the edges of the large fields, as seen in the image on the right of Figure 3.5 with associated predicted and measured transit image profiles in Figure 3.4.

Table 3.1. 3%/ 3 mm Gamma analysis passing rates for calibration phantoms

	Field Size					
Phantom	3 x 3	5 x 5	10 x 10	15 x 15	20 x 20	Average
Plastic Water, 5cm	100.0	100.0	100.0	100.0	100.0	100.0
Plastic Water, 10cm	100.0	100.0	100.0	100.0	100.0	100.0
Plastic Water, 15cm	100.0	100.0	100.0	100.0	98.4	99.7
Plastic Water, 20cm	100.0	100.0	100.0	100.0	95.7	99.1
Plastic Water, 25cm	100.0	100.0	100.0	99.1	94.2	98.7

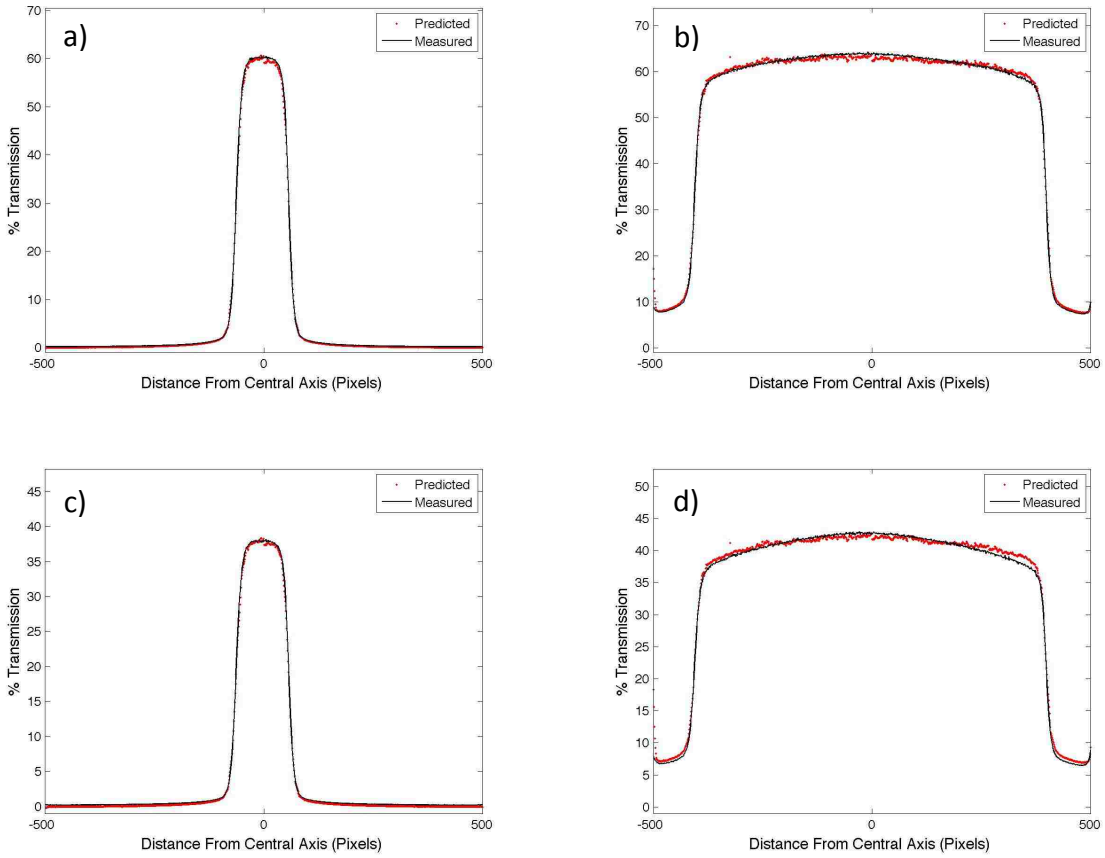

Figure 3.4. Profiles for measured (black) and predicted (red) images. a) 3x3 FS, 10 cm phantom, b) 20x20 FS, 10 cm phantom, c) 3x3 FS, 20 cm phantom, and d) 20x20 FS, 20 cm phantom

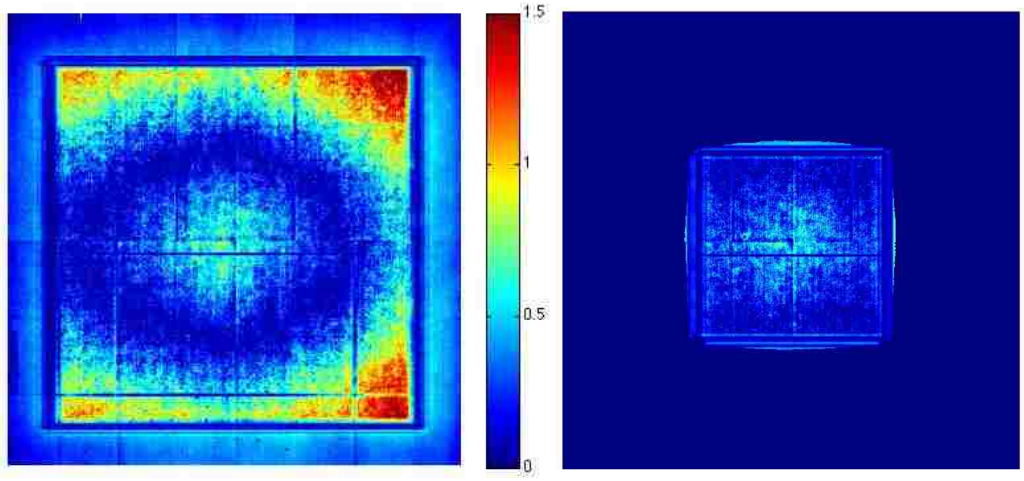

Figure 3.5. Gamma values for the 10 x 10 cm^2 (left) and 20 x 20 cm^2 (right) field sizes, 20 cm calibration phantom. Gamma values greater than one represent points that failed the gamma analysis under the 3% 3 mm criteria.

3.3 RESULTS FOR AIM 2: HOMOGENEOUS PHANTOM WITH COMPLEX GEOMETRY

The homogeneous plastic water phantom with complex geometry tested the transit dosimetry method for a more complicated geometry than the single thickness, homogeneous plastic water slabs. For the smaller field examples, only one thickness was present in the field, so the effect of the changing thickness of the phantom on these images was expected to be minimal. In the larger field sizes, the changes in phantom thickness were evident within the field. Figure 3.6 shows a measured (left) and predicted (middle) transit image for a 15 x 15 cm^2 field size, along with a display of gamma values (right).

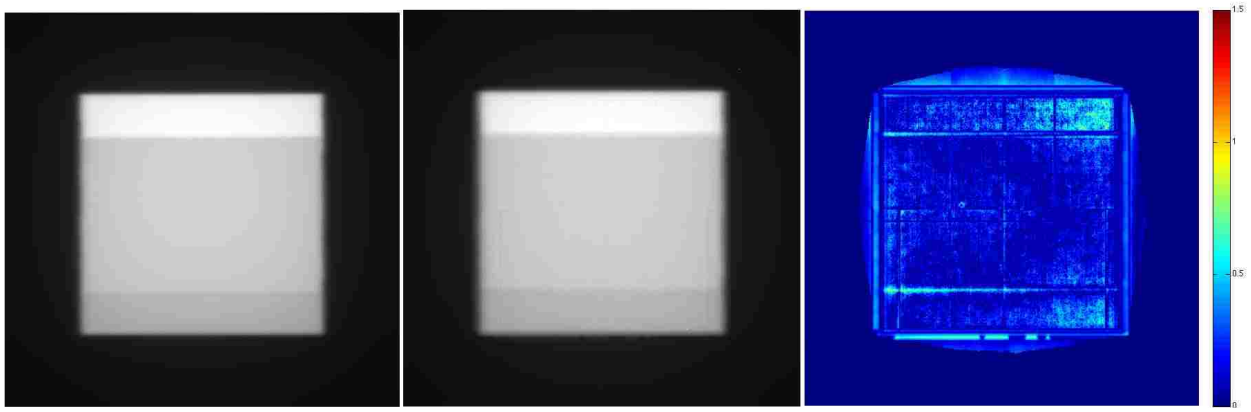

Figure 3.6. Measured (left) and predicted (center) EPID transit images, and gamma values (right) for the complex geometry homogeneous phantom and a 15 x 15 cm^2 field.

The results of the gamma analysis comparison for the homogeneous, complex geometry phantom are shown in Table 3.2. The average passing rate for this phantom was 98.9%, and passing rates ranged from 94.8% to 100.0% for the 20 x 20 cm^2 and 3 x 3 cm^2 field sizes, respectively. Changes in thickness present in the larger field size images were tracked accurately by the predicted images. The failure points that were present were once again mostly at the edges of the fields, with some failures at the points of thickness change in the phantom and at points far from the CAX at the largest field sizes (Figure 3.7).

Table 3.2. 3%/ 3 mm gamma analysis results for homogeneous, complex geometry plastic water phantom.

Field Size (cm^2)	% of Passing Points
3 x 3	100.0
5 x 5	100.0
10 x 10	100.0
15 x 15	99.8
20 x 20	94.8

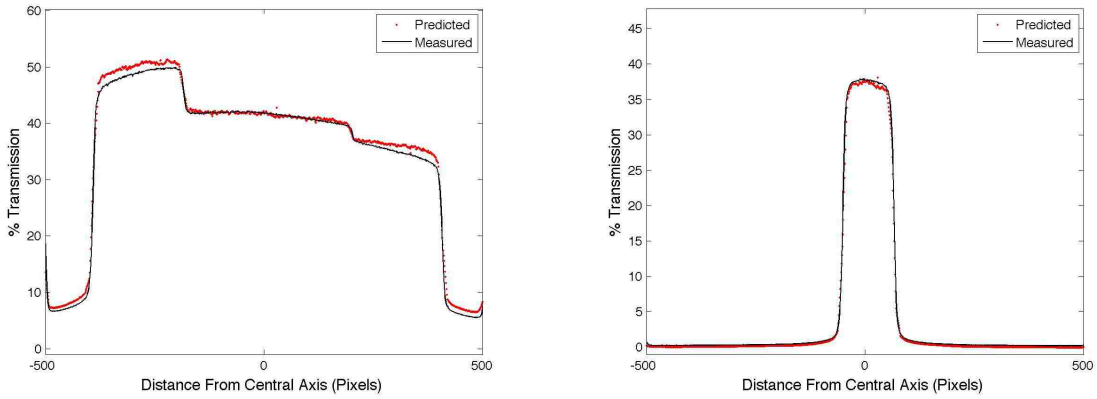

Figure 3.7. Profiles for measured (black) and predicted (red) Aim 2 phantom images. Left: 20 x 20 cm^2 . Right: 3 x 3 cm^2 field size.

3.4 RESULTS OF HETEROGENEOUS CYLINDER PHANTOM

The cylinder phantom (Figure 2.15) contained complex cylindrical geometry and the internal heterogeneities (air). In addition, the Aim 3 phantom is composed of polymethyl methacrylate (PMMA), which tested the EPID transit dosimetry method on a different material.

Figure 3.8 shows profiles and gamma results for the 5 x 5 cm^2 and 20 x 20 cm^2 fields. Table 3.3 shows the results of the gamma analysis for the cylindrical, heterogeneous phantom. The average gamma passing rate for the 3%/ 3mm analyses was 94.6%. The passing rates

ranged from 100.0% for the 5 x 5 cm^2 field to 75.7% for the 15 x 15 cm^2 field. For the 15 x 15 cm^2 field analysis, many of the points that fail are just above the criteria. A second gamma analysis was calculated for this field with 5%/ 3 mm gamma criteria (Figure 3.9). With the second analysis, the passing rate for the 15 x 15 cm^2 field increased from 75.7% to 97.9%. Section 4.5 gives an explanation for the higher failure rate of the 15 x 15 cm^2 field.

For the larger fields in the Aim 3 and Aim 4 cases, the areas where the couch was visible were eliminated from the gamma analyses. The edges of some of the larger field images contained the couch, so those portions of the images were removed prior to gamma analysis..

Table 3.3. 3%/ 3 mm gamma analysis results for heterogeneous cylinder PMMA phantom

Field Size (cm^2)	% of Passing Points
3 x 3	100.0
5 x 5	100.0
10 x 10	99.6
15 x 15	75.7
20 x 20	97.8

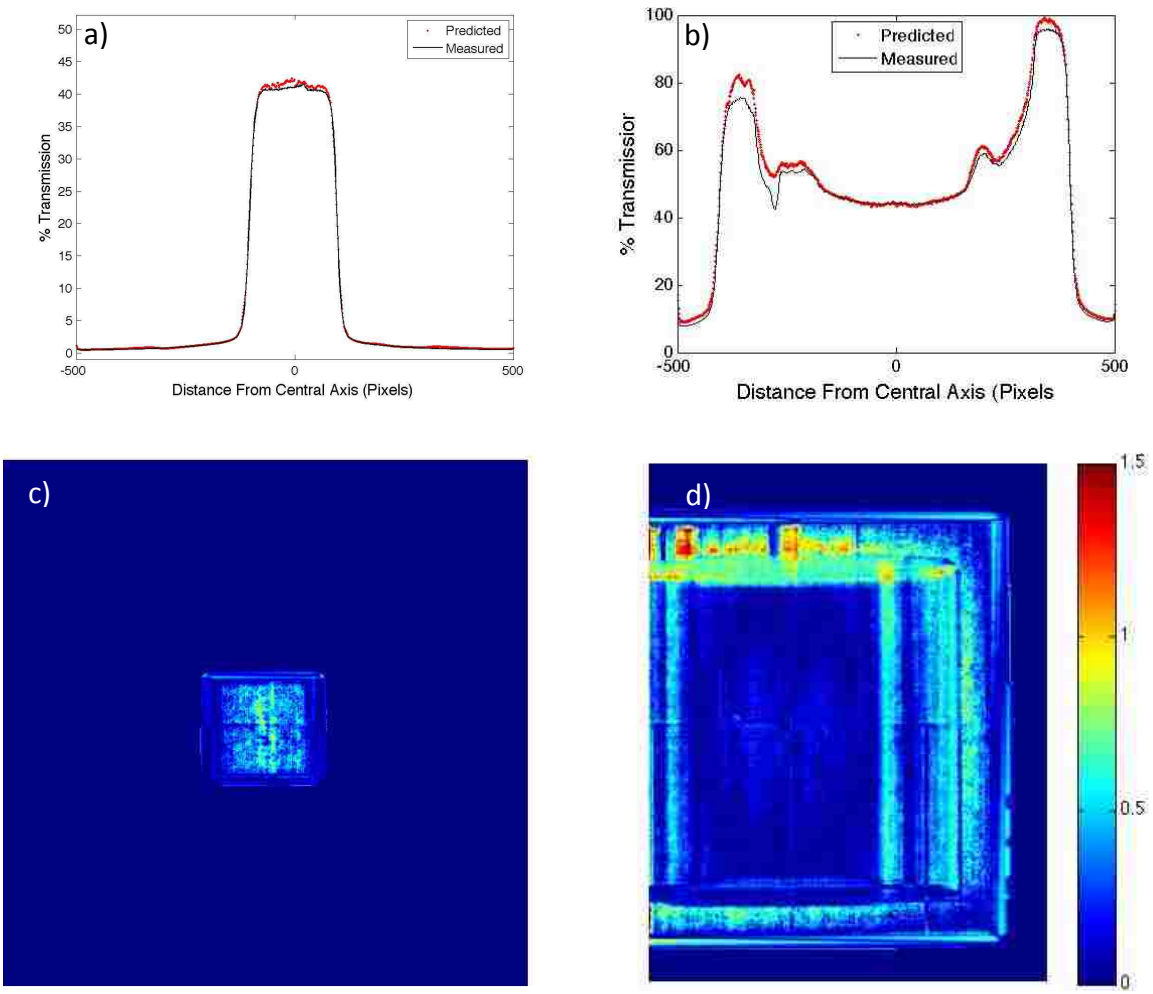

Figure 3.8. Top: Profiles for the heterogeneous cylinder phantom for the a) 5 x 5 cm^2 field and b) 20 x 20 cm^2 field. Bottom: Gamma values for the c) 5 x 5 cm^2 field and d) 20 x 20 cm^2 field. The 20 x 20 cm^2 profile and image were truncated to remove couch artifacts from the analysis (see section 2.3).

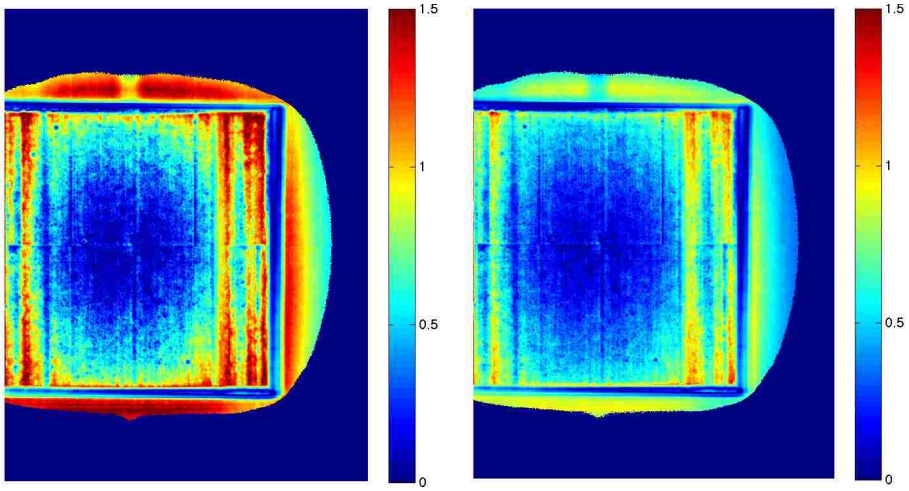

Figure 3.9. Gamma values for (left) the 3%/ 3 mm and (right) 5%/ 3 mm gamma for the 15 x 15 cm^2 field size cylinder phantom.

3.5 RESULTS OF AIM 4 PHANTOM

To test the transit dosimetry method for a clinically relevant case, an anthropomorphic head phantom was introduced for Aim 4 (Figure 3.10). The phantom contains geometry and compositional materials comparable to a human head. The geometry and heterogeneities in this phantom were far more irregular than in the previous phantoms. Figure 3.11 compares profiles for

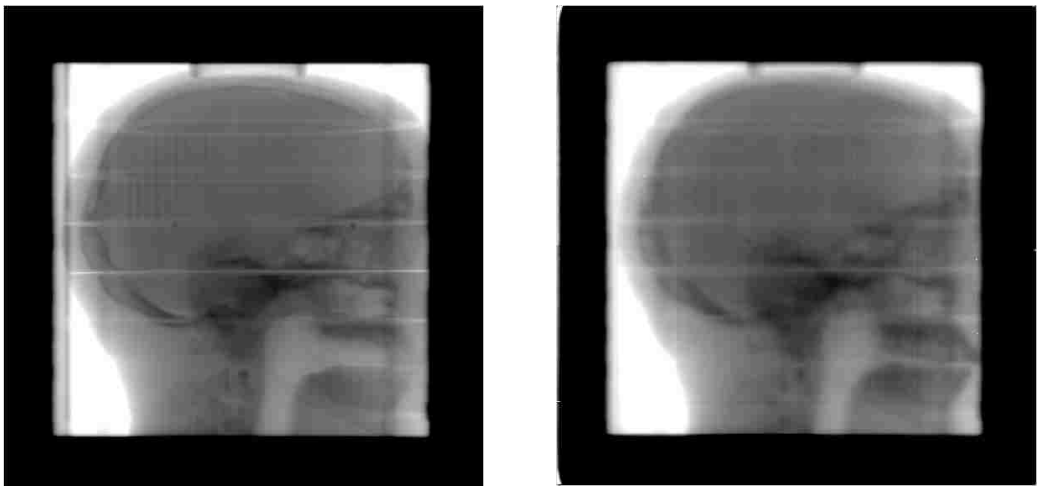

Figure 3.10. Measured (left) and predicted (right) transit images for an anthropomorphic head phantom. Field size is 20 x 20 cm^2.

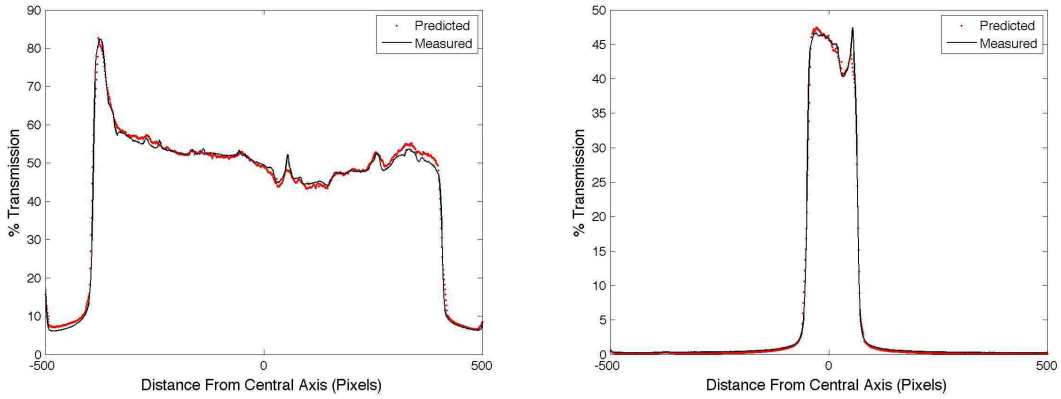

Figure 3.11. Profiles for measured (black) and predicted (red) anthropomorphic phantom images. Left: 20 x 20 cm^2. Right 3 x 3 cm^2 field size.

predicted and measured transit images for two field sizes.

Due to the complex attributes of the anthropomorphic phantom, a 5%/ 3 mm gamma index was used for analysis (Figure 3.12). Table 3.4 shows the results of the gamma analysis. The average passing rate for points of the head phantom images was 98.3%, and ranged from 97.4% to 99.2% for the 3 x 3 cm^2 and 5 x 5 cm^2 field sizes, respectively. The irregular geometry and heterogeneities of the phantom demonstrated the capability of the EPID transit dosimetry method to acceptably predict EPID transit treatment images for a patient-like scenario, with ≥95% gamma point passing rates for all field sizes. The one feature of the anthropomorphic head that showed a high number of point failures was the teeth (discussed in section 4.6).

To further assess the capability of this situation, a more stringent 3%/ 3 mm analysis was performed for the anthropomorphic head phantom data. Figure 3.13 and Table 3.5 show the gamma analysis results for the 3%/ 3 mm comparison. The average passing rate for points in the head phantom images was 96.6%, and ranged from 94.8 to 98.1% for the 15 x 15 cm^2 and 5 x 5 cm^2 field sizes, respectively. The vast majority of the features of the head passed the more strict 3% criteria, with the only major exception again being the teeth.

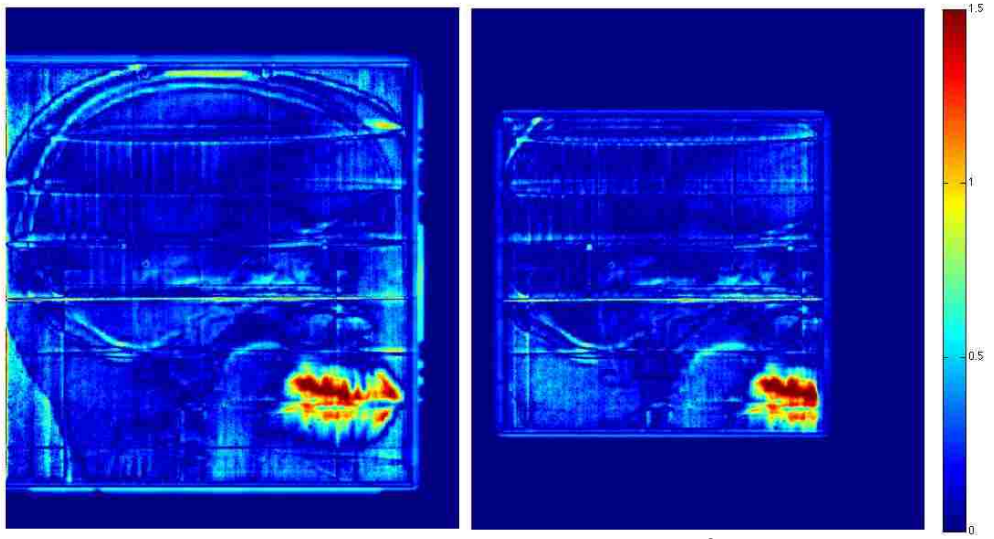

Figure 3.12. 5%/ 3 mm gamma values for (left) 20 x 20 cm^2 and (right) 15 x 15 cm^2 for the anthropomorphic head phantom.

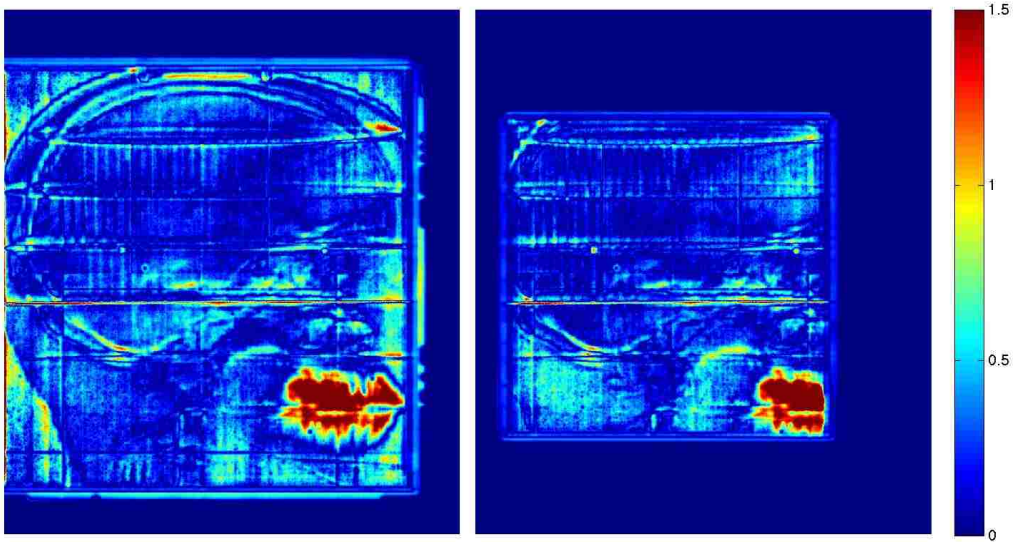

Figure 3.13. 3%/ 3 mm gamma values for (left) 20 x 20 cm^2 and (right) 15 x 15 cm^2 for the anthropomorphic head phantom.

Table 3.4. 5% / 3 mm gamma analysis results for anthropomorphic head phantom.

Field Size (cm^2)	% of Passing Points
3 x 3	97.4
5 x 5	99.2
10 x 10	98.6
15 x 15	98.2
20 x 20	98.6

Table 3.5. 3% / 3 mm gamma analysis results for anthropomorphic head phantom.

Field Size (cm^2)	% of Passing Points
3 x 3	96.6
5 x 5	98.1
10 x 10	96.7
15 x 15	94.8
20 x 20	97.0

CHAPTER 4: DISCUSSION AND CONCLUSIONS

4.1 RESULTS SUMMARY

This work describes a method of transit dosimetry that is novel in its use of a "through-air" image to calculate the predicted EPID transit image. Current methods derive dose information from EPID intensity patterns by transforming the images measured by the EPID into dose within the patient or at the plane of the EPID (Renner 2007; van Elmpt 2008). These approaches require that various dose response dependencies of the EPID – energy, dose rate, beam hardening, field size, scatter, and nonuniformity – be carefully characterized and accounted for in order to convert the EPID pixel intensities to dose. In contrast, the proposed method eliminates this conversion by predicting the transmitted intensity. To assess the feasibility of the proposed method, evaluation proceeded from simple homogeneous phantoms, through more complex setups, to a patient-like scenario. Predicting dose in the patient in two or even three dimensions was not attempted here, but could be a future extension of this work. The motivation for this research was to find a straightforward method for EPID transit dosimetry that required a minimum of time and effort, and was general enough to be implemented in other clinics with any commercial EPID.

In the proposed method, through-air portal images were convolved with field specific pencil kernels to produce predicted transit images. The kernels were selected based upon the radiological pathlength of ray traces from the beam source, through the patient, and terminating at the detector elements. Gamma analysis was used to compare predicted images with measured transit images.

The hypothesis tested in this research effort stated that a through-air approach to transit dosimetry using the EPID could be devised that would predict EPID transit images to within specified criteria* compared with measured transit images for phantoms of increasing complexity.

*homogeneous phantom: gamma [3%/ 3 mm; 95% passing rate]

*cylindrical heterogeneous phantom: gamma [3%/ 3 mm; 95% passing rate]

*anthropomorphic phantom: gamma [5%/ 3 mm; 95% passing rate]

This hypothesis was supported by the initial feasibility study presented in this thesis. The average passing rate for the homogeneous plastic slab phantoms was 99% for all field sizes and the average passing rate for the heterogeneous cylinder phantom was 95% for all field sizes. The results from the 5%/ 3 mm gamma analysis for the anthropomorphic head returned an average passing rate of 98% for all field sizes. An additional gamma analysis using 3%/ 3 mm criteria showed an average passing rate of 97% for all field sizes, indicating the method successfully predicted the transit portal images for the anthropomorphic phantom even under the more strict criteria. All tests met or exceeded the conditions of the hypothesis.

The gamma results for all phantoms and field sizes are summarized in Table 4.1. In general, the passing rates for all field sizes and phantoms were satisfactory. Failure points that are present are generally found in the out of field areas just above the 10% maximum dose threshold. A complete set of gamma and profile results for all field sizes and phantoms is provided in the appendix of this thesis.

Table 4.1. Percentage of points passing for gamma analysis results for all fields and phantoms. All criteria are 3%/ 3 mm unless otherwise noted.

	Field Size (cm^2)					
Phantom	3 x 3	5 x 5	10 x 10	15 x 15	20 x 20	Average
Plastic Water, 5cm	100.0%	100.0%	100.0%	100.0%	100.0%	100.0%
Plastic Water, 10cm	100.0%	100.0%	100.0%	100.0%	100.0%	100.0%
Plastic Water, 15cm	100.0%	100.0%	100.0%	100.0%	98.4%	99.7%
Plastic Water, 20cm	100.0%	100.0%	100.0%	100.0%	95.7%	99.1%
Plastic Water, 25cm	100.0%	100.0%	100.0%	99.1%	94.2%	98.7%
Complex Geom. Plastic Water	100.0%	100.0%	100.0%	99.8%	94.8%	98.9%
PMMA Cylinder	100.0%	100.0%	99.6%	75.7%	97.8%	94.6%
Anthro Head (5%/ 3 mm)	97.4%	98.8%	98.6%	98.2%	98.6%	98.3%
Anthro Head (3%/ 3 mm)	96.6%	98.1%	96.7%	94.8%	97.0%	96.6%

4.2 LIMITATIONS AND CONSEQUENCES OF THE EPID TRANSIT DOSIMETRY MODEL

The use of pencil beams with assumed constant fluence, energy spectra, and angle of incidence means that any prediction based on the pencil kernels had limitations. In the clinical situation, the divergent beam produced by the linac and incident on the patient and EPID varies in these quantities as a function of off axis distance.

The beam's average energy drops as off axis distance increases, with changes in average energy of up to 25% for a position 20 cm off axis compared to the central axis position (Sheikh-Bagheri Rogers 2002). Due to the EPID's nonuniform energy response (Figure 4.1), an assumption of uniform energy spectrum across the profile of the incident beam necessarily introduced spatially variant errors into the predicted transit image. The energy spectrum across the profile also changes with the thickness of object traversed by the radiation due to beam hardening. The response of the EPID to the open beam was captured in this transit dosimetry method by the through-air image, but the kernels used in the convolution of the through-air image assumed constant energy spectrum, neglecting changes in spectrum across the profile as a function of off-axis position and object thickness.

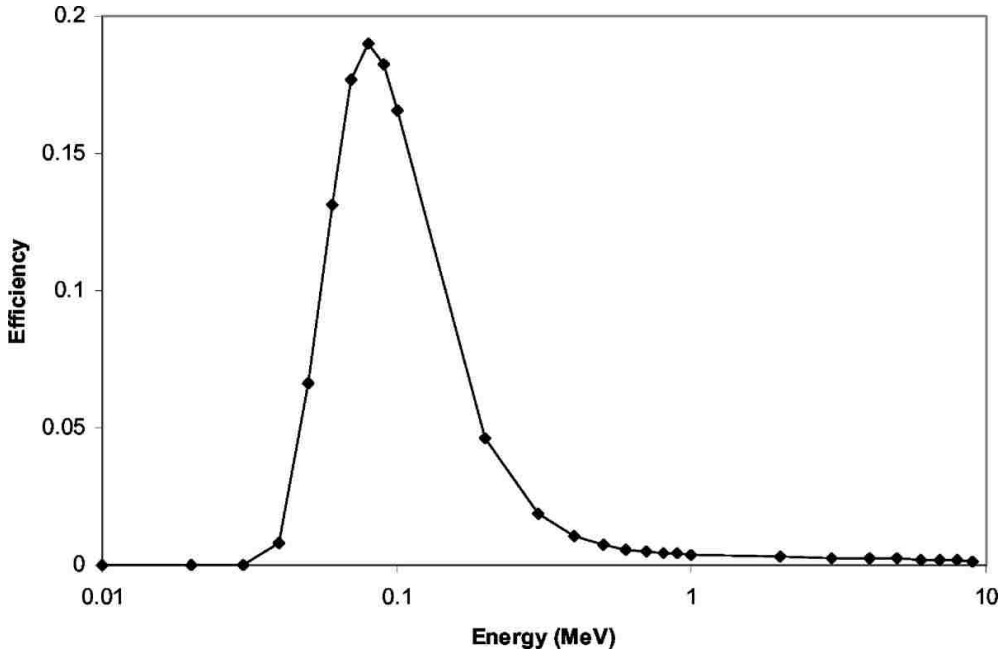

Figure 4.1. Efficiency as a function of energy for the Elekta EPID as calculated by Parent *et al*. for 0.002 x 0.002 cm^2 monoenergetic photon beams scored as dose deposited in the phosphor layer. (Parent 2007)

In addition to the spectral simplifications assumed in the Monte Carlo model, there were some geometric inconsistencies. First, the kernels assumed only parallel incidence. The true geometry of the divergent beam presents a different geometry, as studied by Chytyk *et al.* Their group compared the results of a parallel pencil beam kernel convolution calculation with results of a superposition calculation that took into account the actual incidence angles differences in the divergent beam geometry (Chytyk McCurdy 2006). They found maximum errors of 1% for monoenergetic beams of 0.1, 2, and 6 MeV using χ-comparison testing. Their study, however, used uniform fluence, and modeled the EPID with 3 cm of additional water buildup, which could affect the magnitude of errors. Other attempts to quantify the magnitude of error for using a parallel kernel approximation have been made (Sharpe Battista 1993; Helen Liu 1997) showing both similar and larger (in the case of Sharpe *et al.*) errors, but these studies

were not specific to portal dose and so do not account for the effects of the extended geometry and EPID construction materials involved.

Aside from the errors introduced by approximations of the pencil beam geometry, additional errors were introduced by the kernel simulation process. First, the change in air gap due to beam divergence was ignored in the Monte Carlo simulations. For each simulation through water, the pencil beam was modeled as a parallel beam through the medium with the midline depth of the water placed at 100 cm and a constant air gap behind the water (Figure 4.2). The ray trace algorithm then selected for the appropriate radiological thickness, which included an increased thickness of water traversed due to divergence. However, there is also a small increase in air gap that accompanies the increase in pathlength as the angle of divergence increases. Renner described the effects of air gap on EPID dosimetry and found that for large air gaps (>35 cm) the error resulting from the change in air gap was less than 2% (Math Resolutions ; Renner 2013). Renner had, however, corrected for the inverse square effect of increased air gap, which is not accounted for in the method of this study. The effect of not having an inverse square correction would be <0.8% error.

Another assumption made in the kernel simulation process related to air gap involved the isocentric placement (midline depth of water at 100 cm) of the water in the simulation geometry. This geometry was approximately accurate for isocentric treatments where isocenter is near the midline depth of the patient. While non-isocentric setups will be commonly encountered by EPID transit dosimetry, dealing with these effects is outside of the scope of this study. In addition, from Renner's work, errors introduced from air gap changes

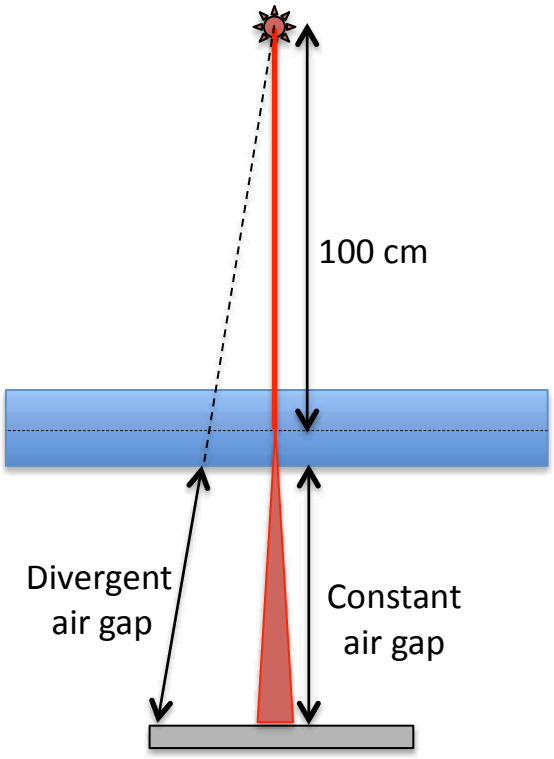

Figure 4.2. Diagram of kernel simulation geometry with constant air gap assumption illustrated. The simulation modeled a constant air gap and did not account for the increased air gap associated with the angle of incidence in a divergent beam.

are expected to be <2%. The errors related to treating a tumor not in the center of the field could also introduce errors and was studied by Cilla *et al.* (Cilla 2013), although the implications of this kind of treatment on prediction accuracy was outside of the scope of this study.

A further physical phenomenon not modeled in the pencil beam simulations was the spread (scatter and reflection) of optical photons in the phosphor layer of the EPID. As discussed in section 2.2, optical spread has an impact on field size dependence and also contributes to the EPID's off axis response (see section 4.4). The effect that optical scatter has on the EPID's response was studied by multiple groups with both measurement (Gustafsson 2009) and Monte Carlo simulation (Blake 2013). For the proposed method, the optical photon transport of the open beam was accounted for in the through-air image, but any changes to

that transport due to the attenuating medium were not modeled in the Monte Carlo simulations.

To test the feasibility of this approach, transit images were predicted for square, isocentrically delivered fields with a fixed source-to-detector (SDD) distance. The beams were delivered through various phantoms of increasing complexity. Some of the fields encompassed part of the CT and treatment couches. Errors in predicted images due to attenuation in the couches were excluded from this research. A number of other parameters, including gantry angle, long-term stability, and image lag and ghosting were not examined here. Other authors reported on the effects these parameters (Greer 2011; Berry 2012). Due to these constraints, the results were therefore limited in their reach. However, the purpose of this study was to assess the feasibility of the EPID transit dosimetry method to determine if it warranted further investment of time, energy, and money.

4.3 AIM 1 DISCUSSION

The radiological pathlength calculations for the test case of the 5 cm thick block of plastic water gave a quantitative indication that the algorithm provided satisfactory results. Both the manually calculated pathlengths, and the pathlength estimated from the manufacturer's density, were within the range of uncertainty due to CT number measurement of the Matlab calculated radiological pathlength. In addition, the geometrical increase in pathlength due to divergence at the edge of the detector was consistent with the increase seen in the Matlab algorithm calculation.

4.4 AIM 2 DISCUSSION

Many of the failure points in gamma analyses were found for points near the edges of large fields. These failures likely resulted from the spectral changes in the divergent beam measured by the EPID that were not accounted for in the pencil beam Monte Carlo kernel calculations (Swindell Evans 1996).

In general, there was a systematic overestimate in the predicted transit image compared to the transit image at the edges of large fields. These findings were consistent with those of other authors (McCurdy 2001; Berry 2012; Blake 2013; Renner 2013). Renner cited a decrease in off axis patient scatter as a reason for the overestimate in the prediction, with the effect being most pronounced for large field sizes and phantom thicknesses (Renner 2013). Swindell *et al* showed that for a 14.1 x 14.1 cm^2 beam of uniform incident spectrum (as a function of off axis distance), the scatter generated from the phantom for a 20 cm thick slab of water changed from 7% at the central axis to 4% at a point 20 cm off axis when measured at 160 cm SDD (Swindell Evans 1996). The pencil kernel approach did not account for this change in patient scatter as a function of off axis distance. Because the EPID over responds to scattered radiation, the measured transit image showed smaller signals at greater distances off axis compared to the predicted transit image.

Other authors have shown that "glare" or optical photon scattering played a role in overestimation of the predicted transit image near the field edges (McCurdy 2001; Berry 2012; Blake 2013). McCurdy *et al* used an empirical glare kernel to correct for the overestimate, while Berry suggested that the influence of optical photons on the overestimate in prediction at field edges might be related to the loss of lateral equilibrium near the edges of the detector, which was not modeled in the pencil beam approach.

Additionally, application of the kernels as parallel pencil beams assumed a perpendicular incidence. Small errors (~1%) associated with this assumption would be most evident at large distances from the CAX in large fields due to the increasing angle of incidence relative to perpendicular incidence (Chytyk McCurdy 2006). The savings in computational time due to the use of the pencil beams over divergent beam simulations, however, likely outweighs the losses in accuracy, because the magnitude of the errors was minimal. Furthermore, IMRT treatments typically use small field sizes (Chytyk McCurdy 2006).

There was good agreement for the plastic water phantom with multiple thicknesses. Failures that did exist mirrored those that were found for the simple flat plastic water phantoms, with some prediction overestimates at the corners of large fields. The same arguments made above should also apply to the explanation for these overestimates.

4.5 AIM 3 DISCUSSION

In general there was a persistent, albeit subtle, overestimate in the prediction of the cylinder phantom. Even with the addition of the more points to the CT-to-density conversion table, there remained an overestimate of up to 2%. The overestimate may simply be due to variability in the phantom's manufacturing process or small variabilities in the day-to-day setup and performance of the CT scanner and linear accelerator and setup. Another possible factor for the change in response is the age of the phantom. This phantom was an older phantom with some substantial yellowing. PMMA is known to suffer from polymer disruption from exposure to radiation (Schmalz 1996; Lee 1999), which could have some effect on its attenuation and scattering characteristics. A future direction for the research could involve efforts to further elucidate the causes of this inaccuracy.

4.6 AIM 4 DISCUSSION

While nearly all features of the head anatomy were predicted accurately, substantial gamma failures between the predicted and measured transit images were noted in the area of the teeth (Figure 3.12). The teeth of the anthropomorphic phantom are made of a synthetic barium-based compound with a density of about 3.0 g/cm^3. The teeth for the anthropomorphic phantom caused severe streaking artifacts in the CT images generated (Figure 4.3). One source for the streaking may be the fact that the high CT numbers for the teeth were near the upper limit of the CT scanner.

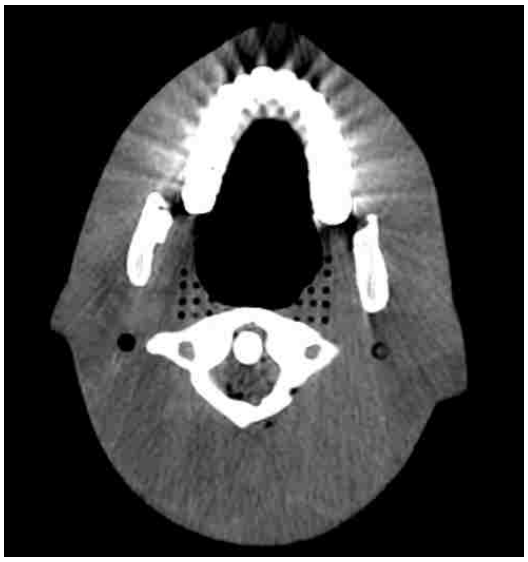

Figure 4.3. CT image of the anthropomorphic head phantom with severe streaking artifacts in the teeth region.

4.7 FUTURE WORK

Future directions for this work vary in scope. The method's robustness in predicting transit images for other field orientations and shapes, as well as for alternate linear accelerators needs to be analyzed. For example, the energy spectrum of the linear accelerator and EPID construction may vary slightly from one model or manufacturer to the next. Testing

the sensitivity of the dosimetry method to these variations will help to determine how generally the method could be applied.

The method will need to be modified to incorporate the attenuation of the CT and treatment couches. It may be possible, for example to replace the CT couch data with treatment couch data when calculating the radiological pathlength. Mitigating these discrepancies will provide a more robust method, capable of being applied to a wider range of field sizes and orientations.

The effects of image lag and ghosting, gantry angle dependency, and long-term stability of the EPID on the accuracy of the transit dosimetry method may need to be addressed. Authors have studied these effects (van Elmpt 2008; Greer 2011), but mitigation of the resulting errors was expected due to the introduction of the through-air EPID image from which the predicted transit images were generated. Nevertheless, incorporating these effects may further improve the predicted transit images.

Expanding the method for prediction of complex IMRT fields will be necessary. This feasibility study focused on single segment, square fields for a number of different phantom types. To utilize the EPID transit dosimetry method for IMRT, the method must be tested for complex IMRT fields with multiple segments and irregular multileaf collimator-defined field shapes. Concerns arising from the addition of such fields include the weighting of individual segments within a single field, differences in transmission of the MLC leaves and primary linac collimators, and accuracy of the method for handling heavily modulated fields (Cilla 2013). Utilizing the transit dosimetry method for arc therapy could also be investigated, which would require analysis of the method for predicting images of the transit beam during gantry rotation.

REFERENCES

Antonuk, L. E. (2002). "Electronic portal imaging devices: a review and historical perspective of contemporary technologies and research." Phys Med Biol **47**(6): R31.

Bedford, J. L., Hanson, I. M. and Hansen, V. N. (2014). "Portal dosimetry for VMAT using integrated images obtained during treatment." Med Phys **41**(2): 021725.

Berry, S. L. (2012). Transit Dosimetry for Patient Treatment Verification with an Electronic Portal Imaging Device, COLUMBIA UNIVERSITY.

Berry, S. L., Sheu, R. D., Polvorosa, C. S. and Wuu, C. S. (2012). "Implementation of EPID transit dosimetry based on a through-air dosimetry algorithm." Med Phys **39**(1): 87-98.

Blake, S. J., Vial, P., Holloway, L., Greer, P. B., McNamara, A. L. and Kuncic, Z. (2013). "Characterization of optical transport effects on EPID dosimetry using Geant4." Med Phys **40**(4): 041708.

Bogaerts, R., Van Esch, A., Reymen, R. and Huyskens, D. (2000). "A method to estimate the transit dose on the beam axis for verification of dose delivery with portal images." Radiotherapy and Oncology **54**(1): 39-46.

Both, S., Alecu, J. M., Stan, A. R., Alecu, M., Ciura, A., Hansen, J. M. and Alecu, R. (2007). "A study to establish reasonable action limits for patient specific IMRT QA." Journal of Applied Clinical Medical Physics **8**(2).

Chaumet, F. and Bleuse, O. (2013). "Implementation of in vivo dosimetry with epigray." Physica Medica **29**: e32.

Childress, N. L., Bloch, C., White, R. A., Salehpour, M. and Rosen, I. I. (2005). "Detection of IMRT delivery errors using a quantitative 2D dosimetric verification system." Med Phys **32**: 153.

Chytyk, K. and McCurdy, B. M. C. (2006). "Investigation of tilted dose kernels for portal dose prediction in a-Si electronic portal imagers." Med Phys **33**(9): 3333-3339.

Cilla, S., Azario, L., Greco, F., Fidanzio, A., Porcelli, A., Grusio, M., Macchia, G., Morganti, A., Meluccio, D. and Piermattei, A. (2013). "An in-vivo dosimetry procedure for Elekta step and shoot IMRT." Physica Medica.

Dong, L., Antolak, J., Salehpour, M., Forster, K., O'Neill, L., Kendall, R. and Rosen, I. (2003). "Patient-specific point dose measurement for IMRT monitor unit verification." International Journal of Radiation Oncology* Biology* Physics **56**(3): 867-877.

Dupuis, P., Ginestet, C., Rousseau, V. and Kafrouni, H. (2011). "In Vivo Dosimetry using EPIgray® software based on transit dosimetry for Elekta IviewGT® electronic portal imaging." Physica Medica **27**: S23-S24.

Dyk, J. V., Barnett, R., Cygler, J. and Shragge, P. (1993). "Commissioning and quality assurance of treatment planning computers." International Journal of Radiation Oncology* Biology* Physics **26**(2): 261-273.

Essers, M. and Mijnheer, B. (1999). "*In vivo* dosimetry during external photon beam radiotherapy." International Journal of Radiation Oncology* Biology* Physics **43**(2): 245-259.

Fafi, S., Largeron, G., Nguyen, D., Josserand Pietri, F., Da Eira, E. and Khodri, M. (2013). "Clinical experience of in vivo dosimetry 3D (dosimetry check) by portal imaging for treatment of breast cancer." Physica Medica **29**: e32-e33.

Fraass, B., Doppke, K., Hunt, M., Kutcher, G., Starkschall, G., Stern, R. and Van Dyke, J. (1998). "American Association of Physicists in Medicine Radiation Therapy Committee Task Group 53: quality assurance for clinical radiotherapy treatment planning." Med Phys **25**: 1773.

Grattan, M. W. and McGarry, C. K. (2010). "Mechanical characterization of the Varian Exact-arm and R-arm support systems for eight aS500 electronic portal imaging devices." Med Phys **37**(4): 1707-1713.

Greer, P. B. (2005). "Correction of pixel sensitivity variation and off-axis response for amorphous silicon EPID dosimetry." Med Phys **32**: 3558.

Greer, P. B. and Popescu, C. C. (2003). "Dosimetric properties of an amorphous silicon electronic portal imaging device for verification of dynamic intensity modulated radiation therapy." Med Phys **30**(7): 1618-1627.

Greer, P. B. and Vial, P. (2011). Epid Dosimetry. AIP Conference Proceedings.

Grubbe, E. H. (1902). "X-rays in the treatment of cancer and other malignant diseases." Medical Record **62**: 692-695.

Gustafsson, H., Vial, P., Kuncic, Z., Baldock, C. and Greer, P. B. (2009). "EPID dosimetry: Effect of different layers of materials on absorbed dose response." Med Phys **36**(12): 5665-5674.

Hall, E., J., Giaccia, A., J. (2006). Radiobiology for the Radiobiologist. Philidelphia, PA, Lippincott Williams & Wilkins.

Halperin, E. C., Brady, L. W., Wazer, D. E. and Perez, C. A. (2013). Principles and practice of radiation oncology, Lippincott Williams & Wilkins.

Hansen, V., Evans, P. and Swindell, W. (1996). "The application of transit dosimetry to precision radiotherapy." Med Phys **23**: 713.

Helen Liu, H., Mackie, T. R. and McCullough, E. C. (1997). "Correcting kernel tilting and hardening in convolution/superposition dose calculations for clinical divergent and polychromatic photon beams." Med Phys **24**(11): 1729-1741.

Herman, M. G., Balter, J. M., Jaffray, D. A., McGee, K. P., Munro, P., Shalev, S., Van Herk, M. and Wong, J. W. (2001). "Clinical use of electronic portal imaging: Report of AAPM Radiation Therapy Committee Task Group 58." Med Phys **28**(5): 712-737.

Jarry, G. and Verhaegen, F. (2007). "Patient-specific dosimetry of conventional and intensity modulated radiation therapy using a novel full Monte Carlo phase space reconstruction method from electronic portal images." Phys Med Biol **52**(8): 2277.

Jemal, A., Siegel, R., Xu, J. and Ward, E. (2010). "Cancer statistics, 2010." CA Cancer J Clin **60**(5): 277-300.

Jornet, N., Carrasco, P., Jurado, D., Ruiz, A., Eudaldo, T. and Ribas, M. (2004). "Comparison study of MOSFET detectors and diodes for entrance in vivo dosimetry in 18 MV x-ray beams." Med Phys **31**: 2534.

Kirkby, C. and Sloboda, R. (2005). "Consequences of the spectral response of an a-Si EPID and implications for dosimetric calibration." Med Phys **32**(8): 2649-2658.

Klein, E. E., Hanley, J., Bayouth, J., Yin, F.-F., Simon, W., Dresser, S., Serago, C., Aguirre, F., Ma, L. and Arjomandy, B. (2009). "Task Group 142 report: quality assurance of medical accelerators." Med Phys **36**: 4197.

Kutcher, G. J., Coia, L., Gillin, M., Hanson, W. F., Leibel, S., Morton, R. J., Palta, J. R., Purdy, J. A., Reinstein, L. E. and Svensson, G. K. (1994). "Comprehensive QA for radiation oncology: Report of AAPM radiation therapy committee task group 40." Med Phys **21**: 581.

Lee, E., Rao, G. and Mansur, L. (1999). "LET effect on cross-linking and scission mechanisms of PMMA during irradiation." Radiation physics and chemistry **55**(3): 293-305.

Liebich, J., Licher, J., Scherf, C., Kara, E., Koch, N., Rödel, C. and Ramm, U. (2011). "Simple Proposal for Dosimetry with an Elekta iViewGT TM Electronic Portal Imaging Device (EPID) Using Commercial Software Modules." Strahlentherapie und Onkologie **187**(5): 316-321.

Litzenberg, D. W., Balter, J. M., Hadley, S. W., Sandler, H. M., Willoughby, T. R., Kupelian, P. A. and Levine, L. (2006). "Influence of intrafraction motion on margins for prostate radiotherapy." International Journal of Radiation Oncology* Biology* Physics **65**(2): 548-553.

LoSasso, T., Chui, C.-S. and Ling, C. C. (2001). "Comprehensive quality assurance for the delivery of intensity modulated radiotherapy with a multileaf collimator used in the dynamic mode." Med Phys **28**: 2209.

Louwe, R., Damen, E., van Herk, M., Minken, A., Törzsök, O. and Mijnheer, B. (2003). "Three-dimensional dose reconstruction of breast cancer treatment using portal imaging." Med Phys **30**: 2376.

Louwe, R. J., McDermott, L. N., Sonke, J.-J., Tielenburg, R., Wendling, M., Van Herk, M. and Mijnheer, B. J. (2004). "The long-term stability of amorphous silicon flat panel imaging devices for dosimetry purposes." Med Phys **31**: 2989.

Low, D. A., Harms, W. B., Mutic, S. and Purdy, J. A. (1998). "A technique for the quantitative evaluation of dose distributions." Med Phys **25**(5): 656-661.

Math Resolutions, L. "Dosimetry Check." US Patent 6,853,702 and **8**: 8,605,857.

McCurdy, B. M., Luchka, K. and Pistorius, S. (2001). "Dosimetric investigation and portal dose image prediction using an amorphous silicon electronic portal imaging device." Med Phys **28**(6): 911-924.

McDermott, L., Wendling, M., Van Asselen, B., Stroom, J., Sonke, J.-J., Van Herk, M. and Mijnheer, B. (2006). "Clinical experience with EPID dosimetry for prostate IMRT pre-treatment dose verification." Med Phys **33**: 3921.

McEwen, M., Williams, A. and DuSautoy, A. (2001). "Determination of absorbed dose calibration factors for therapy level electron beam ionization chambers." Phys Med Biol **46**(3): 741.

McNutt, T. R., Mackie, T. R., Reckwerdt, P. and Paliwal, B. R. (1996). "Modeling dose distributions from portal dose images using the convolution/superposition method." Med Phys **23**: 1381.

Mohammadi, M., Bezak, E. and Reich, P. (2006). "The use of extended dose range film for dosimetric calibration of a scanning liquid-filled ionization chamber electronic portal imaging device." Journal of applied clinical medical physics/American College of Medical Physics **8**(1): 69.

Nijsten, S., Van Elmpt, W., Jacobs, M., Mijnheer, B., Dekker, A., Lambin, P. and Minken, A. (2007). "A global calibration model for a‐Si EPIDs used for transit dosimetry." Med Phys **34**: 3872.

Nijsten, S. M., Mijnheer, B. J., Dekker, A. L., Lambin, P. and Minken, A. W. (2007). "Routine individualised patient dosimetry using electronic portal imaging devices." Radiotherapy and Oncology **83**(1): 65-75.

Parent, L., Fielding, A., Dance, D., Seco, J. and Evans, P. (2007). "Amorphous silicon EPID calibration for dosimetric applications: comparison of a method based on Monte Carlo prediction of response with existing techniques." Phys Med Biol **52**(12): 3351.

Parent, L., Seco, J., Evans, P. M., Fielding, A. and Dance, D. R. (2006). "Monte Carlo modelling of a-Si EPID response: the effect of spectral variations with field size and position." Med Phys **33**(12): 4527-4540.

Pasma, K., Kroonwijk, M., De Boer, J., Visser, A. and Heijmen, B. (1998). "Accurate portal dose measurement with a fluoroscopic electronic portal imaging device (EPID) for open and wedged beams and dynamic multileaf collimation." Phys Med Biol **43**(8): 2047.

Pasma, K. L., Kroonwijk, M., Quint, S., Visser, A. G. and Heijmen, B. J. (1999). "Transit dosimetry with an electronic portal imaging device (EPID) for 115 prostate cancer patients." International Journal of Radiation Oncology* Biology* Physics **45**(5): 1297-1303.

Ramsey, C., Dube, S. and Hendee, W. R. (2003). "It is necessary to validate each individual IMRT treatment plan before delivery." Med Phys **30**: 2271.

Renner, W. D. (2007). "3D dose reconstruction to insure correct external beam treatment of patients." Med Dosim **32**(3): 157-165.

Renner, W. D. (2013). Method and system to reconstruct treatment dose to a patient from integrated exit-transit images of radiation fields taken during treatment, Google Patents.

Renner, W. D., Norton, K. and Holmes, T. (2005). "A method for deconvolution of integrated electronic portal images to obtain incident fluence for dose reconstruction." Journal of Applied Clinical Medical Physics **6**(4).

Renner, W. D., Norton, K. J. and Holmes, T. W. (2005). "A method for deconvolution of integrated electronic portal images to obtain fluence for dose reconstruction." Journal of Applied Clinical Medical Physics **6**(4).

Renner, W. D., Sarfaraz, M., Earl, M. A. and Cedric, X. Y. (2003). "A dose delivery verification method for conventional and intensity-modulated radiation therapy using measured field fluence distributions." Med Phys **30**: 2996.

Schmalz, O., Hess, M. and Kosfeld, R. (1996). "Structural changes in poly (methyl methacrylate) during deep‐etch X‐ray synchrotron radiation lithography. Part II: Radiation effects on PMMA." Die Angewandte Makromolekulare Chemie **239**(1): 79-91.

Sharpe, M. and Battista, J. (1993). "Dose calculations using convolution and superposition principles: The orientation of dose spread kernels in divergent x‐ray beams." Med Phys **20**(6): 1685-1694.

Sheikh-Bagheri, D. and Rogers, D. (2002). "Monte Carlo calculation of nine megavoltage photon beam spectra using the BEAM code." Med Phys **29**(3): 391-402.

Siddon, R. L. (1985). "Fast calculation of the exact radiological path for a three-dimensional CT array." Med Phys **12**(2): 252-255.

Siegel, R., Ma, J., Zou, Z. and Jemal, A. (2014) "Cancer statistics, 2014." CA Cancer J Clin.

SROA (2010). Physician Characteristics and Distribution in the U.S., 2010 Edition. SROA Benchmarking Survey. I. M. I. Division.

Swindell, W. and Evans, P. M. (1996). "Scattered radiation in portal images: a Monte Carlo simulation and a simple physical model." Med Phys **23**(1): 63-73.

van Elmpt, W., McDermott, L., Nijsten, S., Wendling, M., Lambin, P. and Mijnheer, B. (2008). "A literature review of electronic portal imaging for radiotherapy dosimetry." Radiotherapy and Oncology **88**(3): 289-309.

van Elmpt, W., McDermott, L., Nijsten, S., Wendling, M., Lambin, P. and Mijnheer, B. (2008). "A literature review of electronic portal imaging for radiotherapy dosimetry." Radiother Oncol **88**(3): 289-309.

van Elmpt, W., Nijsten, S., Mijnheer, B., Dekker, A. and Lambin, P. (2008). "The next step in patient-specific QA: 3D dose verification of conformal and intensity-modulated RT based on EPID dosimetry and Monte Carlo dose calculations." Radiotherapy and Oncology **86**(1): 86-92.

van Elmpt, W., Petit, S., De Ruysscher, D., Lambin, P. and Dekker, A. (2010). "3D dose delivery verification using repeated cone-beam imaging and EPID dosimetry for stereotactic body radiotherapy of non-small cell lung cancer." Radiotherapy and Oncology **94**(2): 188-194.

Van Esch, A., Depuydt, T. and Huyskens, D. P. (2004). "The use of an aSi-based EPID for routine absolute dosimetric pre-treatment verification of dynamic IMRT fields." Radiotherapy and Oncology **71**(2): 223-234.

van Herk, M., Jaffray, D., Remeijer, P., Sonke, J.-J., Smitsmans, M. and Lebesque, J. (2004). Image guided radiotherapy. Proc. 14th Int. Conf on the Use of Computers in Radiation Therapy.

Vedantham, S., Karellas, A., Suryanarayanan, S., Albagli, D., Han, S., Tkaczyk, E. J., Landberg, C. E., Opsahl-Ong, B., Granfors, P. R., Levis, I., D'Orsi, C. J. and Hendrick, R. E. (2000). "Full breast digital mammography with an amorphous silicon-based flat panel detector: Physical characteristics of a clinical prototype." Med Phys **27**(3): 558-567.

Verellen, D. (2007). "Image-guided radiotherapy."

Wagener, D. T. (2009). The history of oncology, Bohn Stafleu van Loghum.

Warkentin, B., Steciw, S., Rathee, S. and Fallone, B. (2003). "Dosimetric IMRT verification with a flat-panel EPID." Med Phys **30**: 3143.

Warkentin, B., Steciw, S., Rathee, S. and Fallone, B. G. (2003). "Dosimetric IMRT verification with a flat-panel EPID." Med Phys **30**(12): 3143-3155.

Webb, S. (2003). "The physical basis of IMRT and inverse planning." British journal of radiology **76**(910): 678-689.

Wendling, M., Louwe, R. J., McDermott, L. N., Sonke, J.-J., van Herk, M. and Mijnheer, B. J. (2006). "Accurate two-dimensional IMRT verification using a back-projection EPID dosimetry method." Med Phys **33**: 259.

Wendling M, L. R., McDermott LN, Sonke JJ, van Herk M, and BJ., M. (2006). "Accurate two-dimensional IMRT verification using a back-projection EPID dosimetry method." Med Phys **33**.

Winkler, P. and Georg, D. (2006). "An intercomparison of 11 amorphous silicon EPIDs of the same type: implications for portal dosimetry." Phys Med Biol **51**(17): 4189.

Zelefsky, M. J., Chan, H., Hunt, M., Yamada, Y., Shippy, A. M. and Amols, H. (2006). "Long-term outcome of high dose intensity modulated radiation therapy for patients with clinically localized prostate cancer." J Urol **176**(4 Pt 1): 1415-1419.

Zietman, A. L., DeSilvio, M. L., Slater, J. D., Rossi Jr, C. J., Miller, D. W., Adams, J. A. and Shipley, W. U. (2005). "Comparison of conventional-dose vs high-dose conformal radiation therapy in clinically localized adenocarcinoma of the prostate." JAMA: the journal of the American Medical Association **294**(10): 1233-1239.

APPENDIX: FULL GAMMA RESULTS FOR ALL PHANTOMS

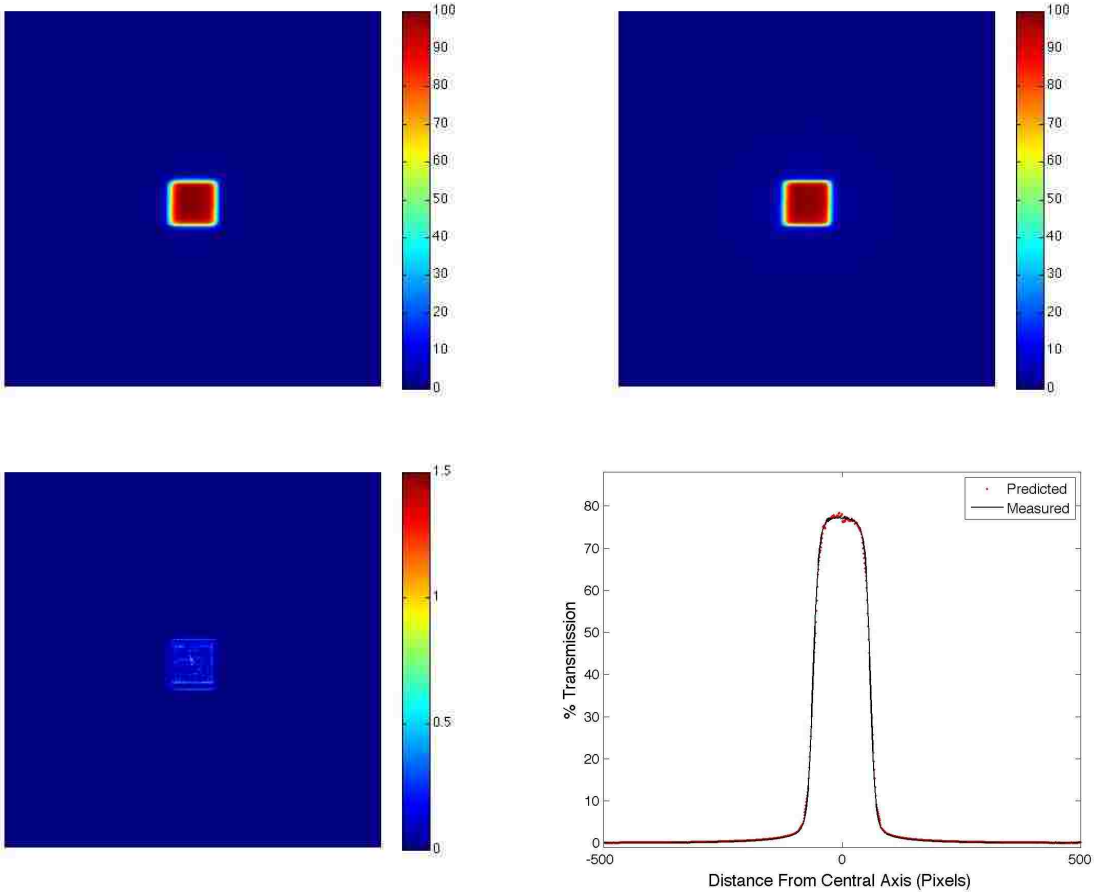

Figure A.0.1. ABOVE: Relative intensity maps for 3x3 FS, 5 cm phantom predicted (left) and measured (right) portal images. BELOW: 3x3 FS, 5 cm phantom gamma values (left) and % transmission relative to the through-air profiles (right).

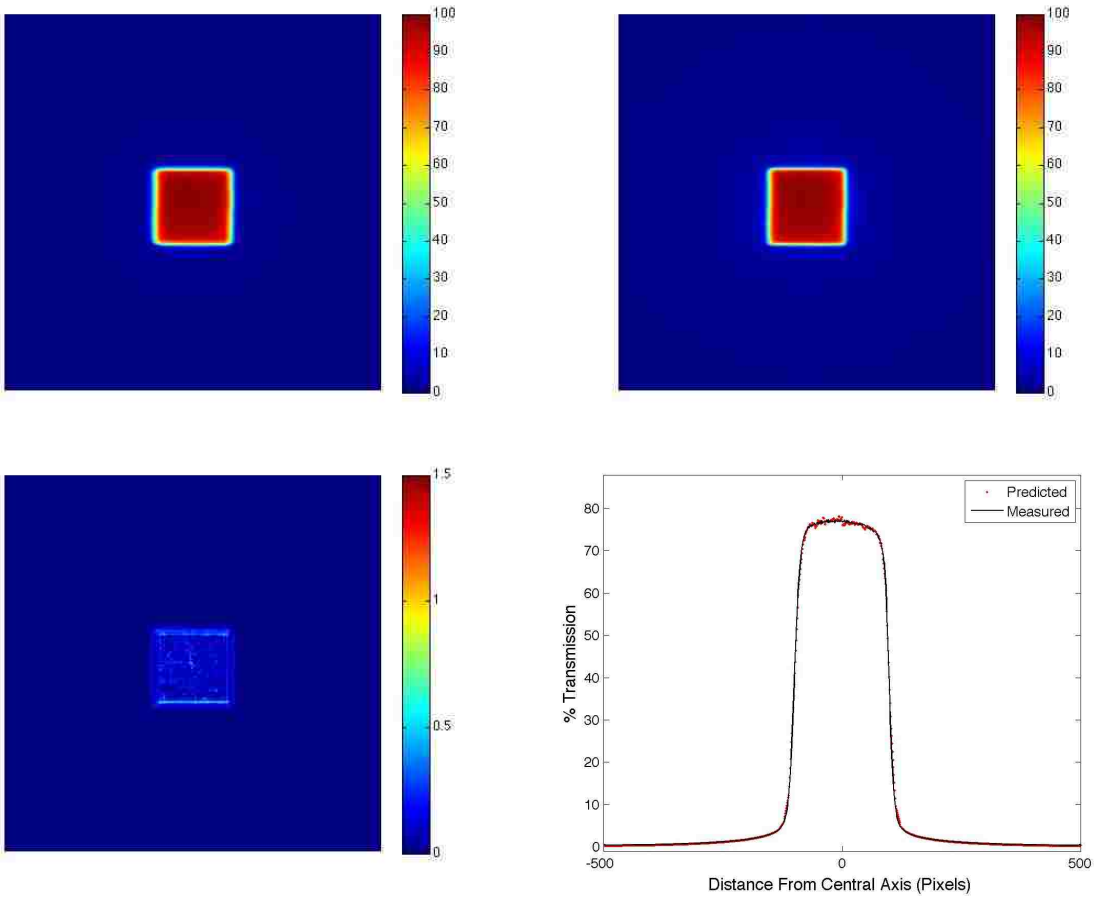

Figure A.0.2. ABOVE: Relative intensity maps for 5x5 FS, 5 cm phantom predicted (left) and measured (right) portal images. BELOW: 5x5 FS, 5 cm phantom gamma values (left) and % transmission relative to the through-air profiles (right).

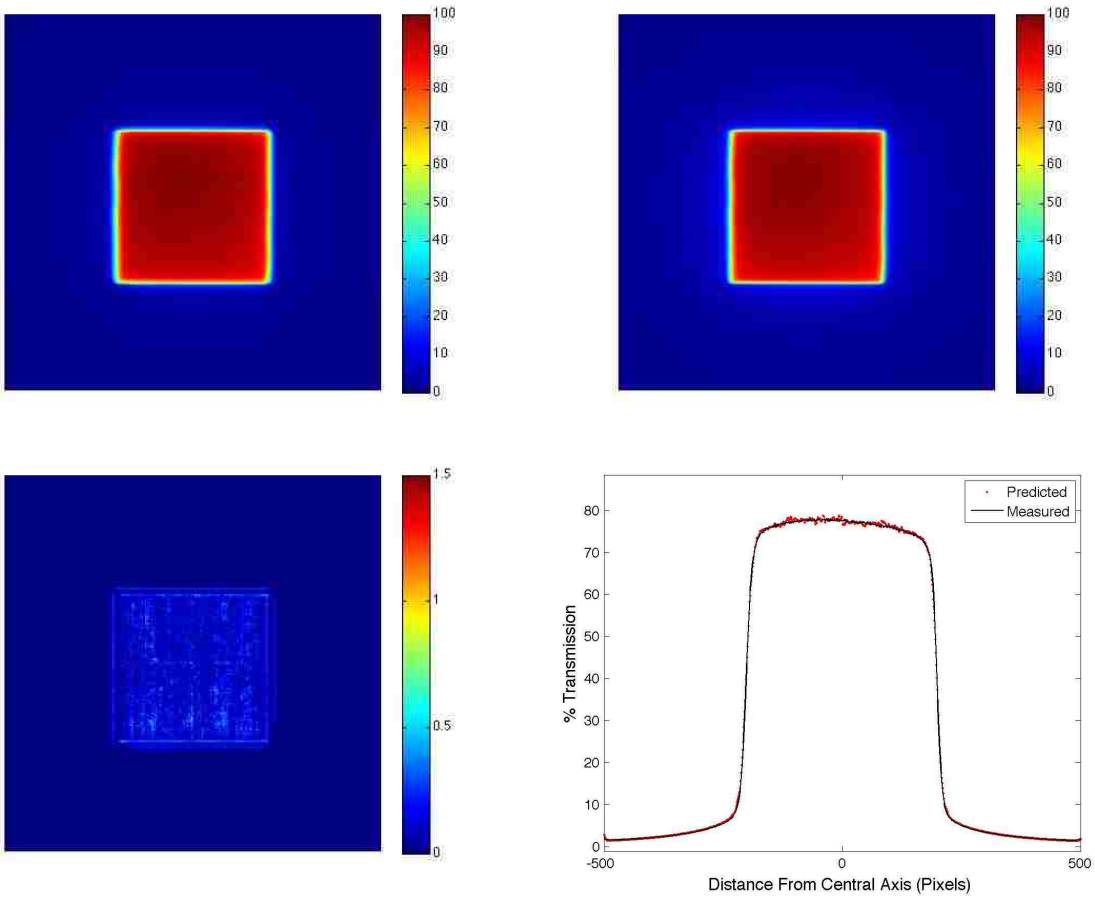

Figure A.0.3. ABOVE: Relative intensity maps for 10x10 FS, 5 cm phantom predicted (left) and measured (right) portal images. BELOW: 10x10 FS, 5 cm phantom gamma values (left) and % transmission relative to the through-air profiles (right).

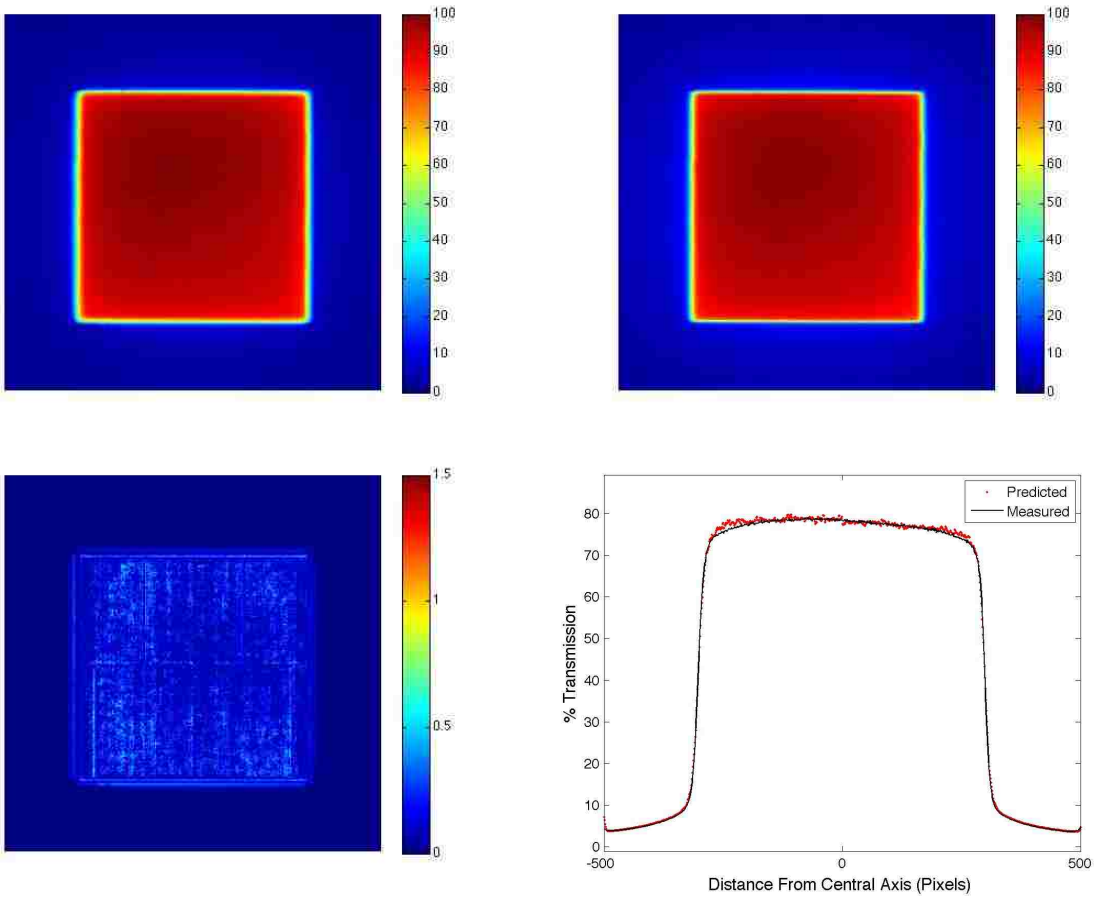

Figure A.0.4. ABOVE: Relative intensity maps for 15x15 FS, 5 cm phantom predicted (left) and measured (right) portal images. BELOW: 15x15 FS, 5 cm phantom gamma values (left) and % transmission relative to the through-air profiles (right).

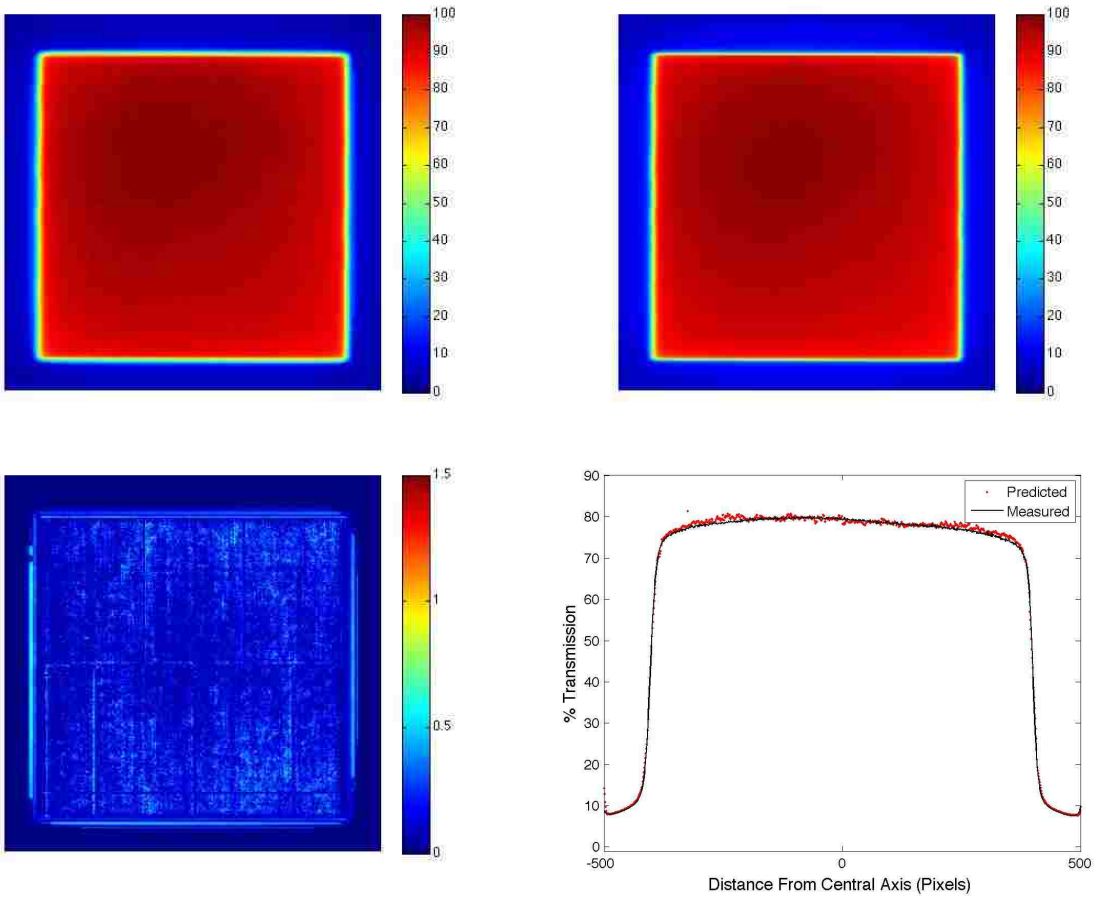

Figure A.0.5. ABOVE: Relative intensity maps for 20x20 FS, 5 cm phantom predicted (left) and measured (right) portal images. BELOW: 20x20 FS, 5 cm phantom gamma values (left) and % transmission relative to the through-air profiles (right).

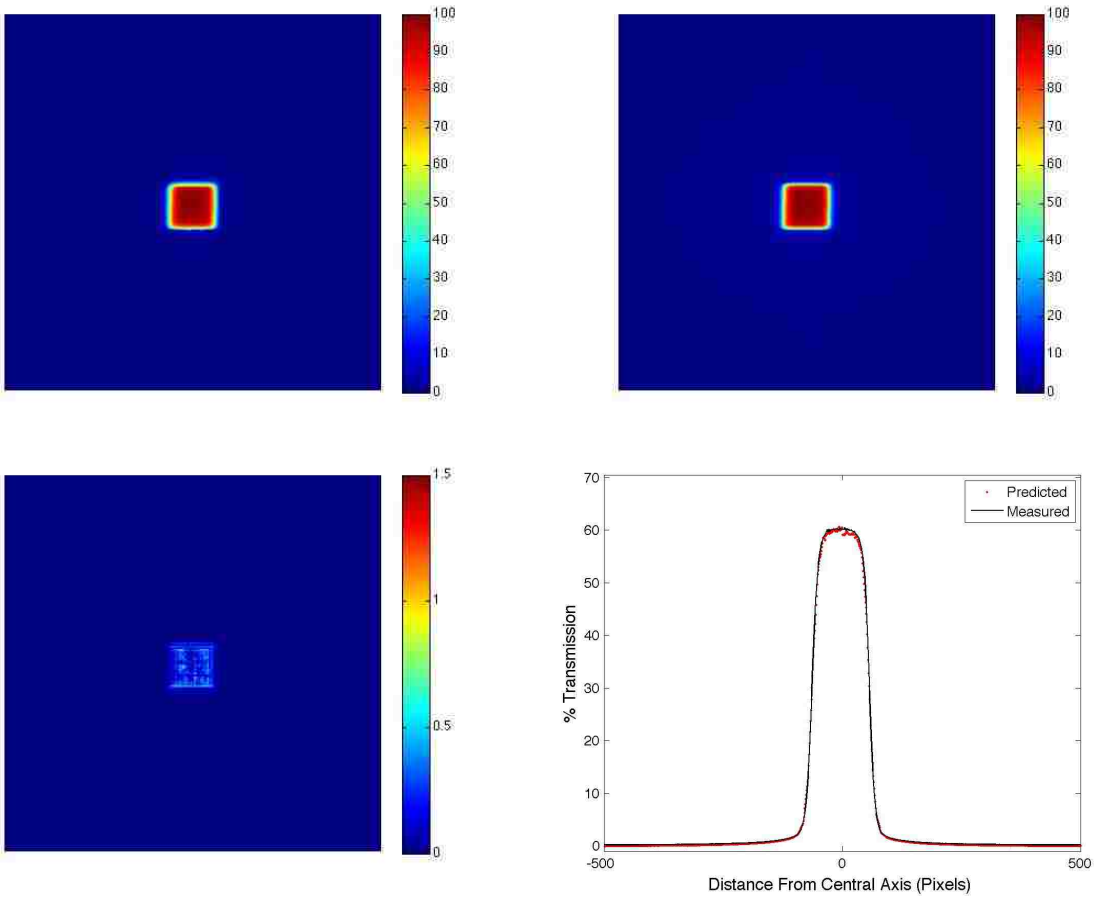

Figure A.0.6. ABOVE: Relative intensity maps for 3x3 FS, 10 cm phantom predicted (left) and measured (right) portal images. BELOW: 3x3 FS, 10cm phantom gamma values (left) and % transmission relative to the through-air profiles (right).

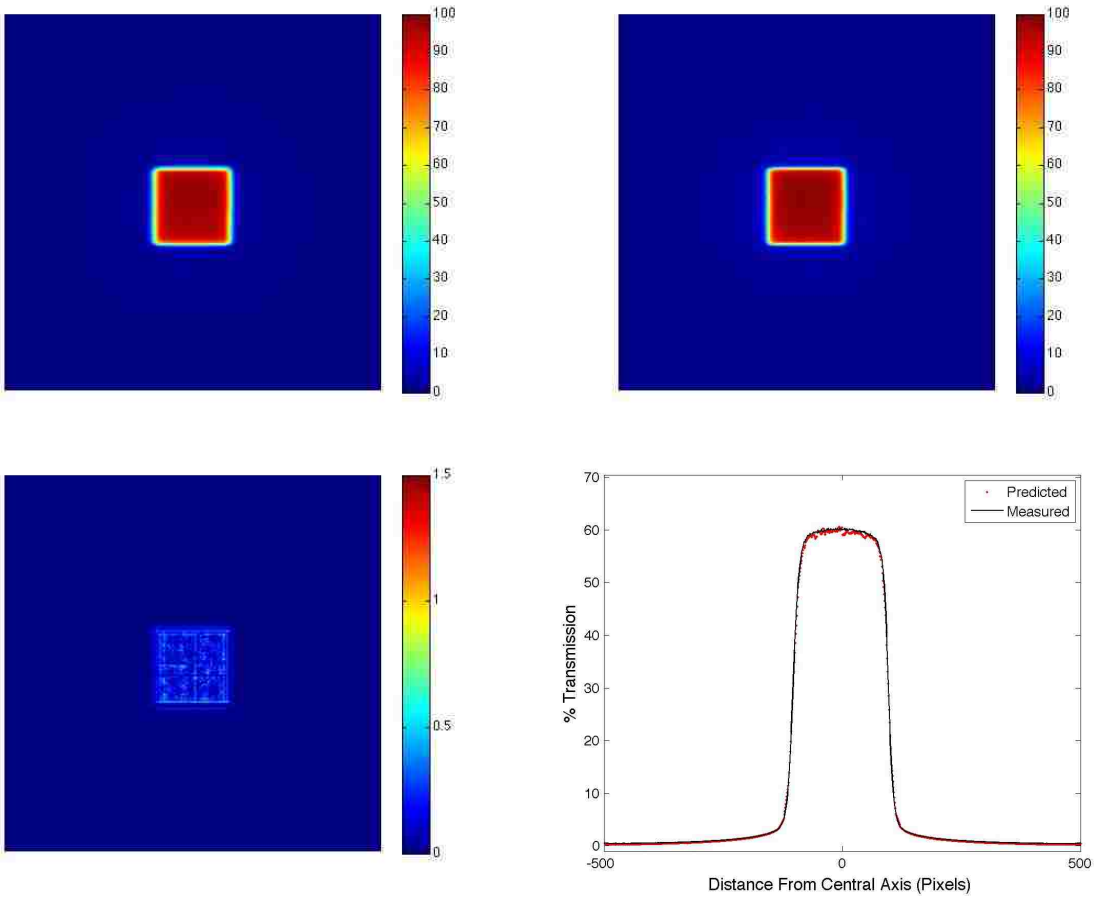

Figure A.0.7. ABOVE: Relative intensity maps for 5x5 FS, 10 cm phantom predicted (left) and measured (right) portal images. BELOW: 5x5 FS, 10cm phantom gamma values (left) and % transmission relative to the through-air profiles (right).

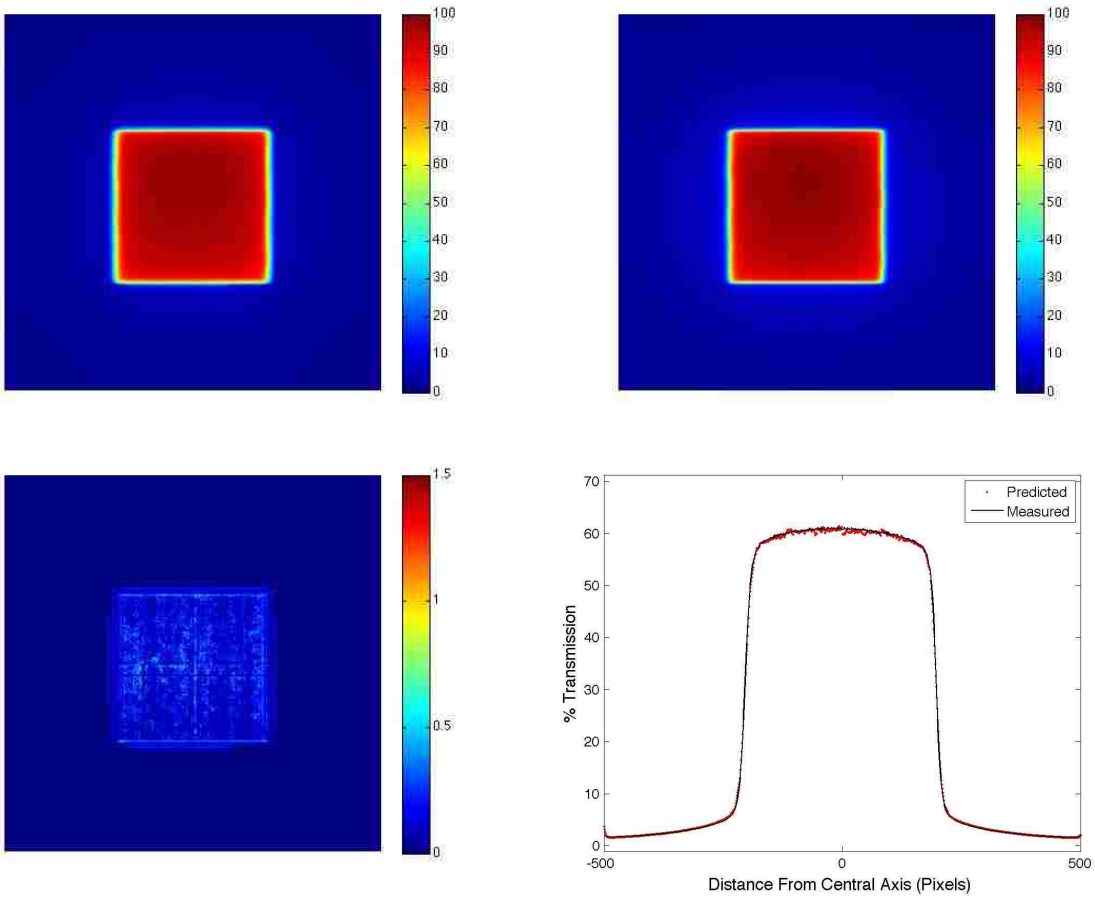

Figure A.0.8. ABOVE: Relative intensity maps for 10x10 FS, 10 cm phantom predicted (left) and measured (right) portal images. BELOW: 10x10 FS, 10cm phantom gamma values (left) and % transmission relative to the through-air profiles (right).

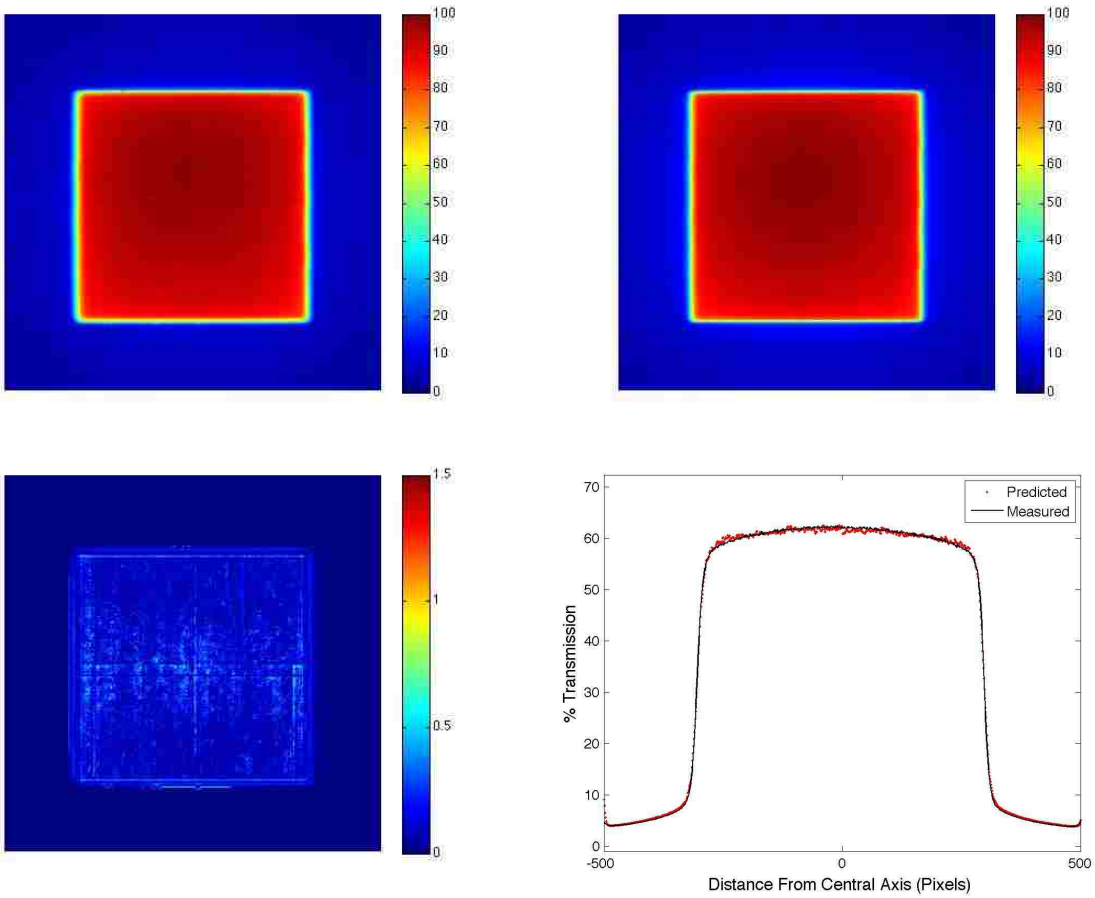

Figure A.0.9. ABOVE: Relative intensity maps for 15x15 FS, 10 cm phantom predicted (left) and measured (right) portal images. BELOW: 15x15 FS, 10cm phantom gamma values (left) and % transmission relative to the through-air profiles (right).

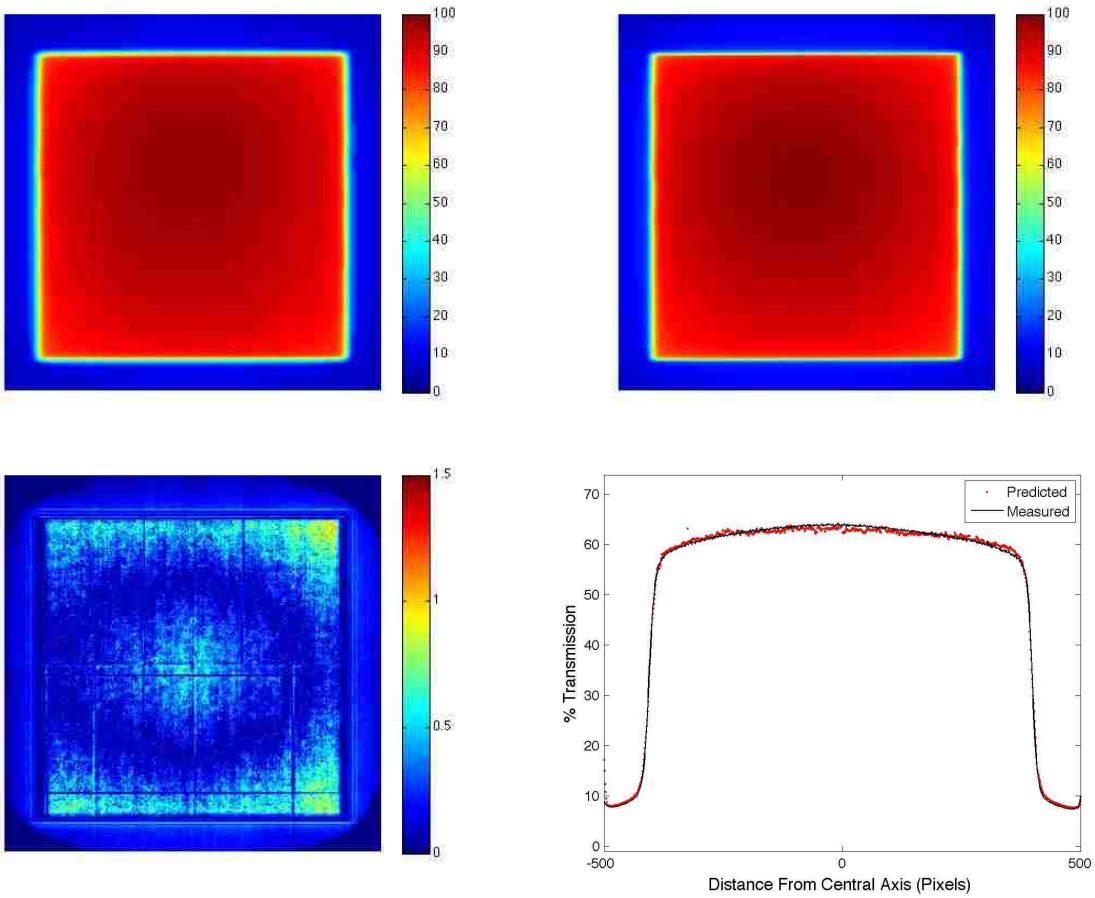

Figure A.0.10. ABOVE: Relative intensity maps for 20x20 FS, 10 cm phantom predicted (left) and measured (right) portal images. BELOW: 20x20 FS, 10cm phantom gamma values (left) and % transmission relative to the through-air profiles (right).

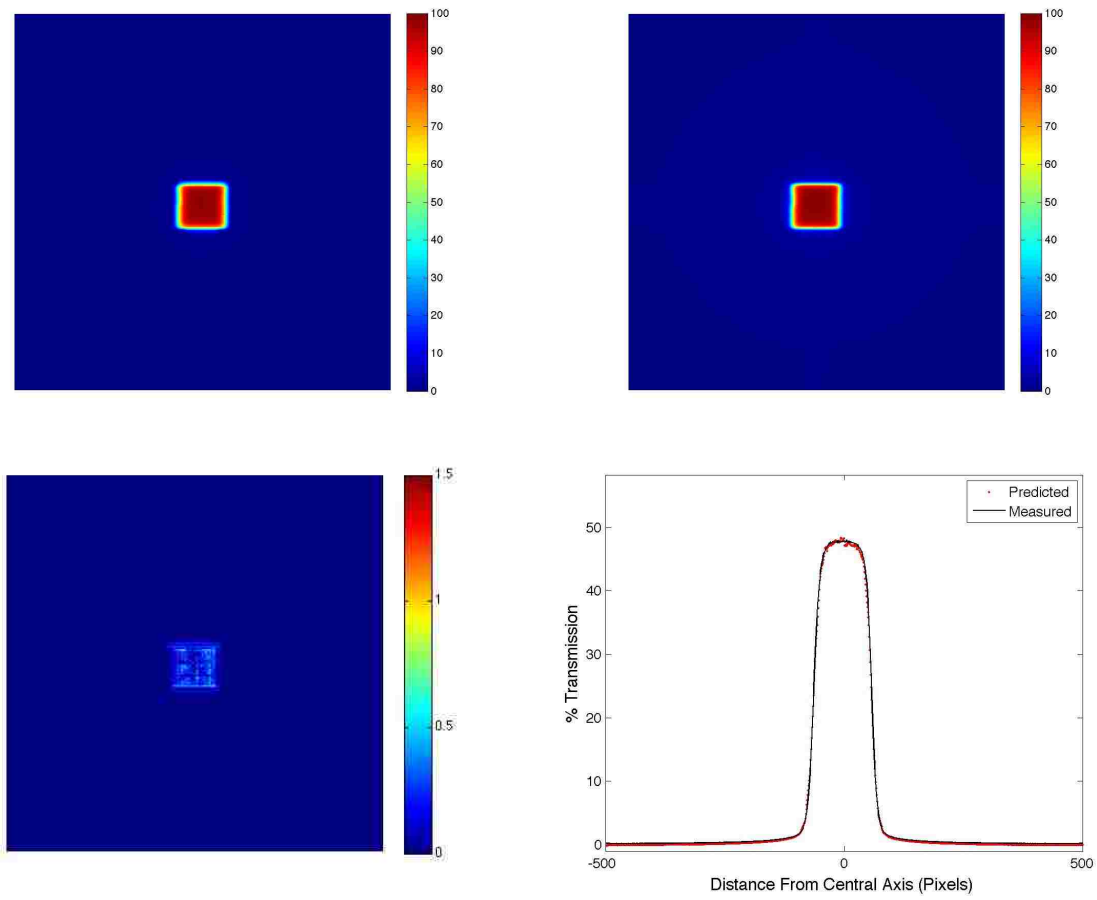

Figure A.0.11. ABOVE: Relative intensity maps for 3x3 FS, 15 cm phantom predicted (left) and measured (right) portal images. BELOW: 3x3 FS, 15cm phantom gamma values (left) and % transmission relative to the through-air profiles (right).

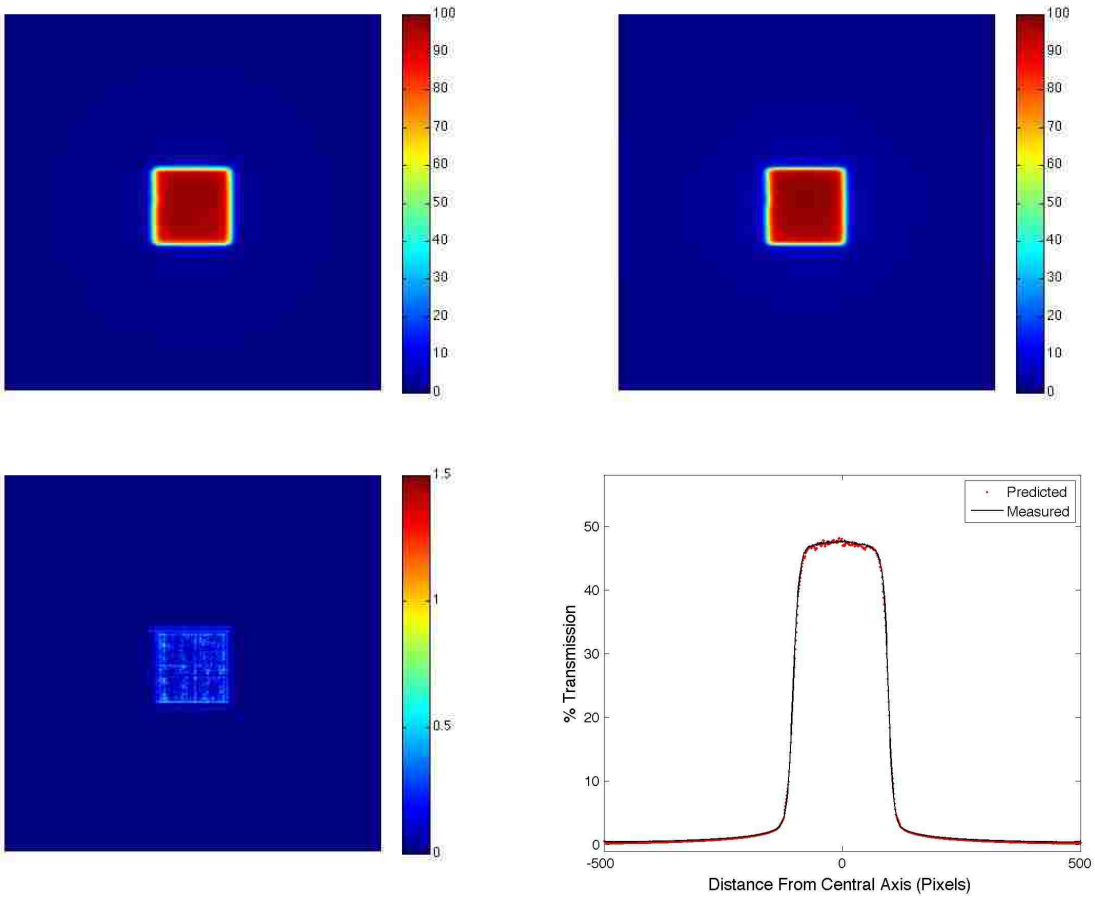

Figure A.0.12. ABOVE: Relative intensity maps for 5x5 FS, 15 cm phantom predicted (left) and measured (right) portal images. BELOW: 5x5 FS, 15cm phantom gamma values (left) and % transmission relative to the through-air profiles (right).

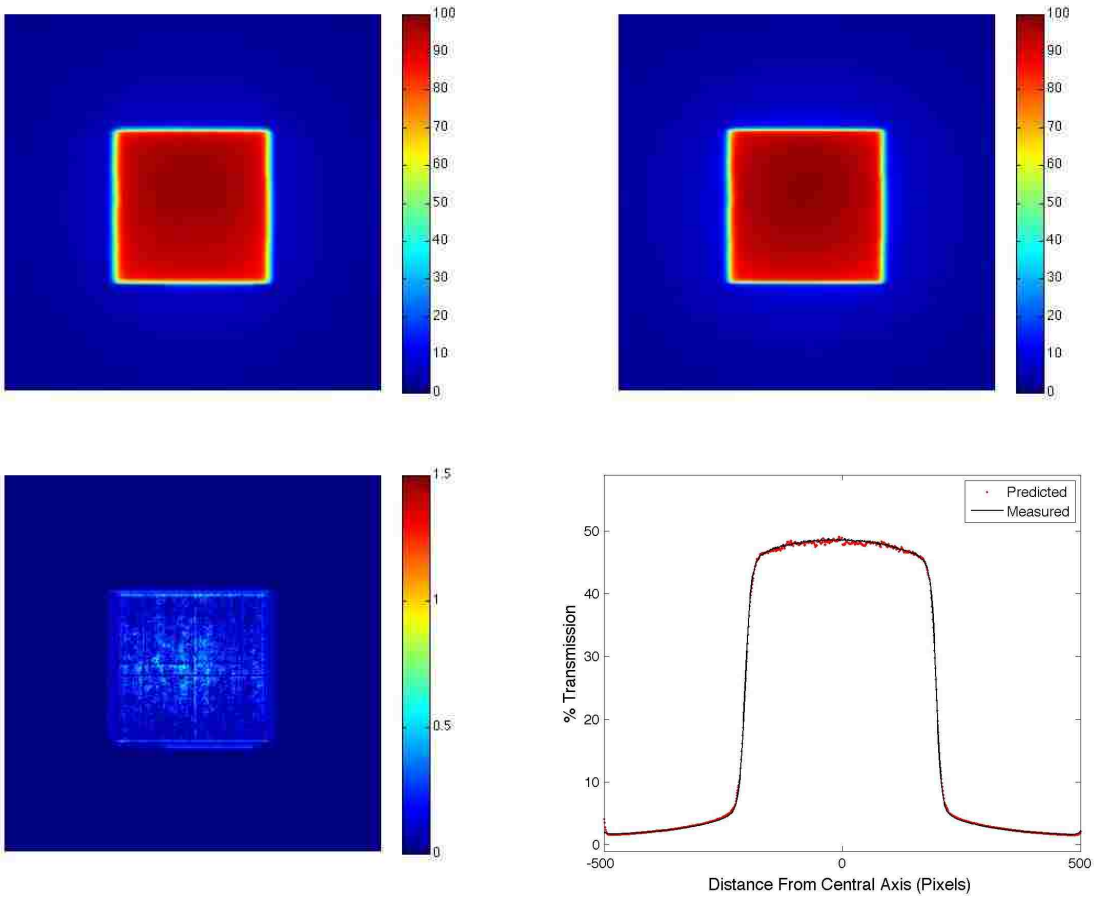

Figure A.0.13. ABOVE: Relative intensity maps for 10x10 FS, 15 cm phantom predicted (left) and measured (right) portal images. BELOW: 10x10 FS, 15cm phantom gamma values (left) and % transmission relative to the through-air profiles (right).

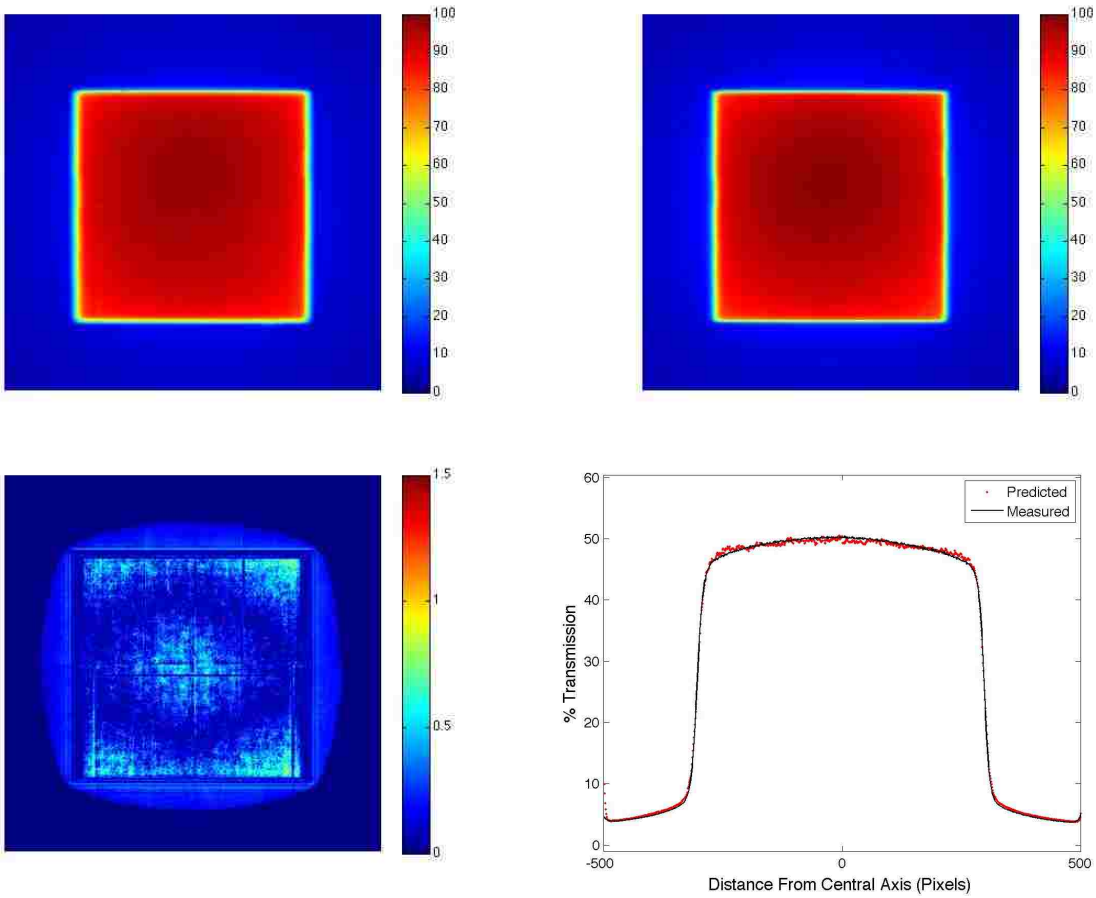

Figure A.0.14. ABOVE: Relative intensity maps for 15x15 FS, 15 cm phantom predicted (left) and measured (right) portal images. BELOW: 15x15 FS, 15cm phantom gamma values (left) and % transmission relative to the through-air profiles (right).

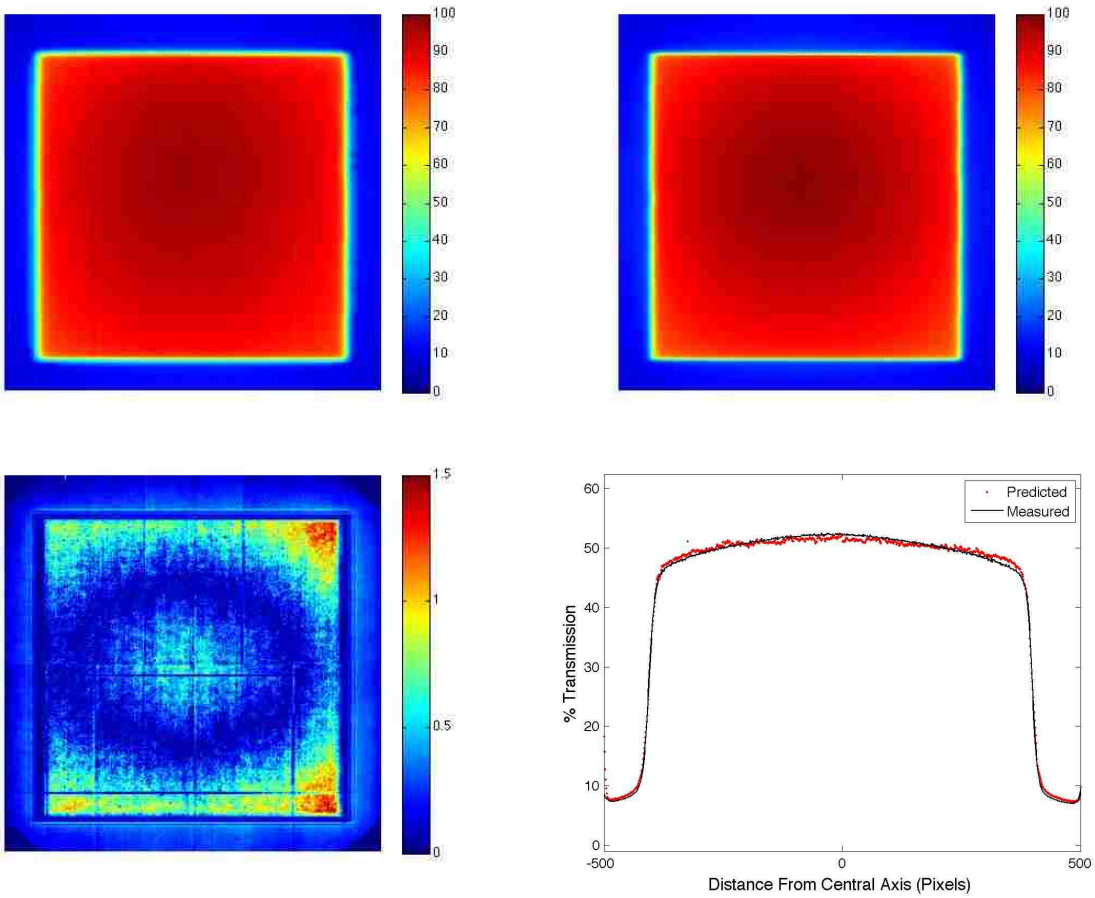

Figure A.0.15. ABOVE: Relative intensity maps for 20x20 FS, 15 cm phantom predicted (left) and measured (right) portal images. BELOW: 20x20 FS, 15cm phantom gamma values (left) and % transmission relative to the through-air profiles (right).

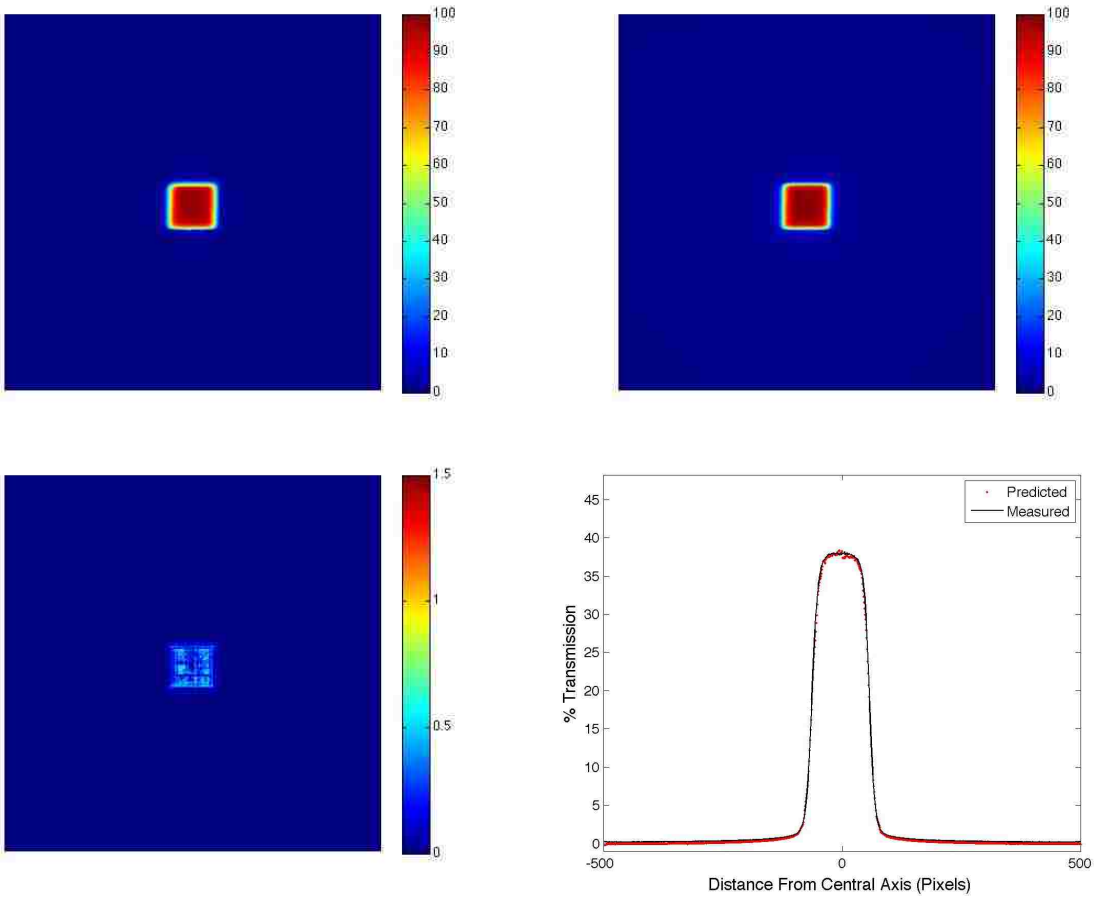

Figure A.0.16. ABOVE: Relative intensity maps for 3x3 FS, 20 cm phantom predicted (left) and measured (right) portal images. BELOW: 3x3 FS, 20cm phantom gamma values (left) and % transmission relative to the through-air profiles (right).

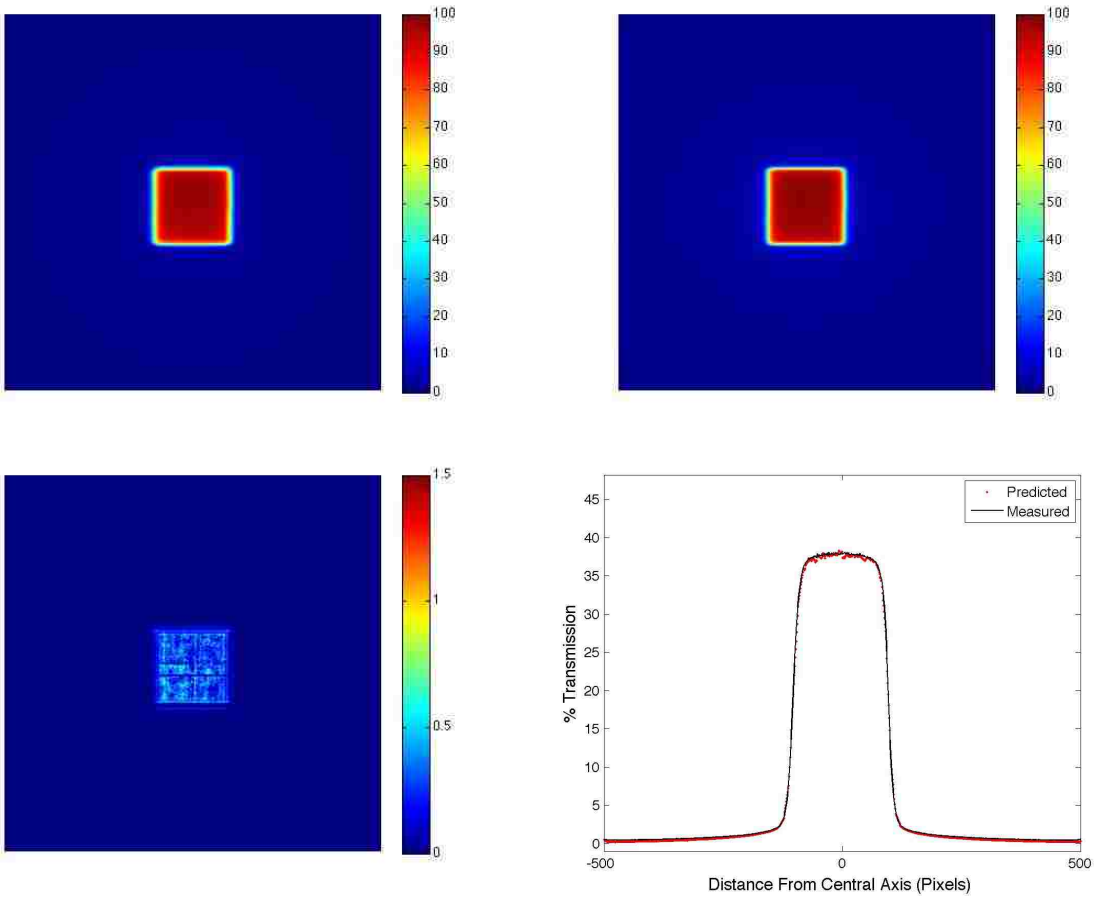

Figure A.0.17. ABOVE: Relative intensity maps for 5x5 FS, 20 cm phantom predicted (left) and measured (right) portal images. BELOW: 5x5 FS, 20cm phantom gamma values (left) and % transmission relative to the through-air profiles (right).

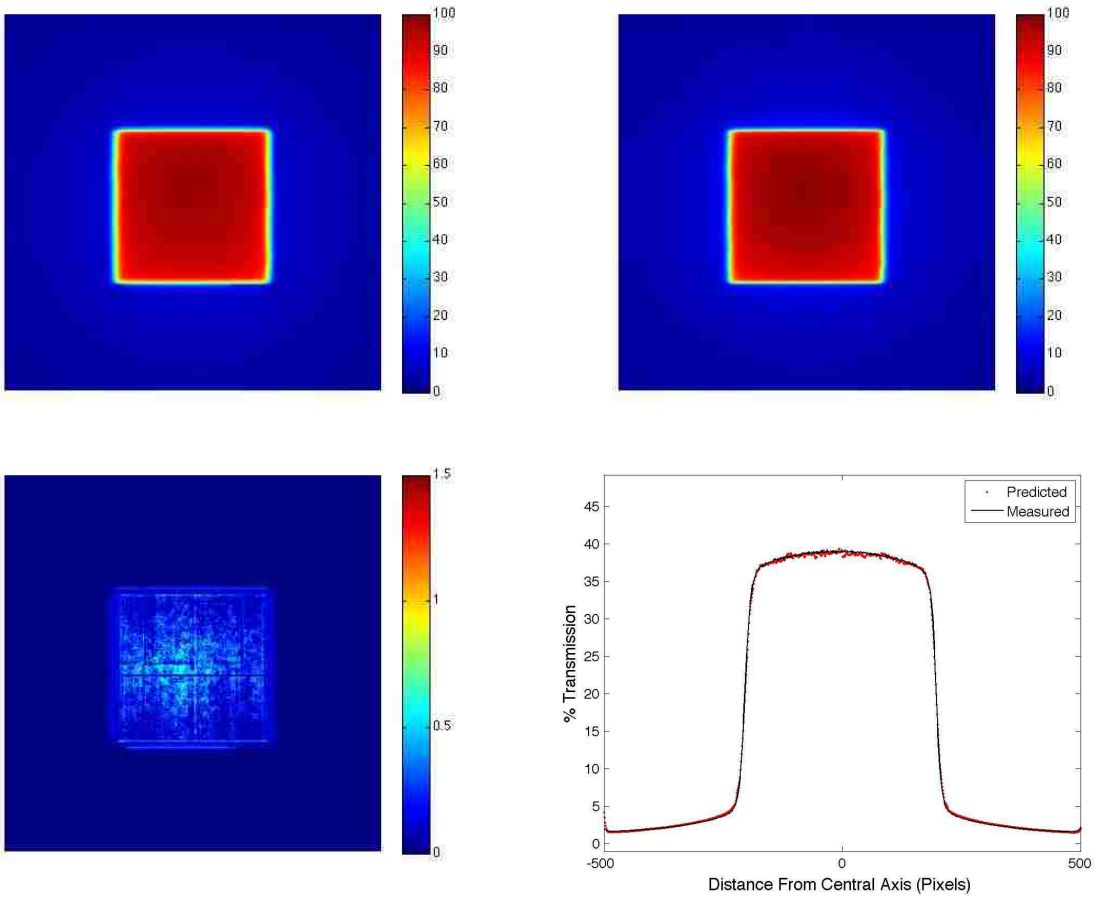

Figure A.0.18. ABOVE: Relative intensity maps for 10x10 FS, 20 cm phantom predicted (left) and measured (right) portal images. BELOW: 10x10 FS, 20cm phantom gamma values (left) and % transmission relative to the through-air profiles (right).

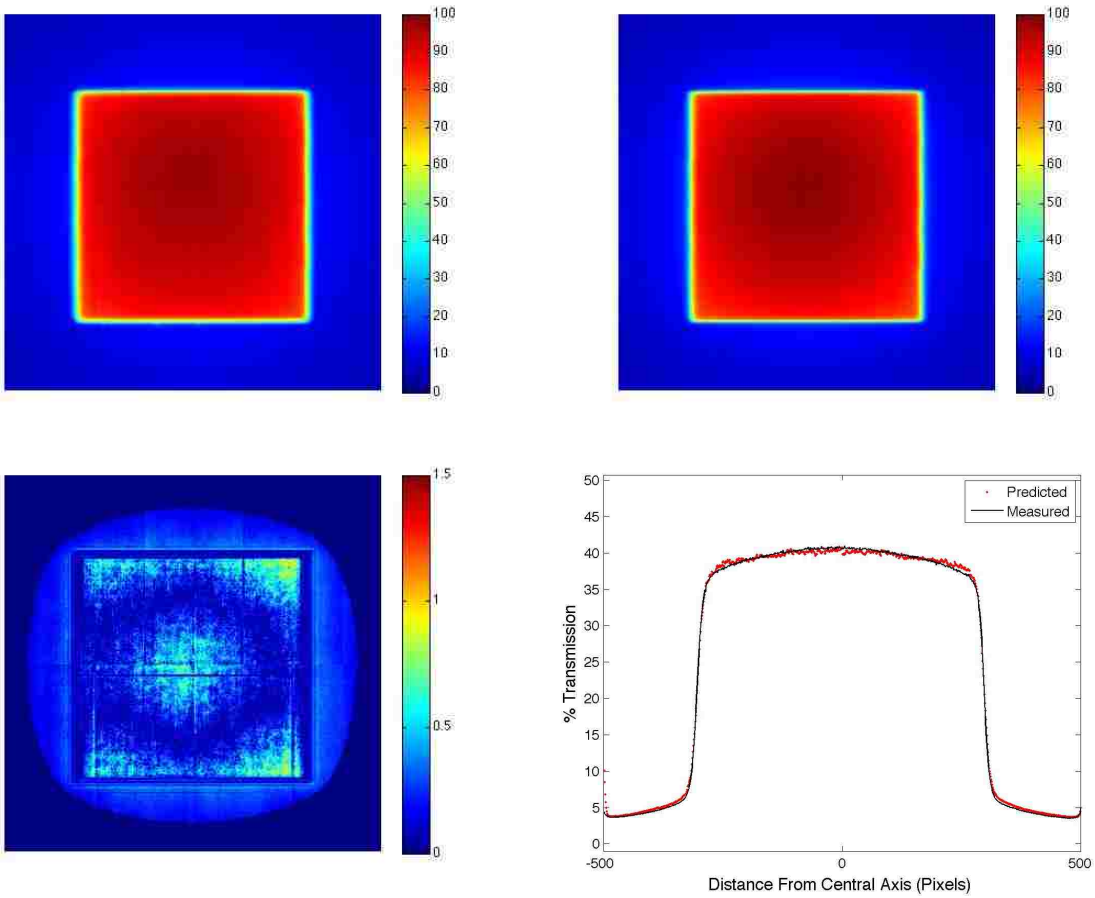

Figure A.0.19. ABOVE: Relative intensity maps for 15x15 FS, 20 cm phantom predicted (left) and measured (right) portal images. BELOW: 15x15 FS, 20cm phantom gamma values (left) and % transmission relative to the through-air profiles (right).

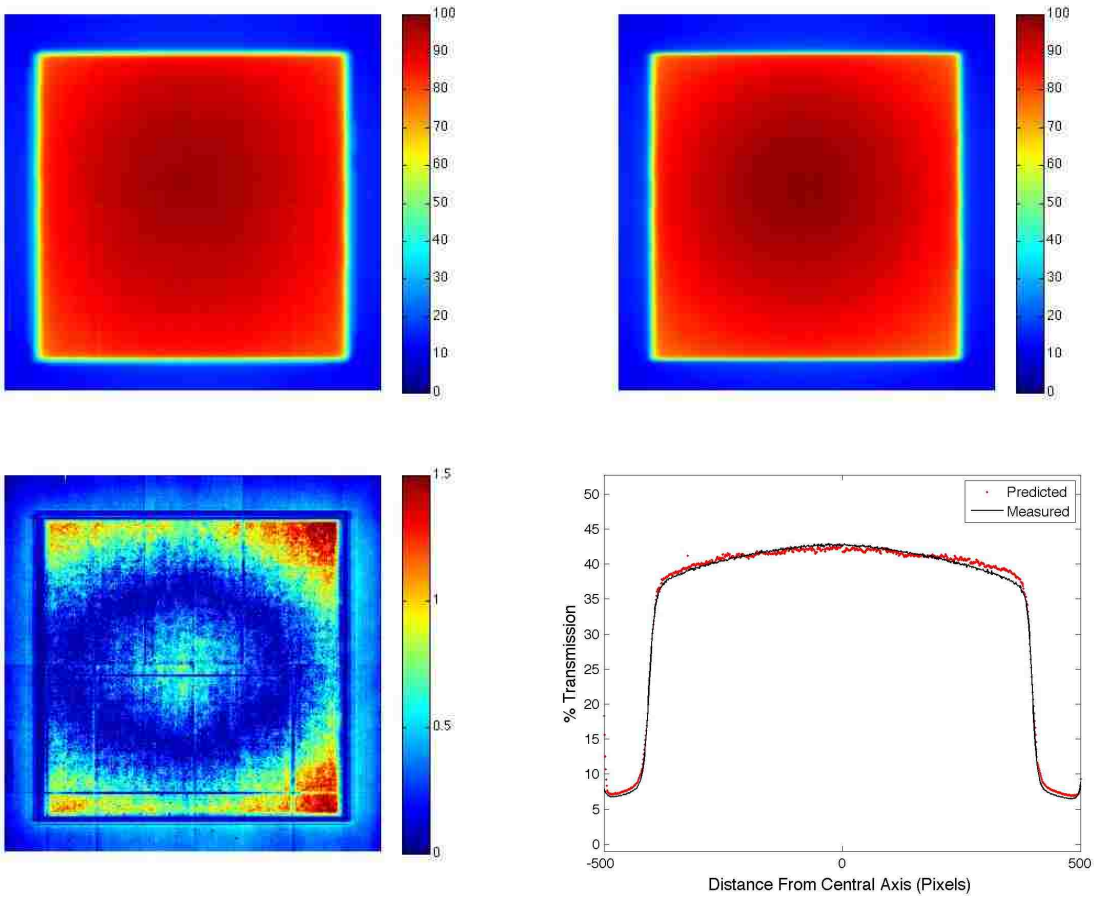

Figure A.0.20. ABOVE: Relative intensity maps for 20x20 FS, 20 cm phantom predicted (left) and measured (right) portal images. BELOW: 20x20 FS, 20cm phantom gamma values (left) and % transmission relative to the through-air profiles (right).

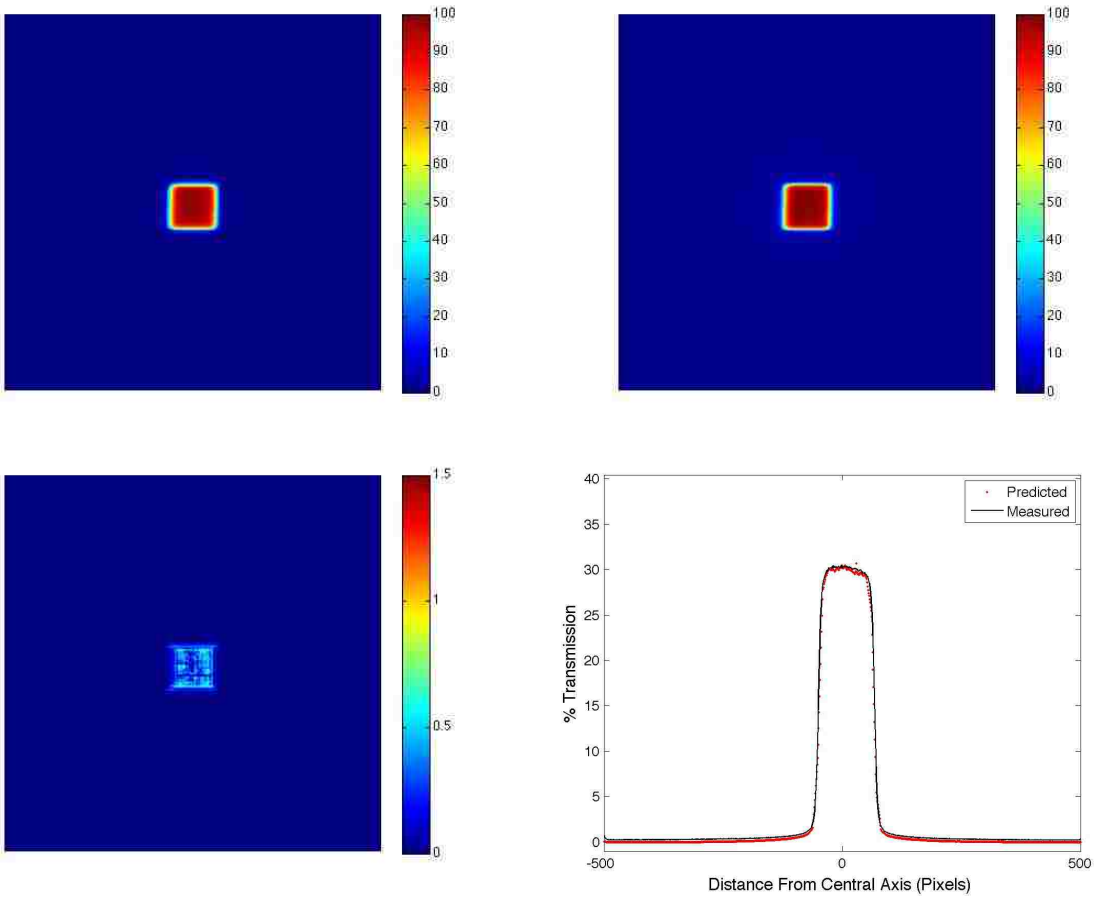

Figure A.0.21. ABOVE: Relative intensity maps for 3x3 FS, 25 cm phantom predicted (left) and measured (right) portal images. BELOW: 3x3 FS, 25cm phantom gamma values (left) and % transmission relative to the through-air profiles (right).

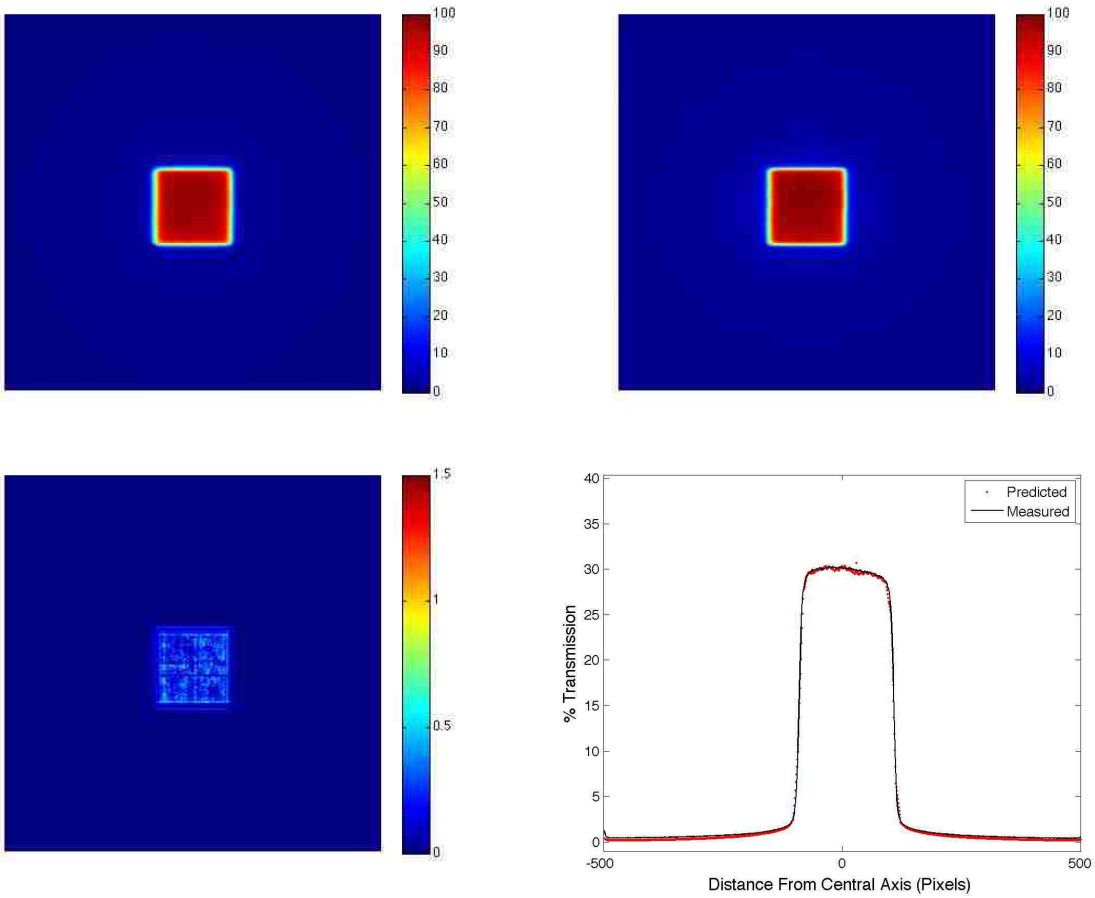

Figure A.0.22. ABOVE: Relative intensity maps for 5x5 FS, 25 cm phantom predicted (left) and measured (right) portal images. BELOW: 5x5 FS, 25cm phantom gamma values (left) and % transmission relative to the through-air profiles (right).

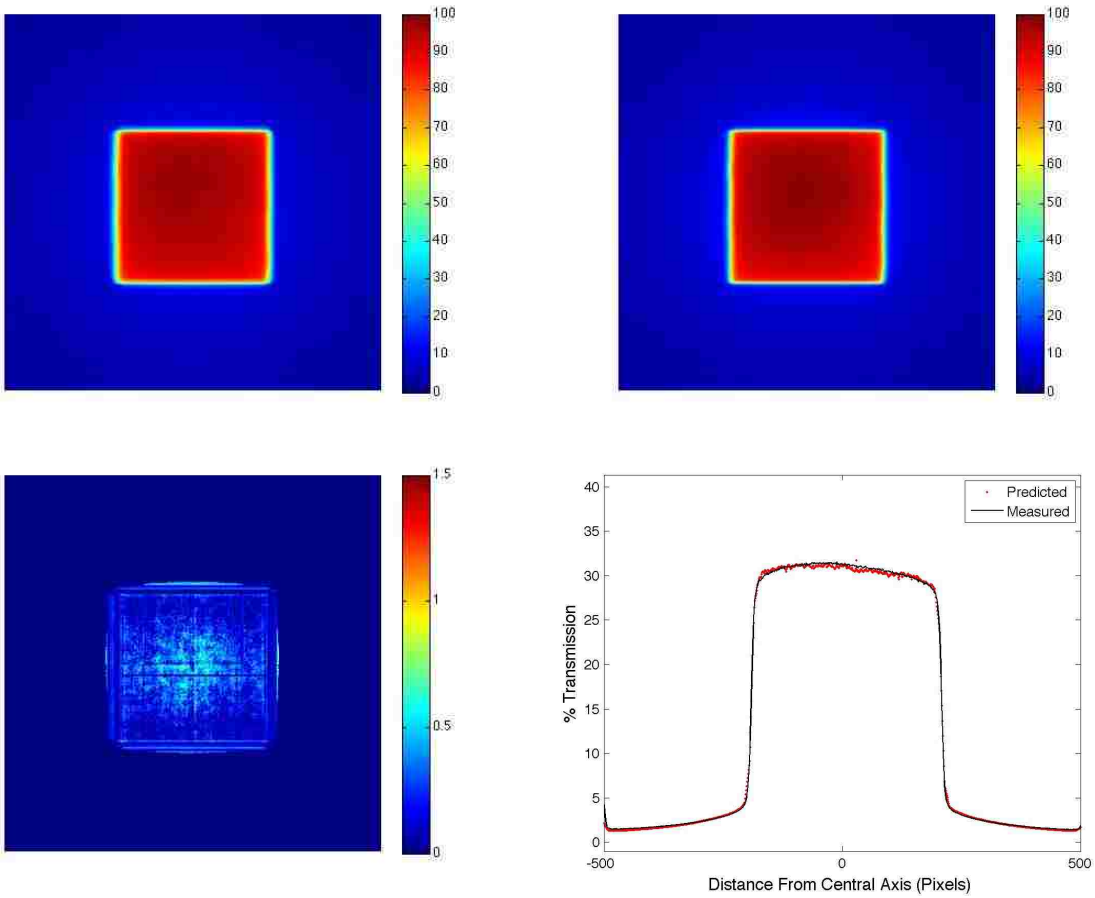

Figure A.0.23. ABOVE: Relative intensity maps for 10x10 FS, 25 cm phantom predicted (left) and measured (right) portal images. BELOW: 10x10 FS, 25cm phantom gamma values (left) and % transmission relative to the through-air profiles (right).

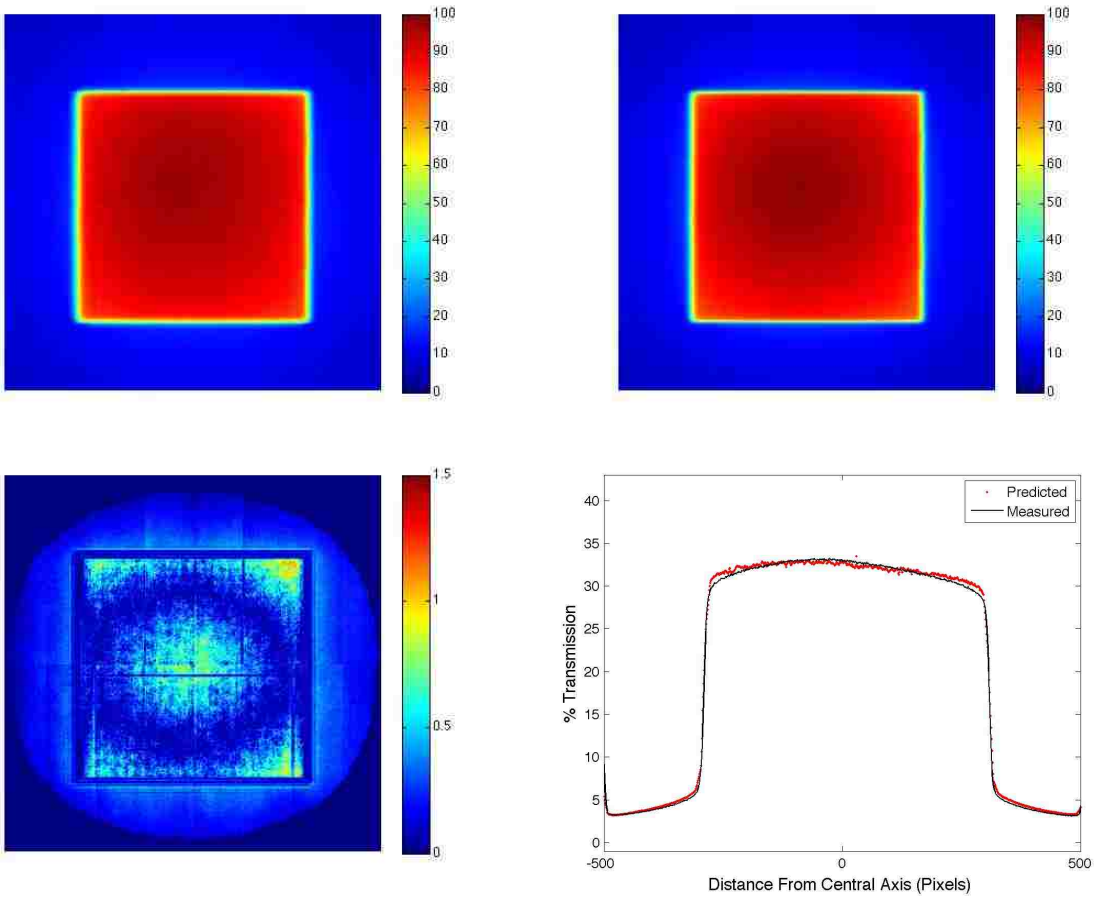

Figure A.0.24. ABOVE: Relative intensity maps for 15x15 FS, 25 cm phantom predicted (left) and measured (right) portal images. BELOW: 15x15 FS, 25cm phantom gamma values (left) and % transmission relative to the through-air profiles (right).

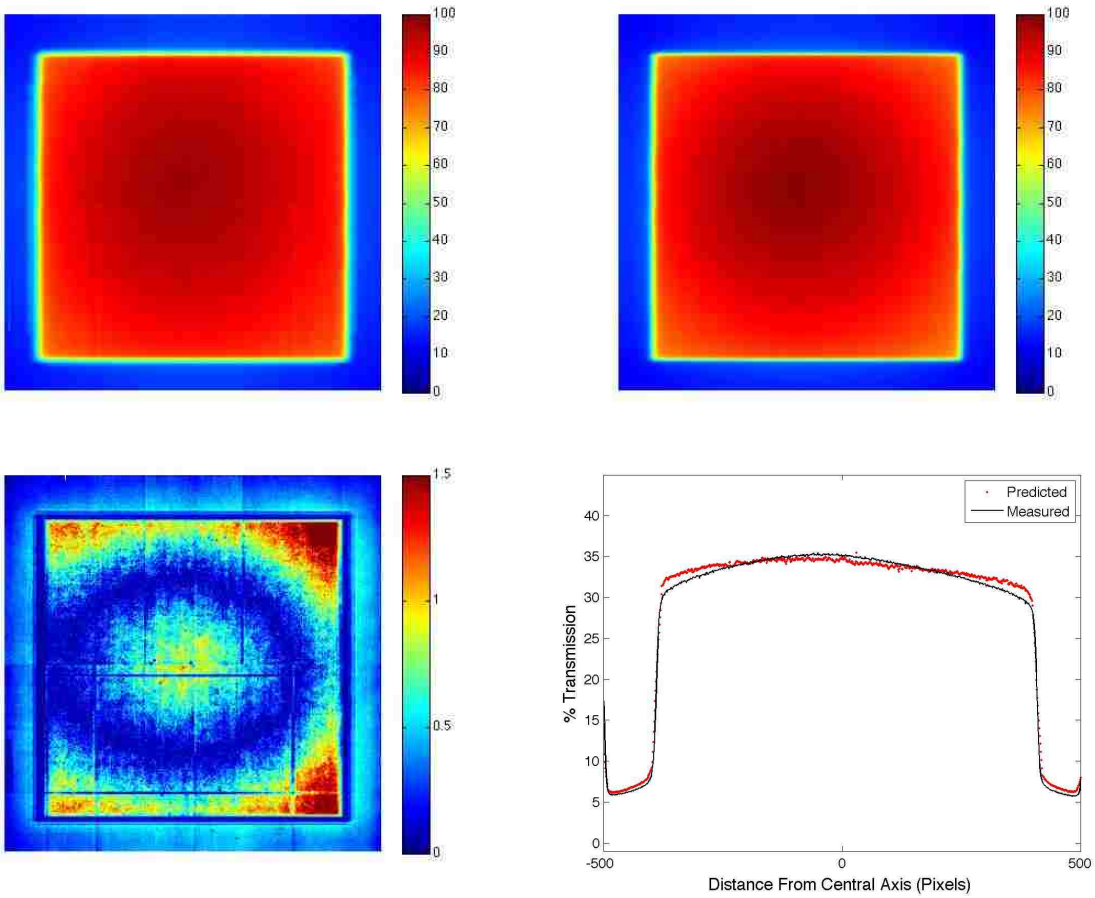

Figure A.0.25. ABOVE: Relative intensity maps for 20x20 FS, 25 cm phantom predicted (left) and measured (right) portal images. BELOW: 20x20 FS, 25cm phantom gamma values (left) and % transmission relative to the through-air profiles (right).

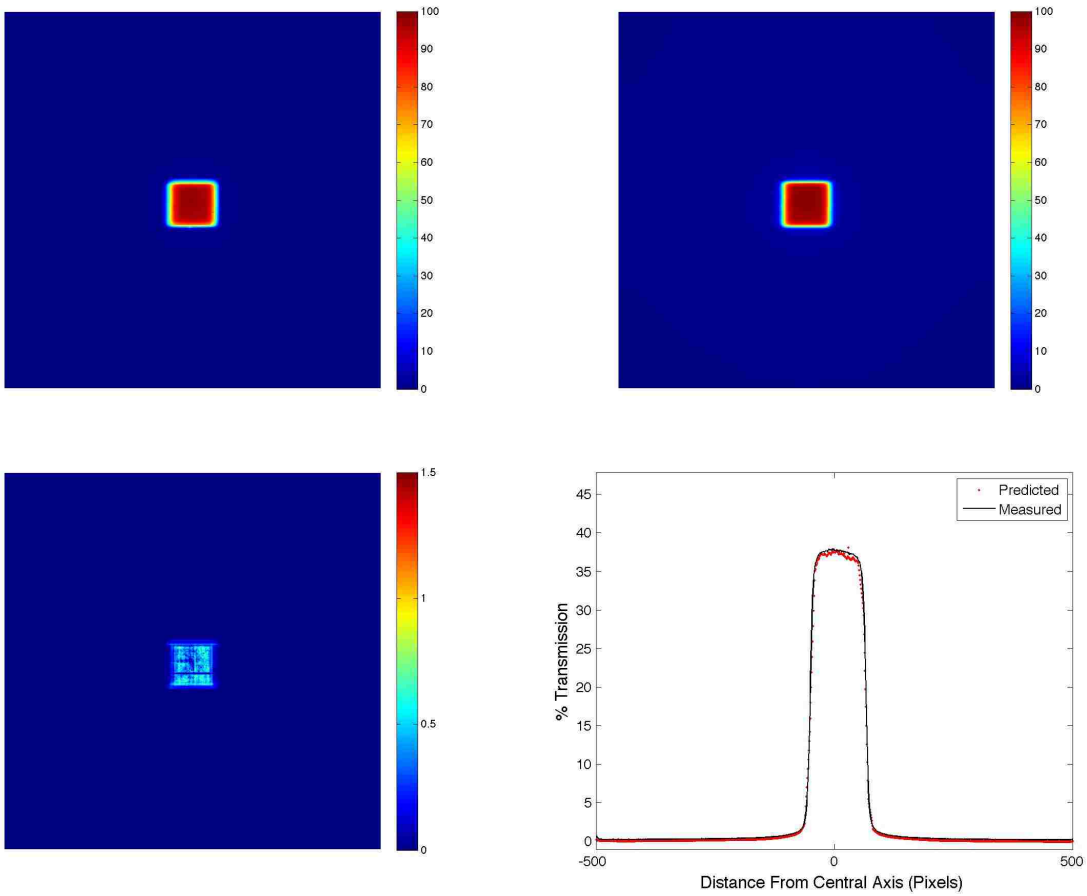

Figure A.0.26. ABOVE: Relative intensity maps for 3x3 FS, homogeneous phantom predicted (left) and measured (right) portal images. BELOW: 3x3 FS, homogeneous phantom gamma values (left) and % transmission relative to the through-air profiles (right).

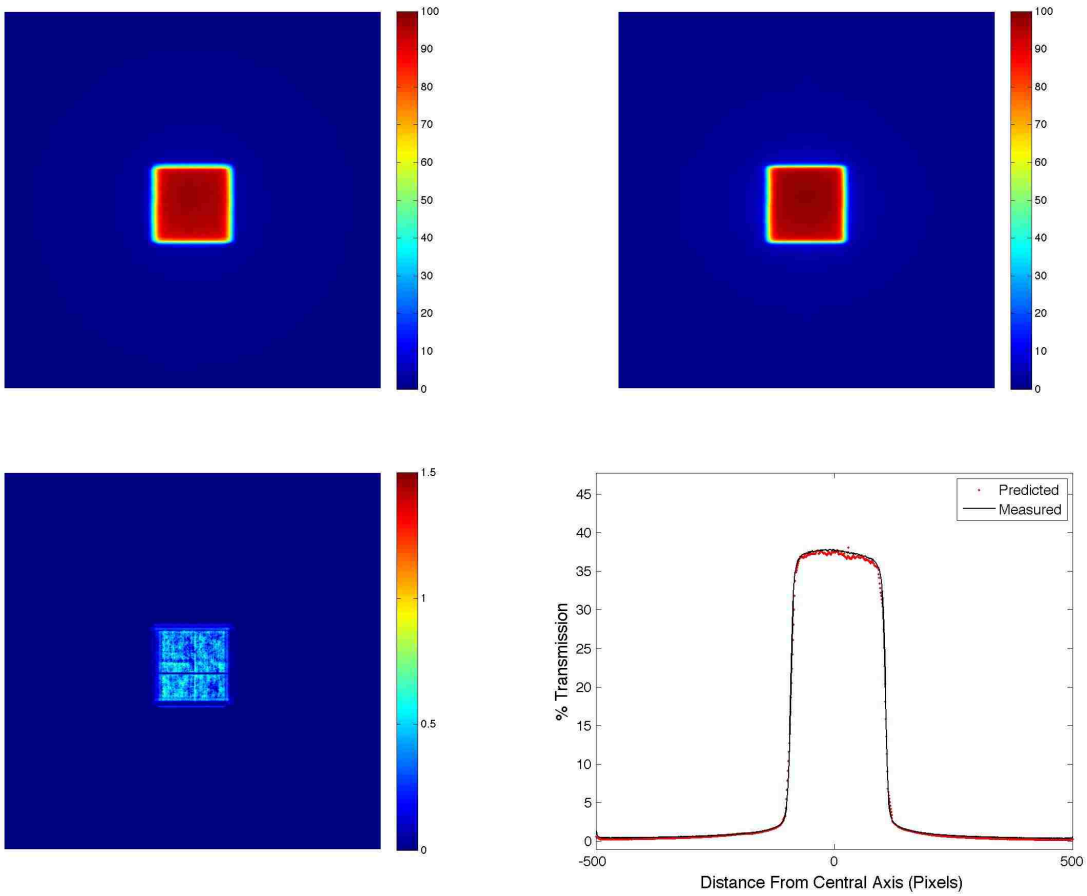

Figure A.0.27. ABOVE: Relative intensity maps for 5x5 FS, homogeneous phantom predicted (left) and measured (right) portal images. BELOW: 5x5 FS, homogeneous phantom gamma values (left) and % transmission relative to the through-air profiles (right).

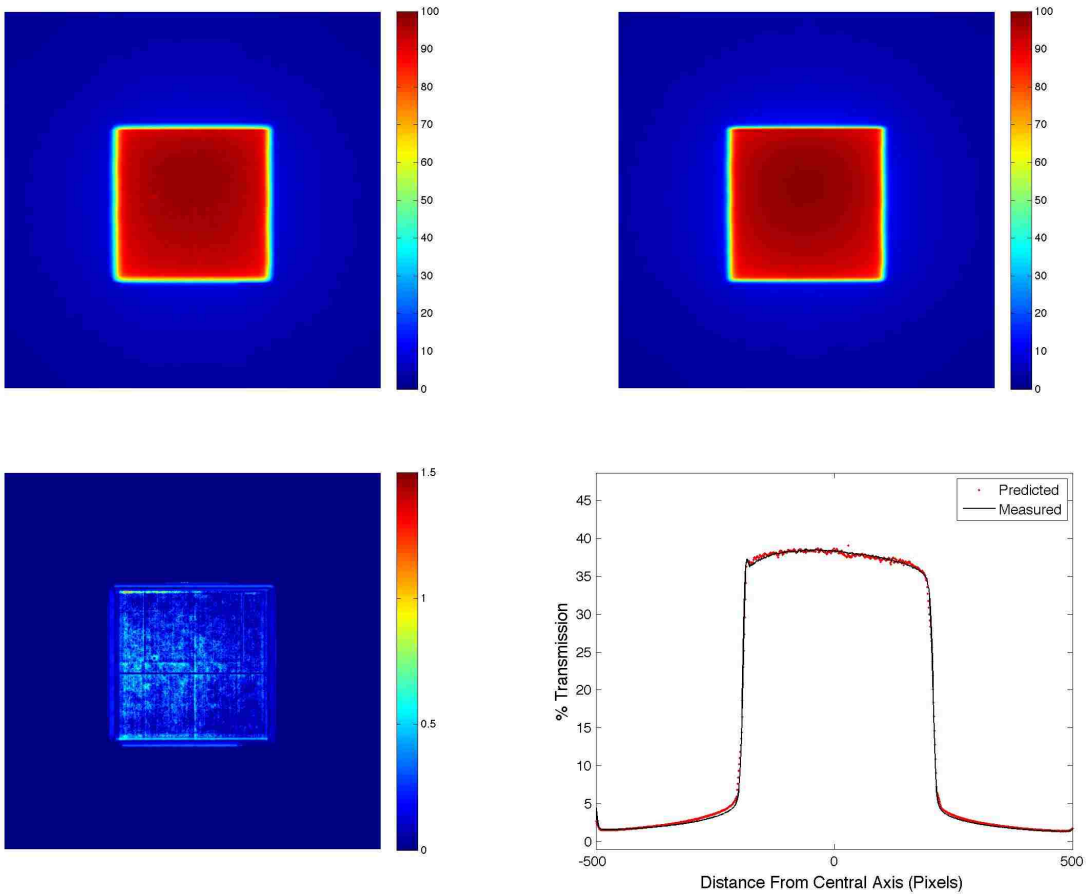

Figure A.0.28. ABOVE: Relative intensity maps for 10x10 FS, homogeneous phantom predicted (left) and measured (right) portal images. BELOW: 10x10 FS, homogeneous phantom gamma values (left) and % transmission relative to the through-air profiles (right).

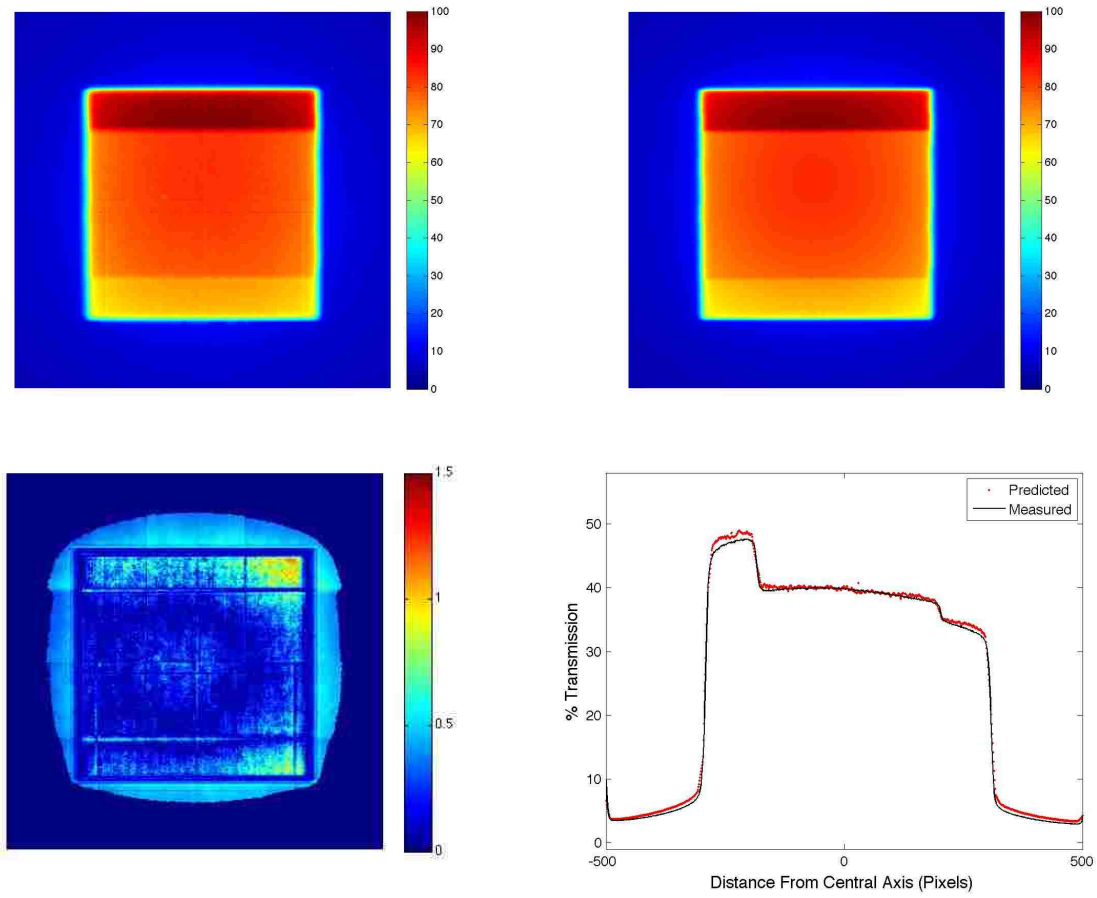

Figure A.0.29. ABOVE: Relative intensity maps for 15x15 FS, homogeneous phantom predicted (left) and measured (right) portal images. BELOW: 15x15 FS, homogeneous phantom gamma values (left) and % transmission relative to the through-air profiles (right).

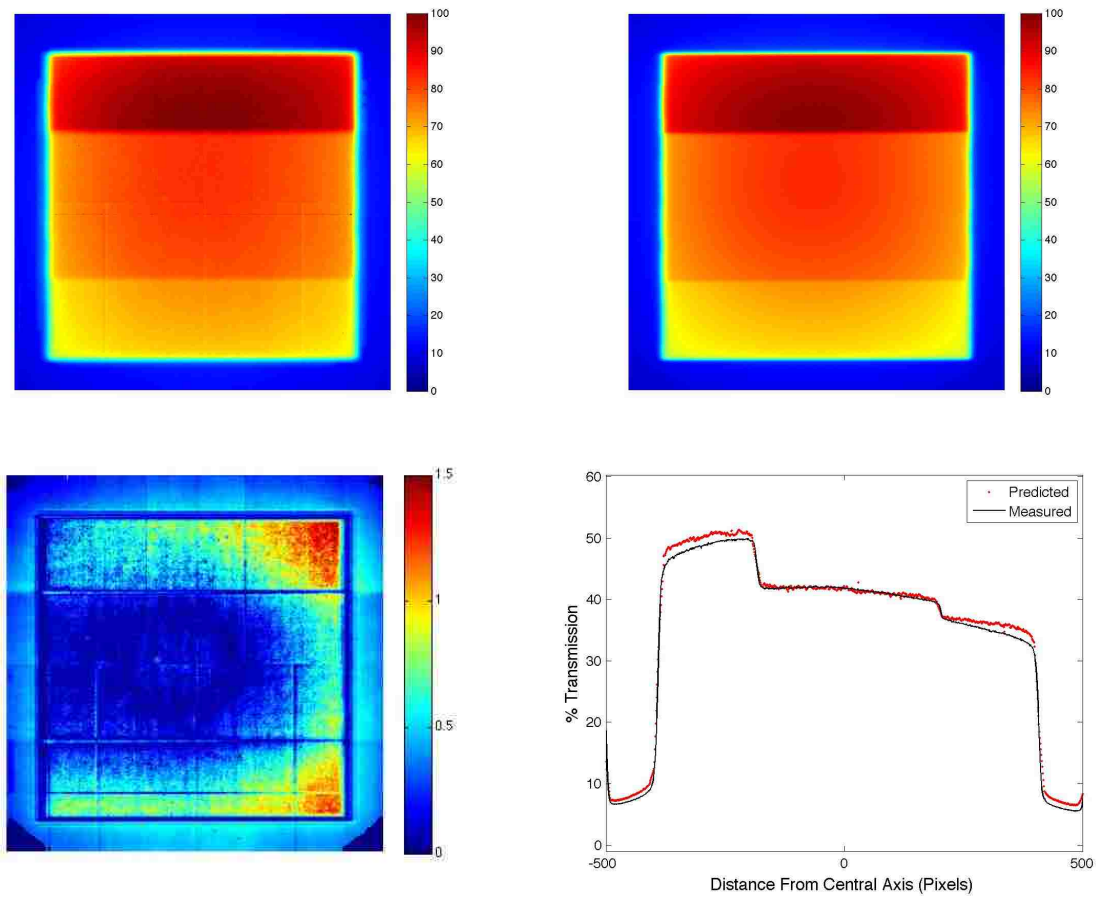

Figure A.0.30. ABOVE: Relative intensity maps for 20x20 FS, homogeneous phantom predicted (left) and measured (right) portal images. BELOW: 20x20 FS, homogeneous phantom gamma values (left) and % transmission relative to the through-air profiles (right).

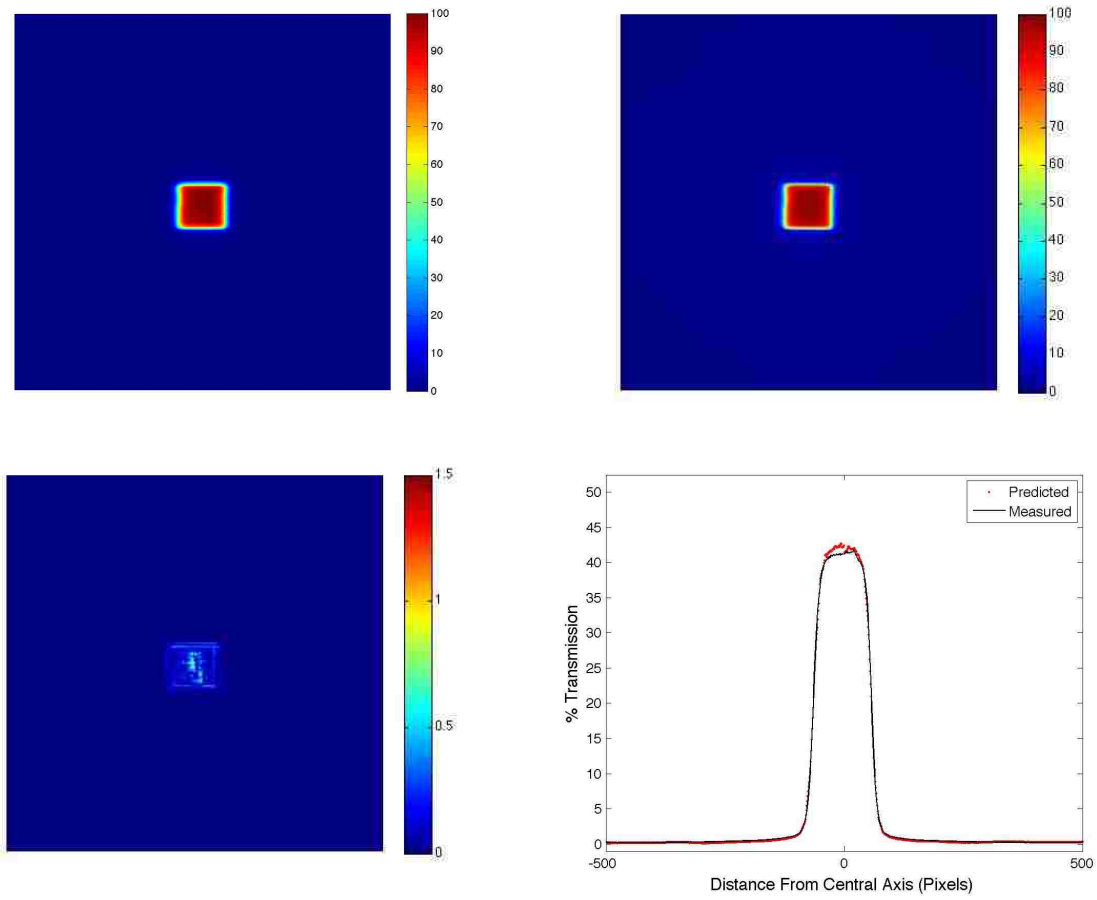

Figure A.0.31. ABOVE: Relative intensity maps for 3x3 FS, heterogeneous cylinder phantom predicted (left) and measured (right) portal images. BELOW: 3x3 FS, heterogeneous cylinder phantom gamma values (left) and % transmission relative to the through-air profiles (right).

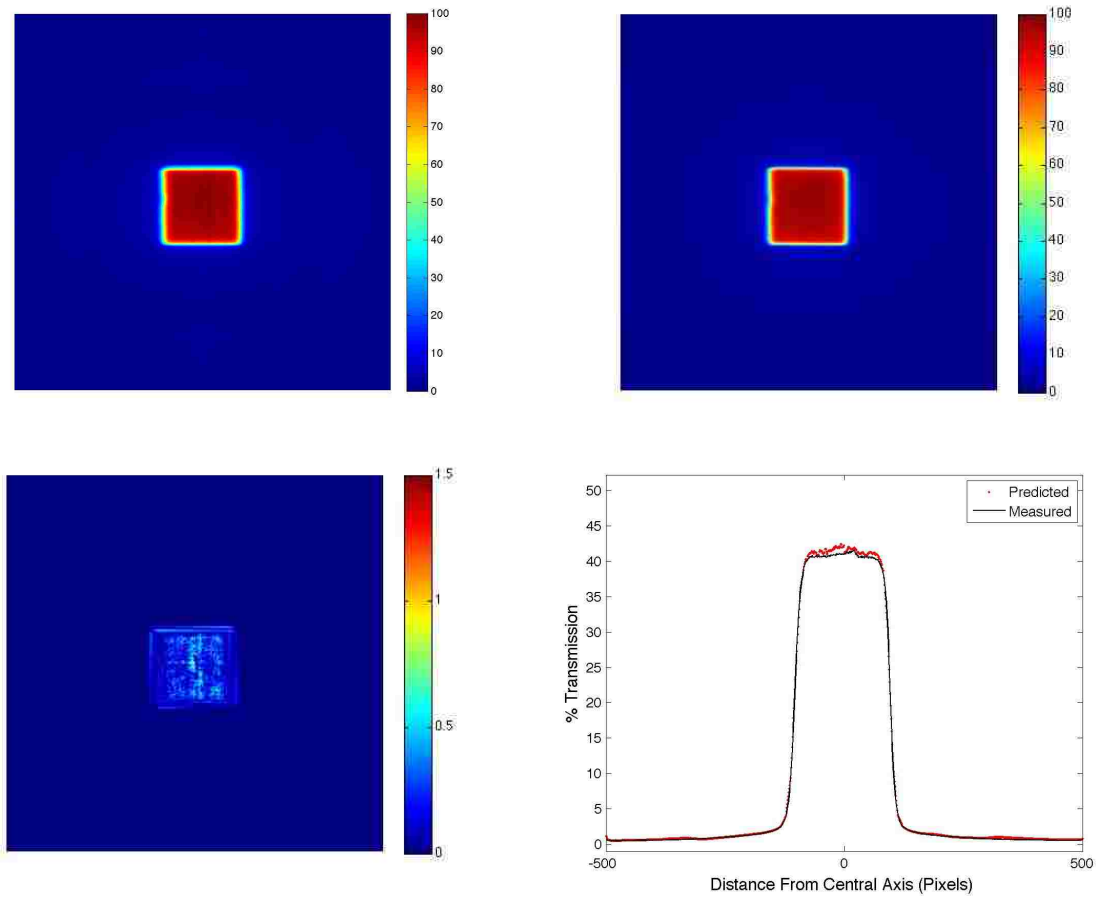

Figure A.0.32. ABOVE: Relative intensity maps for 5x5 FS, heterogeneous cylinder phantom predicted (left) and measured (right) portal images. BELOW: 5x5 FS, heterogeneous cylinder phantom gamma values (left) and % transmission relative to the through-air profiles (right).

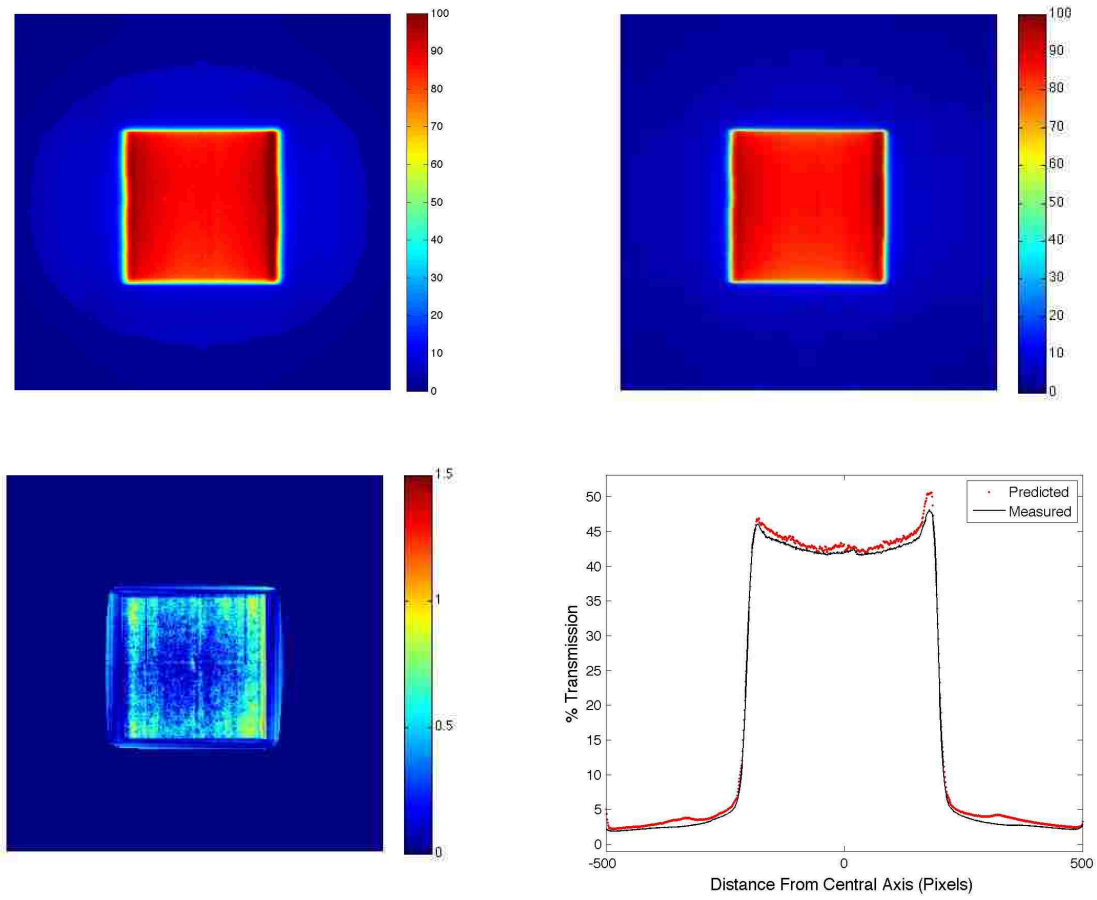

Figure A.0.33. ABOVE: Relative intensity maps for 10x10 FS, heterogeneous cylinder phantom predicted (left) and measured (right) portal images. BELOW: 10x10 FS, heterogeneous cylinder phantom gamma values (left) and % transmission relative to the through-air profiles (right).

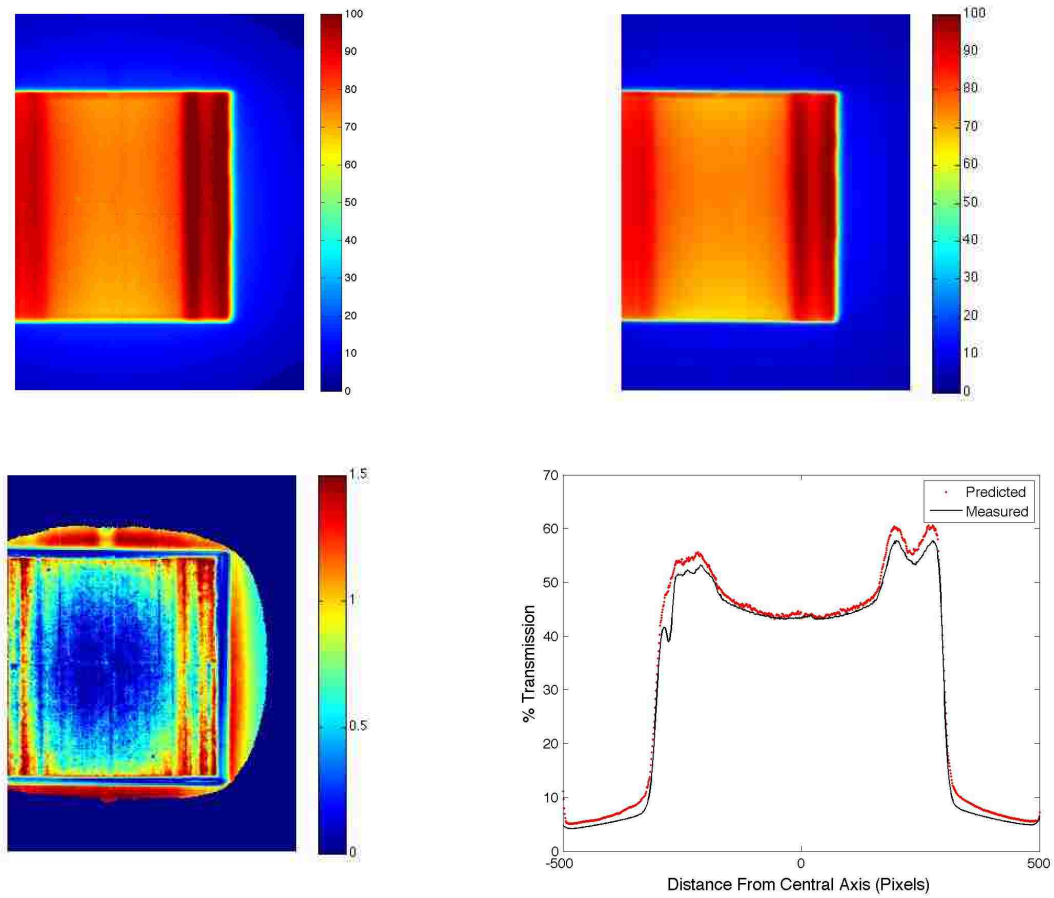

Figure A.0.34. ABOVE: Relative intensity maps for 15x15 FS, heterogeneous cylinder phantom predicted (left) and measured (right) portal images. BELOW: 15x15 FS, heterogeneous cylinder phantom gamma values (left) and % transmission relative to the through-air profiles (right).

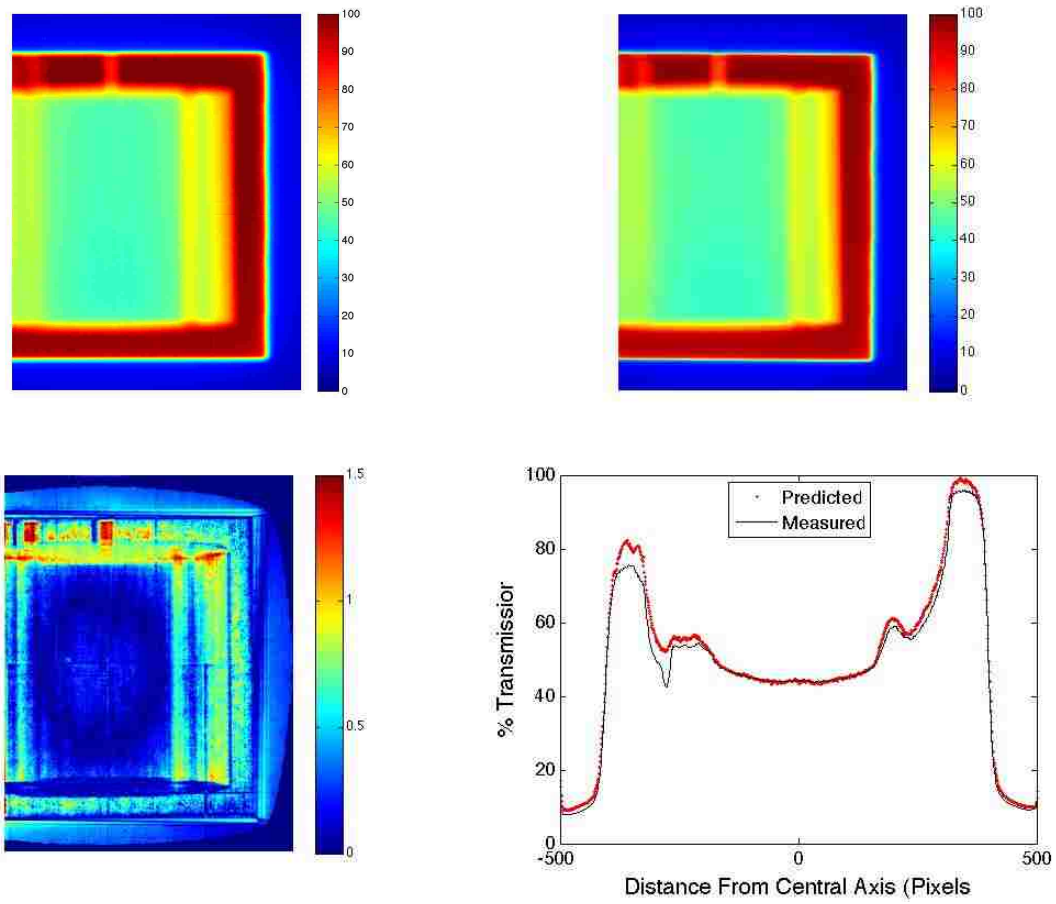

Figure A.0.35. ABOVE: Relative intensity maps for 20x20 FS, heterogeneous cylinder phantom predicted (left) and measured (right) portal images. BELOW: 20x20 FS, heterogeneous cylinder phantom gamma values (left) and % transmission relative to the through-air profiles (right).

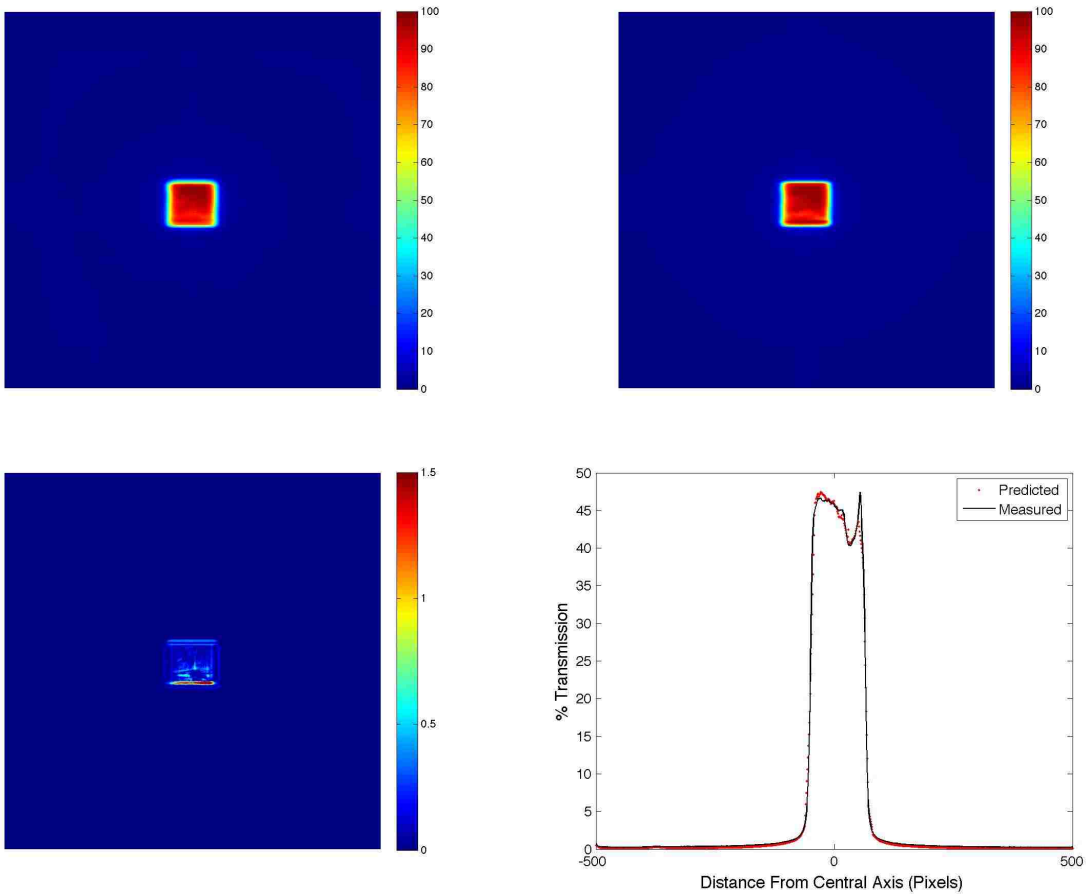

Figure A.0.36. ABOVE: Relative intensity maps for 3x3 FS, anthropomorphic head phantom predicted (left) and measured (right) portal images. BELOW: 3x3 FS, anthropomorphic head phantom 5%/3mm gamma values (left) and % transmission relative to the through-air profiles (right).

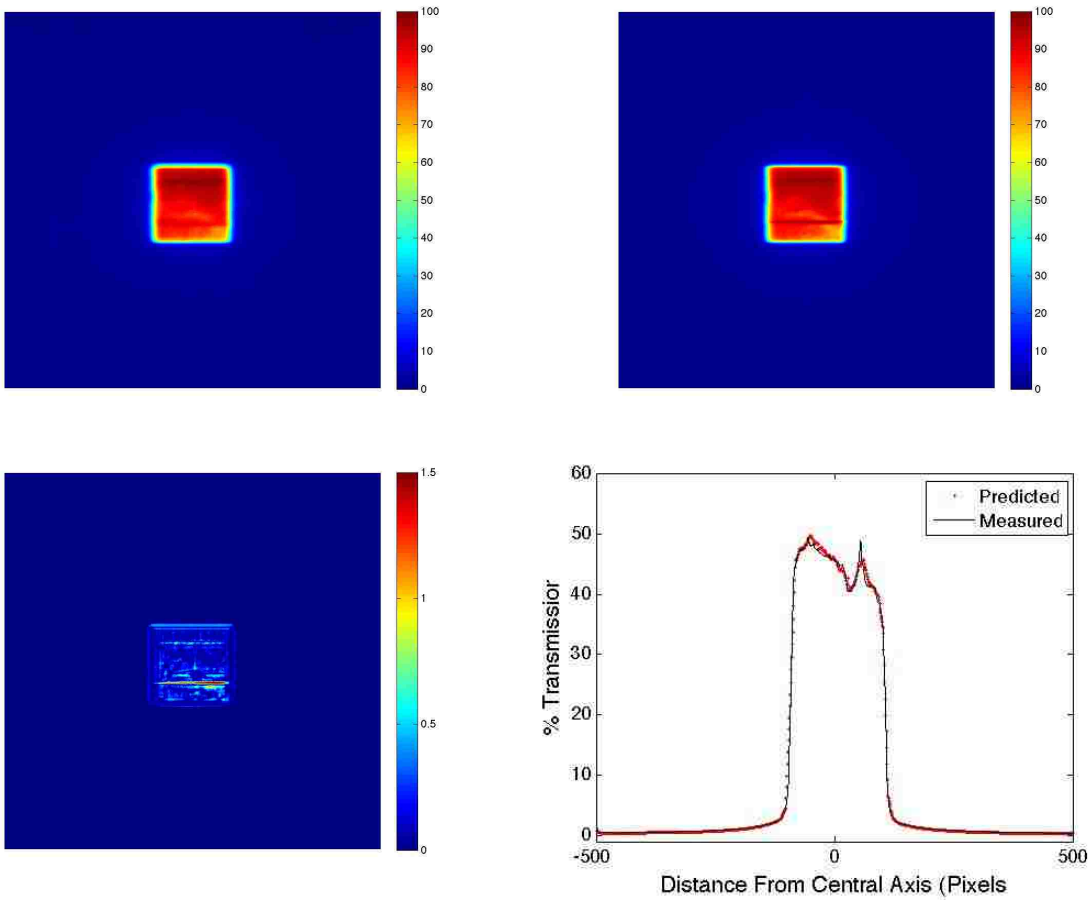

Figure A.0.37. ABOVE: Relative intensity maps for 5x5 FS, anthropomorphic head phantom predicted (left) and measured (right) portal images. BELOW: 5x5 FS, anthropomorphic head phantom 5%/3mm gamma values (left) and % transmission relative to the through-air profiles (right).

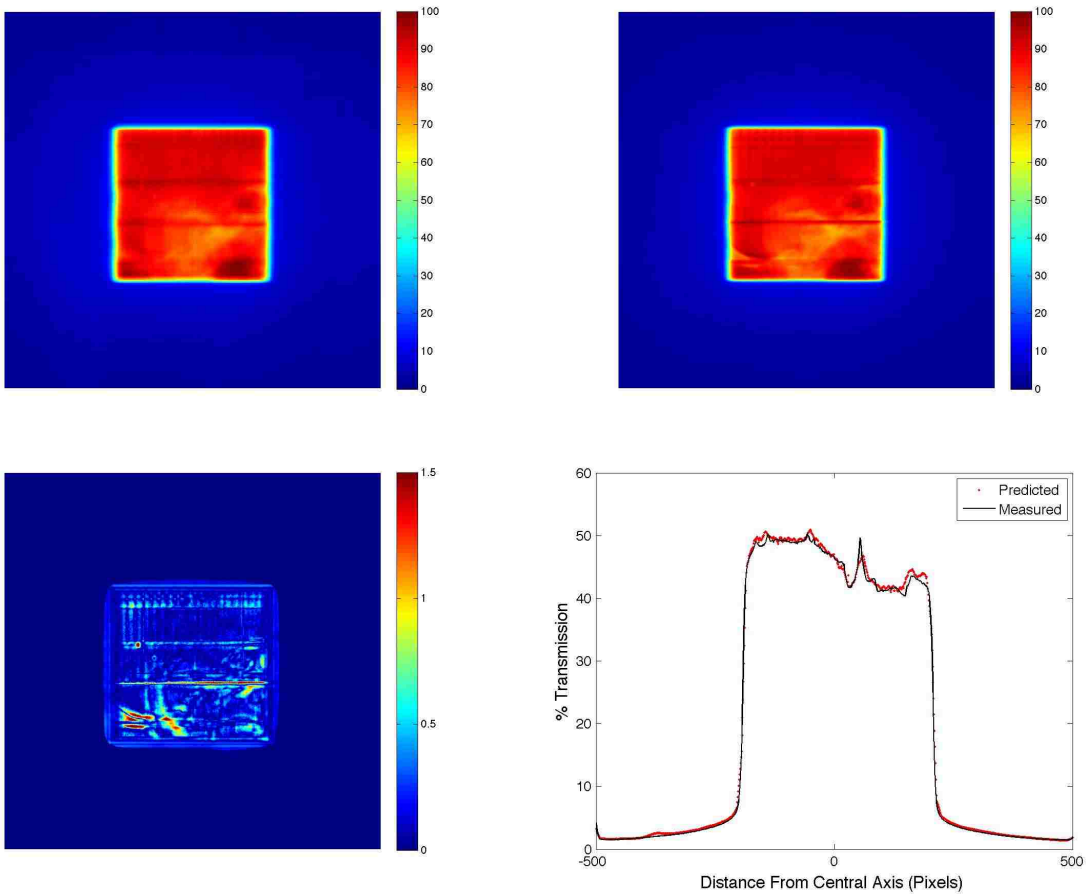

Figure A.0.38. ABOVE: Relative intensity maps for 10x10 FS, anthropomorphic head phantom predicted (left) and measured (right) portal images. BELOW: 10x10 FS, anthropomorphic head phantom 5%/3mm gamma values (left) and % transmission relative to the through-air profiles (right).

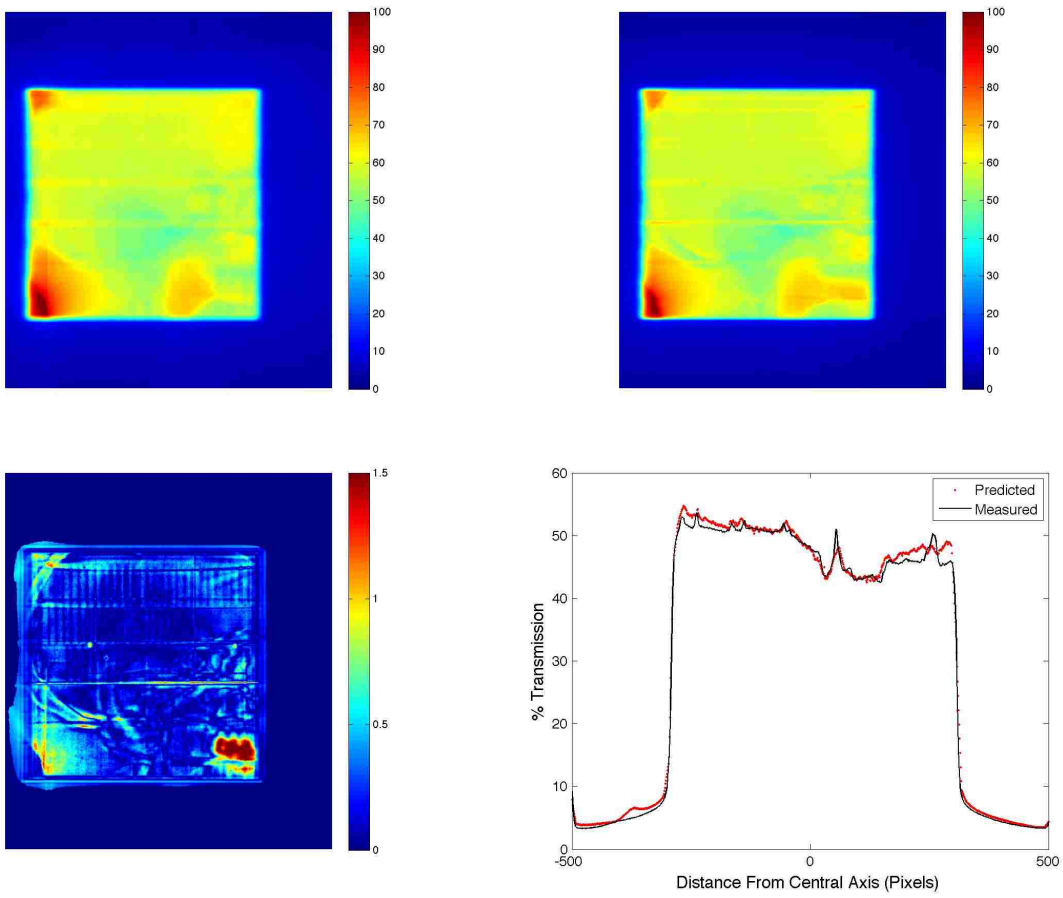

Figure A.0.39. ABOVE: Relative intensity maps for 15x15 FS, anthropomorphic head phantom predicted (left) and measured (right) portal images. BELOW: 15x15 FS, anthropomorphic head phantom 5%/3mm gamma values (left) and % transmission relative to the through-air profiles (right).

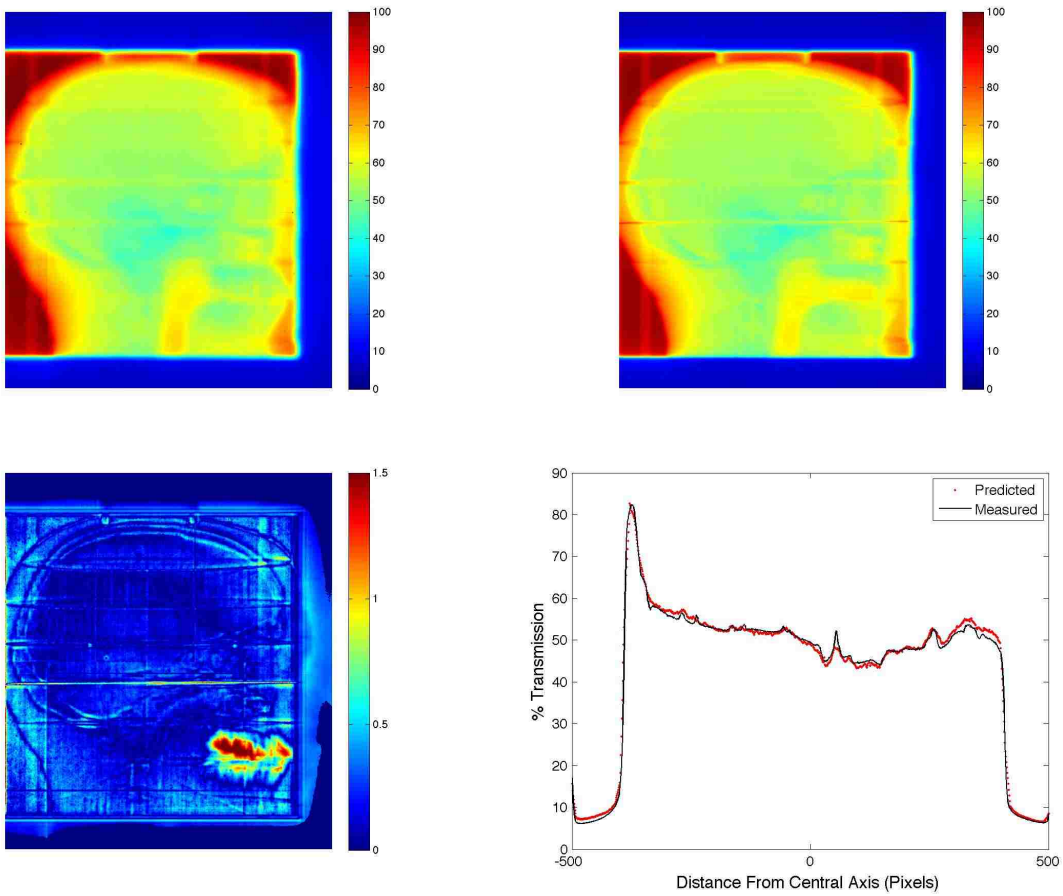

Figure A.0.40. ABOVE: Relative intensity maps for 20x20 FS, anthropomorphic head phantom predicted (left) and measured (right) portal images. BELOW: 20x20 FS, anthropomorphic head phantom 5%/3mm gamma values (left) and % transmission relative to the through-air profiles (right).

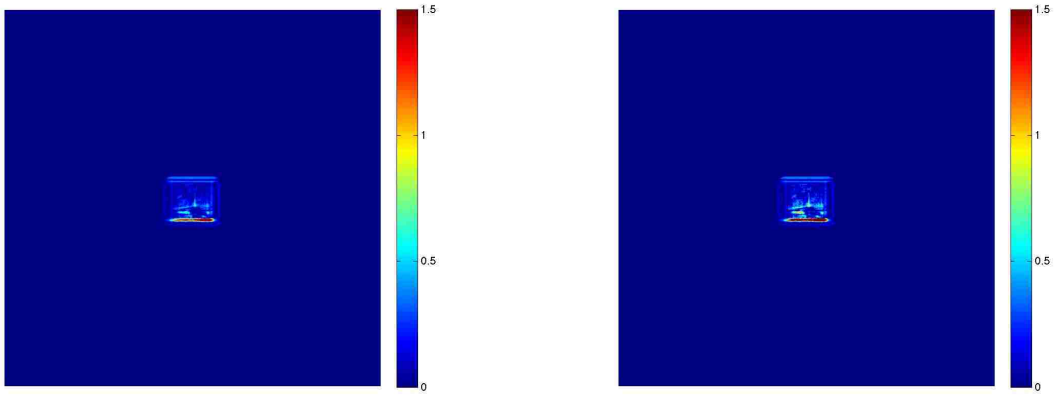

Figure A.0.41. 3x3 FS, anthropomorphic head phantom 5%/ 3 mm gamma values (left) and 3%/3mm gamma values (right).

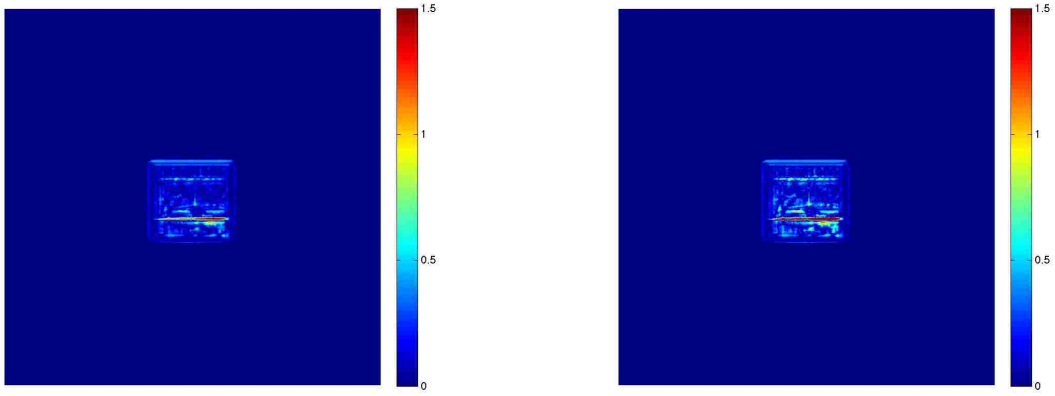

Figure A.0.42. 5x5 FS, anthropomorphic head phantom 5%/ 3 mm gamma values (left) and 3%/3mm gamma values (right).

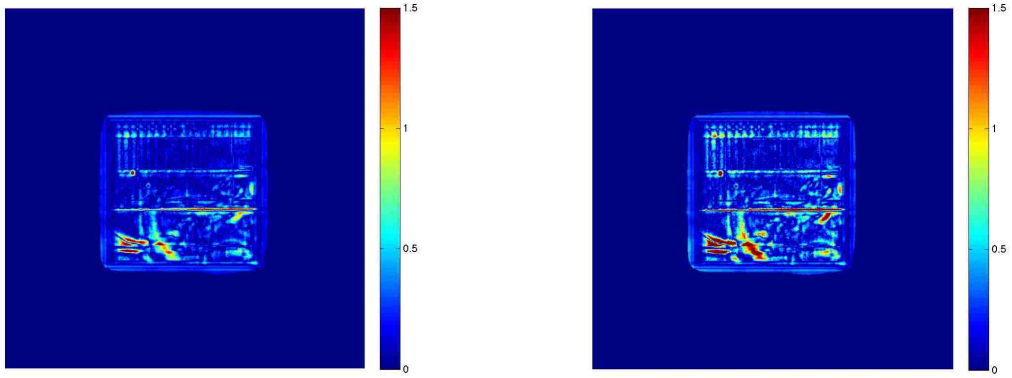

Figure A.0.43. 10x10 FS, anthropomorphic head phantom 5%/ 3 mm gamma values (left) and 3%/3mm gamma values (right).

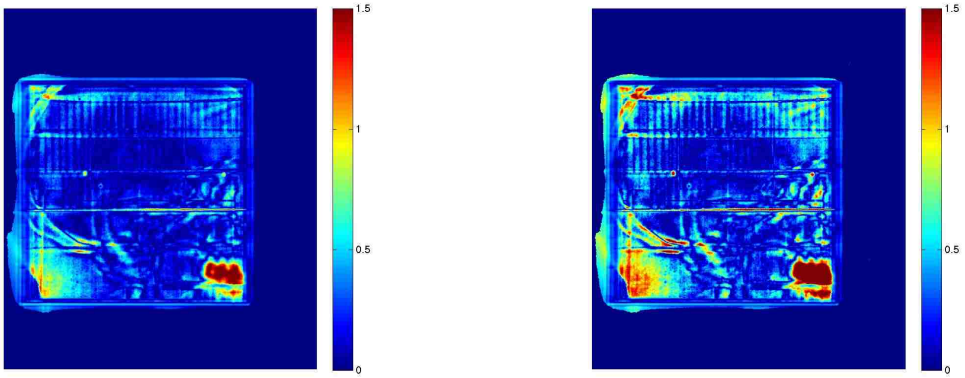

Figure A.0.44. 15x15 FS, anthropomorphic head phantom 5%/ 3 mm gamma values (left) and 3%/3mm gamma values (right).

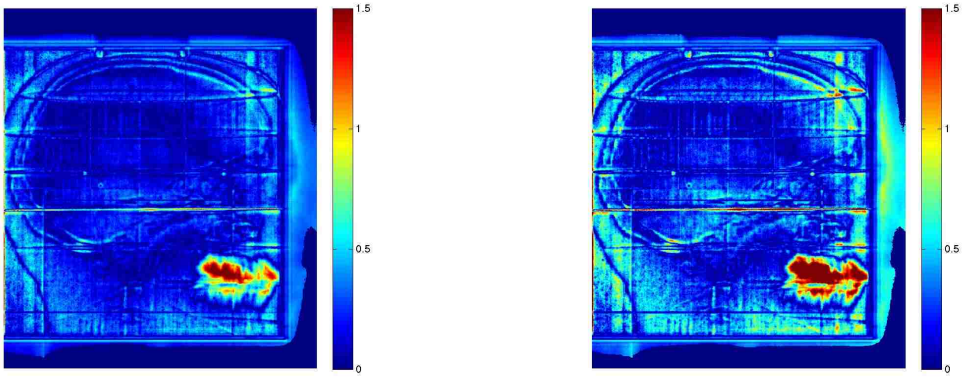

Figure A.0.45. 20x20 FS, anthropomorphic head phantom 5%/ 3 mm gamma values (left) and 3%/3mm gamma values (right).

VITA

Bart Morris was born in Kenton, Ohio, where he grew up and attended Kenton Senior High School. He received a Bachelor of Science Degree in Physics from Middle Tennessee State University in 2011 and enrolled in the Medical Physics Master's program at LSU the following year. Following graduation from LSU he will begin medical physics residency training at the University of Mississippi Medical Center in Jackson, Mississippi.